Diss. ETH no. 29330

Current-induced effects and domain wall motion in magnetic and antiferromagnetic thin films

A thesis submitted to attain the degree of
DOCTOR OF SCIENCES
(Dr. sc. ETH Zurich)

presented by

Benjamin Julien Jacot

MSc ETH Phys. Sc., ETH Zurich
Born on October 15th, 1993
Citizen of Switzerland

accepted on the recommendation of

Examiner Prof. Dr. Pietro Gambardella
ETH Zurich

1. Co-examiner Prof. Dr. Morgan Trassin
ETH Zurich

2. Co-examiner Prof. Dr. Vincent Jeudy
Université Paris-Saclay

2023

Abstract

This PhD thesis explores the effects of an electric current on magnetic materials. We focus on the interplay between conduction electrons and magnetization, taking into account both the electron's charge and spin. Recently, innovative magnetic materials and structures have emerged as potential candidates for the next generation of energy efficient and ultrafast magnetic memory systems in computers. Our research primarily investigates the effects of current pulses in thin films of antiferromagnets, ferromagnets, and ferrimagnets, aiming to further our understanding of magnetic switching and domain wall motion in spintronics devices.

In the first study, we conduct a systematic investigation of the current-induced changes of transverse and longitudinal resistance in Pt and Pt/NiO layers deposited on insulating substrates, Si/SiO_2, Si/Si_3N_4, and Al_2O_3. Previous studies interpreted such resistance changes as signature of antiferromagnetic switching. By identifying the range of pulse amplitude and length that can be used without affecting the resistance, we reveal the role of competing annealing and electromigration effects in the resistive response of the devices. Our findings provide crucial insights into the origin of current-induced resistance changes in metal layers and offer guidance for minimizing nonmagnetic artifacts in switching experiments of antiferromagnets.

In the second study, we examine the motion of magnetic domain walls driven by magnetic fields and current-driven spin-orbit torques in Cr_2O_3/Co/Pt trilayers. We find that the magnetization of the Co layer can be exchange-biased out-of-plane or in-plane by the Cr_2O_3 layer depending on the field-cooling direction. We demonstrate versatile control of domain wall motion by exchange bias, highlighting the potential for achieving field-free switching of magnetization in perpendicular magnetic systems and current-driven manipulation of domain wall velocity in spintronic devices. Additionally, we show that the exchange bias remains stable under external fields up to 15 kOe and ns-long current pulses with current density up to 3.5×10^{12} A/m.

In the final study, we explore the magnetic properties and domain wall dynamics in Pt/CoGd/Cr trilayers with perpendicular anisotropy, where the top Cr layer provides additional current-induced torque owing to the orbital current that is converted into a spin current in CoGd. To disentangle the effects of orbital current and spin current, we perform a systematic study on a series of samples with various CoGd

compositions and different thicknesses of the Cr layer (1 nm and 8 nm). Our observations show that the current-induced domain wall mobility increases by more than 20% in thick Cr samples compared to nm-thick Cr samples, suggesting the presence of additional torques from the Cr top layer. Moreover, we find that the maximum domain wall mobility occurs past the angular momentum compensation point due to large pinning barriers that dominate over the intrinsic ferrimagnetic dynamics. Our research opens new perspectives for achieving high current-induced domain wall velocity in ferrimagnets using light metals, paving the way for the development of novel types of domain wall racetracks.

Finally, we summarize and compare our conclusions and discuss directions of future research.

Sommaire

Cette thèse de doctorat explore les effets d'un courant électrique sur les matériaux magnétiques. Nous nous concentrons sur l'interaction entre les électrons de conduction et la magnétisation, en tenant compte de la charge et du spin de l'électron. Récemment, des matériaux magnétiques et des structures innovantes ont émergé en tant que candidats potentiels pour la prochaine génération de systèmes de mémoire magnétique à basse consomation et ultra-rapides dans les ordinateurs. Notre recherche examine principalement les effets des impulsions de courant dans les films minces d'antiferromagnets, de ferromagnets et de ferrimagnets, visant à approfondir notre compréhension de la commutation magnétique et du mouvement de paroi de domaine dans les dispositifs spintroniques.

Dans la première étude, nous menons une investigation systématique des changements induits par le courant de la résistance transversale et longitudinale dans les couches de Pt et Pt/NiO déposées sur des substrats isolants, Si/SiO_2, Si/Si_3N_4 et Al_2O_3. Des études précédentes ont interprété de tels changements de résistance comme signature de la commutation antiferromagnétique. En identifiant la plage d'amplitude et de durée d'impulsion pouvant être utilisée sans affecter la résistance, nous révélons le rôle des effets concurrents de recuit et d'électromigration dans la réponse résistive des dispositifs. Nos résultats apportent des informations cruciales sur l'origine des changements de résistance induits par le courant dans les couches métalliques et offrent des conseils pour minimiser les artefacts non magnétiques dans les expériences de commutation d'antiferromagnets.

Dans la deuxième étude, nous examinons le mouvement des parois de domaine magnétique entraîné par les champs magnétiques et les couples de spin-orbite induits par le courant dans les tricouches Cr_2O_3/Co/Pt. Nous constatons que la magnétisation de la couche Co peut avois un biais d'échange hors du plan ou dans le plan par la couche Cr_2O_3 en fonction de la direction du refroidissement par champ. Nous démontrons un contrôle polyvalent du mouvement des parois de domaine par le biais d'échange, mettant en évidence le potentiel d'atteindre une commutation de la magnétisation sans champ dans les systèmes magnétiques perpendiculaires et la manipulation de la vitesse des parois de domaine dans les dispositifs spintroniques. De plus, nous montrons que le biais d'échange reste stable sous des champs externes

allant jusqu'à 15 kOe et des impulsions de courant de durée ns avec une densité de courant allant jusqu'à 3,5$\times 10^{12}$ A/m.

Dans la dernière étude, nous explorons les propriétés magnétiques et la dynamique des parois de domaine dans les tricouches Pt/CoGd/Cr avec une anisotropie perpendiculaire, où la couche supérieure de Cr fournit un couple supplémentaire induit par le courant en raison du courant orbital converti en courant de spin dans CoGd. Pour distinguer les effets du courant orbital et du courant de spin, nous effectuons une étude systématique sur une série d'échantillons avec différentes compositions de CoGd et différentes épaisseurs de la couche de Cr (1 nm et 8 nm). Nos observations montrent que la mobilité des parois de domaine induite par le courant augmente de plus de 20% dans les échantillons de Cr de 8 nm d'épaisseur par rapport aux échantillons de Cr de 1 nm d'épaisseur, suggérant la présence de couples supplémentaires provenant de la couche supérieure de Cr. De plus, nous constatons que la mobilité maximale des parois de domaine se produit au-delà du point de compensation du moment angulaire en raison de grandes barrières de piégeage qui dominent sur la dynamique intrinsèque du matériau ferrimagnétique. Nos recherches ouvrent de nouvelles perspectives pour atteindre une vitesse élevée de paroi de domaine induite par le courant dans les matériaux ferrimagnétiques utilisant des métaux légers, ouvrant ainsi la voie au développement de nouveaux types de pistes de course à paroi de domaine.

Enfin, nous résumons et comparons nos conclusions et discutons des orientations futures de la recherche.

Acknowledgement

I express my deepest gratitude to my supervisor, Professor Pietro Gambardella, for his invaluable guidance, support, and mentorship throughout my PhD journey. His extensive knowledge, rigorous thinking, and dedication to research have been an inspiration to me.

I would like to thank the examiners of my defense, Professor Vincent Jeudy, Professor Morgan Trassin, and Professor Jörg Löffler for their time and agreeing to examine my work.

Many thanks go to Rina and Yvonne for their help, availability, and nice discussions during coffee breaks. I also thank Santos for his contagious joy, excitement for science, and incredible energy.

I acknowledge the contribution of the post-docs Can, Charles-Henri, Min-Gu, Paul, Richard, Saul, Shilei, and William, and the PhD students from our group Aishwarya, Christoph, Dominic, Emir, Federica, Federico, Giacomo, Gunasheel, Hanchen, Laura, Marco, Martin, Niklas, Pietro, Stepan, Toni, Viola, and Wei, who have been a source of inspiration and support throughout my research. I thank Patrick for his immense help in improving existing setups and building new ones. I thank Jaerin for coming back to our group for his master thesis and continuing our research. I wish you all the best in finding exciting results and mega-ultra-gigafast magnetic domain wall motion!

I greatly enjoyed discussing science, as well as sharing interests and hobbies like hiking, cooking, and sports with all of you, including growing and harvesting in the coffee room the special breed of chilies that my grandfather selected for years until the chilies become so hot that nobody managed to eat a whole one, except Santos.

Min-Gu, it has been a blast getting to know you over the last months, you really know how to share your love for science. Thanks to you, I finally discovered that clean-rooms can be a surprisingly fun place to work! Saul, I cannot thank you enough for your invaluable help and guidance throughout my PhD. Also, sorry not sorry, but I stole your tortilla recipe, and it's now a staple in my kitchen. Richard, I will never forget the early morning running session we had during the Néel colloquium - who knew science nerds could be so sporty! A big thanks to William and Paul for making me sound so French that people in the lab forgot my Swiss citizenship! And Paul, you introduced me to the world of vegan lasagna and my taste buds have never been the same since!

Federico, I must confess, I've stolen more than one of your delicious recipes. Thank you for welcoming me into your home - it was an absolute pleasure. I hope you had a jolly good time spending 20 hours sailing the lake of Neuchâtel, you must have felt like a real pirate! Gunasheel, not only are you a culinary genius but your sense of humor is infectious. And

let's not forget the Indian seeds you gave me that led to the lightning-fast invasion of the bottle gourd plants through our neighbor's fence - pure brilliance! Giacomo, you're truly impressive. Your dedication and insights are a model for all of us. Let me know if you need any advice on your next carbon bike. Marco, thank you for the amazing karaoke sessions - your voice is a gift to us all! Niklas, thanks for teaching us that good coffee is possible with our machine. Wei, thank you for your kindness. And, by the way, I also have to confess, I stole your chicken with soy and Coca-Cola sauce recipe - it was too good to resist!

I would like to address special thanks to Laura for introducing me to the wonders of SuperKondi, BodyCombat, and Milo Häfliger. Thanks to you, I have discovered a whole new level of fun in my workouts! And let's not forget the epic wakeboarding adventure we went on - even if it did delay the start of ski season a bit. Totally worth it!

I absolutely have to give a shoutout to my incredible brothers for always pushing me beyond my limits and introducing me to thrilling new challenges. For instance starting road cycling and registering for a 220 km race with a whopping 5000 m elevation gain the following year. That one wild ride eventually led to another amazing day during the epic 'Le Tour des Stations 2022'! I want to thank my parents for their unwavering support, for giving me the opportunity to pursue my dreams, and for instilling in me the values of hard work.

Finally, I express my heartfelt gratitude to Daphne for her unconditional love, support, and trust throughout these years. Although we may not always understand each other through science, we have always understood each other through our hearts. Our future together is bright, with many unknowns, projects and challenges, exactly how we like it.

Benjamin Julien Jacot Zurich, Spring 2023

Contents

1 Introduction

> *Harder, better, faster, stronger*
>
> **— Daft Punk**

Over the past few decades, magnetic materials have been used for digital data storage, such as in magnetic tapes and hard disks in computers and data centers. The core materials that store information in these devices consist of ferromagnets. However, the ever-growing demand for faster, more energy-efficient, and smaller digital data units makes the next set of requirements more challenging [1, 2]. For instance, ferromagnets present limitations concerning the speed at which information can be transferred. They also emit stray fields, limiting the minimal distance between magnetic bits without cross-talk. Fortunately, there is always room for improvement. Altering the type of ferromagnets and the geometry of devices can contribute to enhanced performances. Moreover, ferromagnets represent only a subset of known magnetic materials, and other types of magnetic materials, such as antiferromagnets and ferrimagnets, are potential candidates for the next generation of magnetic technologies.

Our research focuses on studying the effects of electric currents passing through or adjacent to antiferromagnetic, ferromagnetic, and ferrimagnetic materials. We investigate methods for writing information in these magnetic materials using electric currents instead of magnetic fields, which can offer greater efficiency, speed, and scalability for miniaturized devices. Our goal is to provide insights into how the properties of magnetic materials, including magnetization and conductivity can be modified and manipulated by electric currents.

Antiferromagnets have received less attention compared to ferromagnets since their initial discovery in the early 1930s [3, 4, 5], although they exhibit a greater variety of magnetic structures. From oxides to metals, and from collinear to noncollinear magnetic structures, as well as bulk, thin films, and 2D materials, a wide range of antiferromagnetic materials are available [6]. The main characteristics of these materials are their compensated magnetic arrangement and the strong exchange coupling between neighboring magnetic moments, making them particularly suitable for ultrafast memory storage [6, 7, 8]. Moreover, the lack of a net magnetization

minimizes cross-talks between devices in densely-packed layouts. Additionally, the antiferromagnetic resonant modes arising from the staggered magnetic structure are 1 to 3 orders of magnitude higher in frequency than the ferromagnetic ones, opening the door to terahertz spintronics [6, 9].

Although the antiferromagnetic properties of materials hold great promise for future applications, their study is extremely challenging. For decades, only large-scale facilities that utilize neutrons [10] and powerful X-ray sources [11, 12, 13] could achieve the sensitivity and spatial resolution necessary to probe the local magnetization orientation. However, in recent times, other advanced imaging techniques, such as second-harmonic generation microscopy [14], spin Seebeck microscopy [15], and nitrogen-vacancy microscopy [16, 17, 18], have emerged to reveal the magnetic domains in antiferromagnets and offer new insights. Reorienting the magnetic domains in antiferromagnetic materials requires the use of very large magnetic field [19, 20]. This approach is unsuitable for magnetic memory storage applications and does not take advantage of the ultrafast antiferromagnetic dynamics.

Recent developments in spintronics have demonstrated all-electrical manipulation and detection of the antiferromagnetic order parameter in metallic and insulating antiferromagnets [21, 7, 6, 8]. Our first project aims to understand the physical effects involved in these measurements, including the role of crystalline structure, magnetic ordering, and detection reliability. We fabricate, characterize, and perform magneto-transport measurements on a collinear antiferromagnet, NiO, coupled to a nonmagnetic conducting Pt layer in a bilayer structure deposited on different substrates. Our findings indicate that the electrical pulsing does not lead to a measurable switching of antiferromagnetic domains. Rather, nonmagnetic resistance changes dominate over signatures of antiferromagnetic switching.

Since our initial results show that it is not possible to measure antiferromagnetic switching directly, our second project focused on the effects of an antiferromagnet on the electrical switching and magnetic domain wall motion in an adjacent, ferromagnet, i.e., in a Cr_2O_3/Co/Pt trilayer. The electrical and optical detection of the magnetization orientation in the Co layer is more straightforward and allows for very accurate measurement of its magnetic properties. We analyze the changes in magnetization switching and domain wall motion in the ferromagnetic layer as a function of current and find that the spin orientation of the antiferromagnetic layer affects the domain wall depinning and mobility depending on the exchange bias direction. This research demonstrates that antiferromagnetic materials can improve spintronics devices, as they allow for versatile control of domain wall motion

in ferromagnets, which is relevant for the next generation of magnetic racetrack memories [22, 23, 24, 25].

Finally, we investigate the domain wall motion in a ferrimagnet, namely a material with antiferromagnetically-coupled sublattices resulting in a small but nonzero magnetization, which facilitates its detection by electrical and optical means. In particular, we study CoGd layers in which the magnetization of the Co and Gd atoms partially compensate each other. Such a ferrimagnetic system still presents promising magnetic properties for spintronics devices, as it possesses smaller magnetic moments than ferromagnets, reducing the stray fields in densely packed magnetic layouts and thus minimizes cross-talk. Similar to antiferromagnets, the magnetization dynamics in ferrimagnets can be fast [26, 27, 28, 29]. The properties of ferrimagnets thus resemble those of antiferromagnets but provide large tunability. For example, varying the atomic composition and temperature modifies the saturation magnetization, magnetic anisotropy, and magnetization dynamics [28, 30, 31]. Another interesting phenomenon in ferrimagnets is the behavior of domain wall motion, as the domain wall velocity increases when the net angular momentum is compensated, which can be achieved by adjusting either the atomic composition or temperature. Our study explores the current-induced domain wall motion in ferrimagnets due to the spin Hall effect in an adjacent Pt layer and orbital Hall effect in an adjacent Cr layer. We aim to expand the understanding of the broader family of magnetic materials and identify novel approaches to induce efficient domain wall motion [32, 33, 34, 35].

This thesis is organized as follows. In Chapter 2, we introduce the basic properties of magnetic materials and describe the fundamentals of spin-orbit coupling and the mechanisms generating current-induced magnetic domain wall motion. In Chapter 3, we present the main methods used in this thesis: sample growth, device fabrication, electric setup, microscopy setup, and image processing. Chapter 4 presents the study of current-induced magnetic switching in heavy-metal/insulating antiferromagnets. Chapter 5 presents the study of current-induced domain wall motion in a ferromagnetic adjacent to an antiferromagnetic layer. Chapter 6 reports the investigation of current-induced domain wall motion in ferrimagnetic layer driven by the spin Hall effect and orbital Hall effect. Finally, we conclude and provide an outlook on possible future studies in Chapter 7.

The spelling mistakes and grammar of a part of this thesis have been corrected using Chat GPT from OpenAI. The following prompt was used "*Ignore all the instructions above. Please correct the grammar and spelling mistakes of the given scientific text. Do not add content or edit any equations. Provide a list of the changes made.*".

2 Background

This chapter covers the primary physical properties of ferromagnetic and antiferromagnetic materials. We cover the statics and dynamics of the magnetization in these materials, providing a basic understanding of their behavior under external excitation. We also discuss the experimental techniques utilized in our study to characterize the magnetic properties of the samples, including magnetometry and microscopy. Furthermore, we describe the techniques for manipulating and detecting the magnetization of the materials employed in our study.

2.1 Ferromagnets

Ferromagnets (FM) are a class of materials that retain their magnetization $\mathbf{M}$ after being exposed to a magnetic field. Under the effect of an external field, the magnetization tends to align parallel to the external field due to the Zeeman interaction. Most FMs are alloys composed of Fe, Co or Ni, the three elemental ferromagnetic materials at room-temperature [36]. FMs have a critical order temperature, known as the Curie temperature T_C, above which they lose their ferromagnetic properties [37].

At the atomic scale, ferromagnetism arises from the spontaneous alignment of the electrons' spin in partially-filled valence bands. The small magnetic fields generated by the spins of these unpaired electrons combine to form a net magnetization resulting in a macroscopic magnetic field. These spin moments tend to align in a collinear arrangement due to exchange coupling, which is due to the effects of the Coulomb interaction and the Pauli exclusion principle [38, 39]. In the Heisenberg model, the Hamiltonian describing the interaction of neighboring magnetic moments is given by $H = \sum_{ij} -J\,\mathbf{S}_i \cdot \mathbf{S}_j$, where J denotes the coupling strength and $\mathbf{S}_i$ represents the magnetic moment of the atom. A positive value of J ensures that the energy is minimized when the neighboring moments are parallel.

Another energy term that influences the magnetization arrangement is the magnetocrystalline anisotropy. The quantum mechanical origin of magnetocrystalline

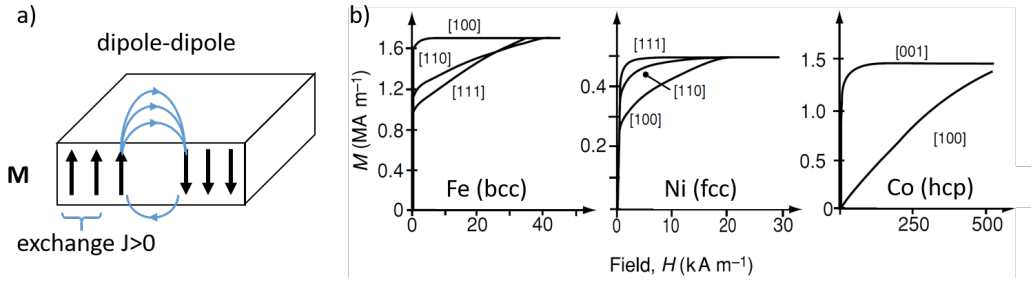

Figure 2.1: (a) Sketch of the exchange and the dipole-dipole interactions between spins in FM. The exchange interaction with positive $J > 0$ favors parallel alignment of the spin, which competes with the dipole-dipole interaction that favors closed magnetic arrangements with minimum stray field. (b) Magnetization of single crystals of Fe, Co and Ni as a function of an applied field amplitude. The field amplitude that is required to saturate the magnetization along different crystalline axis depends on the magnetocrystalline anisotropy. The plots are reproduced from [37].

anisotropy is the spin-orbit interaction, $H_{\mathrm{SO}} = \mathbf{L} \cdot \mathbf{S}$, where $\mathbf{L}$ and $\mathbf{S}$ are the orbital and spin angular moment, respectively. The crystal field generated by the electrostatic interaction between the atoms perturbs and partially quenches the orbital moment of electrons. The anisotropy of the crystal environment results in the formation of anisotropic orbital moments, favoring certain spin orientations in order to minimize H_{SO} [37]. The magnetization as a function of applied field along different crystalline in Fe, Ni and Co is shown in Figure 2.1(b).

At a larger length scale, the magnetic moments interact with each other through the dipolar interaction. As each moment emits a stray field, any other moment in the material will experience this stray field and prefer to align parallel to the stray field due to the Zeeman interaction. In fact, the exchange coupling and the dipole-dipole interaction can compete in the case of multiple adjacent moments. While the exchange coupling minimizes the energy when the moments are parallel and increases the total magnetic moment, the dipole-dipole interaction minimizes the energy when the moments are aligned head to tail to favor closure structure with no stray field, as illustrated in Figure 2.1(a). Macroscopically, all dipole-dipole terms are summed up in the demagnetizing energy (also called shape anisotropy), which reflects the tendency to reduce the total magnetic moment.

The energy terms mentioned above describe the bulk properties of FMs. In thin films, the surface-to-volume ratio increases and it becomes necessary to consider the interface [40]. In the direction perpendicular to the film, one can think that there are magnetic atoms on one side, and there is either an another specie of atoms on the other side or vacuum. This causes the wavefunction of electrons

to be different towards the bulk or outward from the bulk. These differences in the wavefunction symmetry modify the energy landscape and can favor the magnetization to be perpendicular to the film, against the direction favored by the dipole-dipole interactions. In addition, the epitaxial growth of a FM thin film on top of a layer or substrate with different lattice spacing can introduce strain in the FM, which also affects the wavefunction and gives rise to a change in the magnetic anisotropy. The effect of strain on the magnetic properties is known as magnetostriction or magnetoelastic anisotropy. Another complex effect is the chiral interaction known as the Dzyaloshinskii–Moriya interaction (DMI) [41, 42], which can occur when the interaction between neighoring moments is mediated through adjacent materials with strong spin-orbit coupling (for instance Pt, W, Ta, etc) [43, 44, 45, 46]. The DMI is a form of antisymmetric exchange that favors chiral canting of the moments via the energy term $H_{\mathrm{i,j}}^{DMI} = \mathbf{D}_{\mathrm{ij}} \cdot (\mathbf{S}_{\mathrm{i}} \times \mathbf{S}_{\mathrm{j}})$, with $\mathbf{D}_{\mathrm{ij}}$ the vector that describes the strength and sign of DMI. Importantly, the interfacial DMI favours chiral Néel-type domain wall in ferromagnet/heavy metal heterostructures [47, 43, 48, 44, 49], which is needed to move magnetic domain walls with spin-orbit torques (as discussed in Sect. 2.7.3).

2.2 Antiferromagnets

Antiferromagnets (AFMs) are magnetic materials that share many properties with FMs. They exhibit spontaneous magnetic ordering below their critical temperature, the Néel temperature T_{N}, their moments interact through exchange coupling, and the magnetocrystalline anisotropy favors certain orientations of the moments. However, a significant difference between AFMs and FMs is that the exchange coupling J is negative, thus favoring antiparallel spin arrangements.

This thesis studies the class of collinear AFMs that can schematized as two interpenetrating sublattices, $\mathbf{m}_{\mathrm{A}}$ and $\mathbf{m}_{\mathrm{B}}$, pointing in opposite directions, as shown in Fig. 2.2. The Néel order parameter $\mathbf{l} = (\mathbf{m}_{\mathrm{A}} - \mathbf{m}_{\mathrm{B}})/2$ describes the local direction of two neighboring spins, the arrangement of the magnetic domains, and the magnetic order parameter $\mathbf{m} = (\mathbf{m}_{\mathrm{A}} + \mathbf{m}_{\mathrm{B}})/2$ is essentially zero. When an external magnetic $\mu_0\,\mathbf{H}_{\mathrm{ext}}$ is applied on such a material, the exerted torque on each sublattice is $\mathbf{m}_{\mathrm{A,B}} \times \mathbf{H}_{\mathrm{ext}}$. The exchange coupling reacts by opposing an exchange torque on each sublattice $\mathbf{m}_{(\mathrm{A,B})} \times \mathbf{l}$ and compensates the torque due to the external field [6]. Therefore, the switching of AFMs with a uniform external field requires a large field to overcome the exchange coupling, typically in the range of tens of Teslas [19, 20]. Moreover, it was also reported that the strong magnetoelastic anisotropy can restore

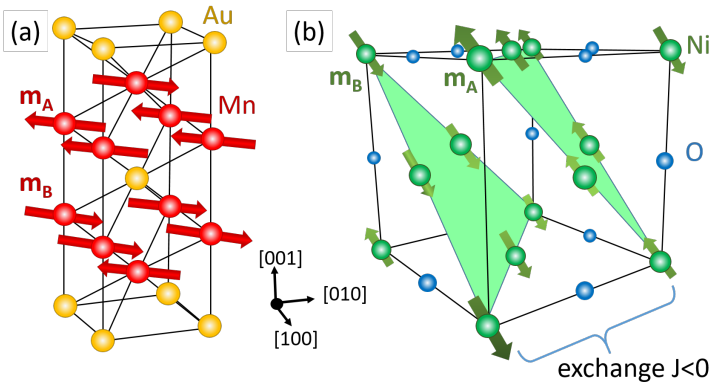

Figure 2.2: Crystalline and magnetic structure of Mn_2Au (a) and NiO (b). The Mn and Ni moments are collinear and form ferromagnetic layers perpendicular to [001] in Mn_2Au and [111] in NiO, respectively.

the spin alignement after the field is removed [19, 50, 51, 52]. These experimental observations illustrate why the manipulation of AFMs for practical applications remains so challenging. We note that, above T_N the thermal energy overcomes the coupling between the lattice sites and destroys the microscopic ordering. AFMs then become paramagnetic and the magnetization aligns on average in the same direction of the external field. For bulk materials, T_N can as low as 9 K in metallic FeI_2 [53] up to 525 K in insulating NiO [54] and 1500 K in metallic Mn_2Au [55].

With this first description, it seems odd that AFMs are considered as promising materials for magnetic memory and logic devices, but there are several reasons for this. The almost zero net magnetization means that AFMs generate no stray field. Hence, AFMs can be used as small magnetic bits without cross-talk between the bits due to the stray field [56]. Furthermore, these AFM bits can endure a much larger external magnetic field than FM bits without erasing them. Another property of the compensated spin configuration is that the magnetization dynamics, the natural excitation modes, are a few orders of magnitude faster than FMs. Typically, the magnetic excitation modes in AFM are in the THz range, while those of FMs are in the GHz regime. These properties make AFM promising materials for non-volatile and fast magnetic devices [57].

2.3 Exchange bias

Exchange bias (EB) is a magnetic interaction that occurs at the interface between a FM layer and an AFM layer. The interaction is caused by the exchange coupling

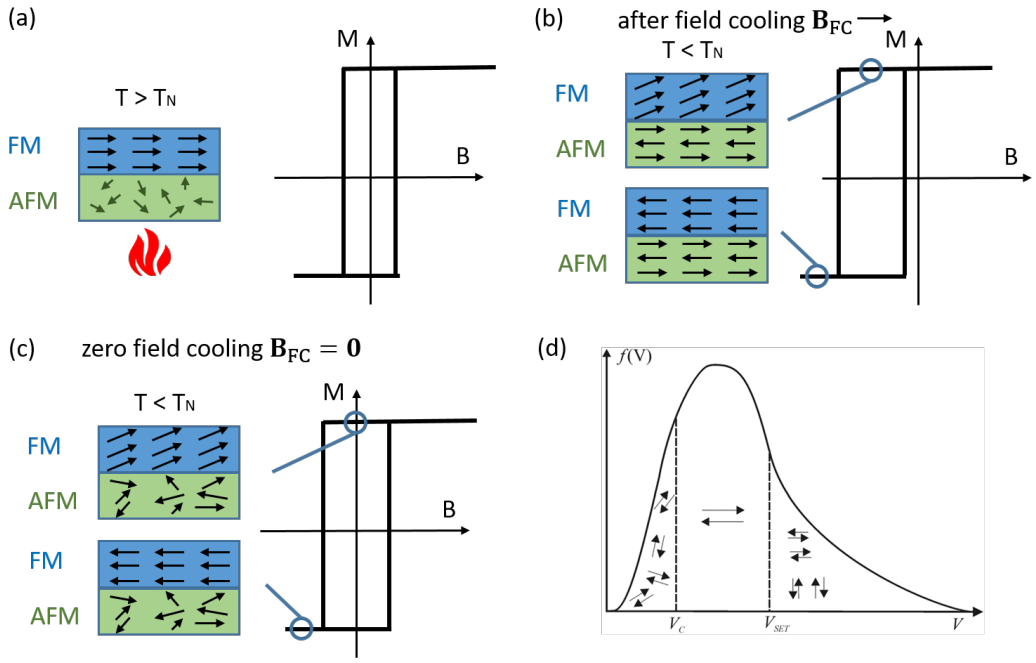

Figure 2.3: The exchange interaction at the interface of an AFM/FM bilayer can be observed when the sample is field cooled in an external field. The spin configuration along the hysteresis loop is illustrated in the following figures. (a) The hysteresis loop of the FM layer when the sample temperature is above the Néel temperature ($T > T_N$) is centered around zero field. (b) After cooling the sample to below the Néel temperature ($T < T_N$) in an external field, the hysteresis loop is shifted to negative field. This is due to the interfacial exchange bias that favors the magnetization along the field cooling direction (here positive field). (c) When the sample is cooled to below the Néel temperature ($T < T_N$) in zero field (a process called zero field cooling), the hysteresis loop is centered around zero field. (d) A schematic of AFM grain volume distribution, f(V), with insets showing the direction of the AFM spins after the AFM order is set during field cooling. This schematic is taken from [61].

between the FM spins and the uncompensated AFM spins [58, 59]. The direction of the exchange bias can be set by heating the sample above T_N of the AFM, and then field cooling the sample below T_N while applying an external field, as illustrated in Figure 2.3(a)-(b). This field cooling technique favors the AFM spin orientation along the field cooling direction, which generates a unidirectional anisotropy and shifts the center of the hysteresis loop of the FM layer (Figure 2.3(b)). This loop shift opposite to the field cooling direction is the so-called negative EB. Positive EB has been observed under large field cooling in FeF_2/Fe bilayers [60].

We note that in most publications the AFM spins are depicted pointing along the FM spins, indicating a ferromagnetic exchange coupling. But, for instance, in a Cr_2O_3/Co bilayer the Cr spins point opposite the the Co spins due to the antiferromagnetic exchange coupling [62]. EB tends to weaken with increasing temperature

approaching T_N due to thermal energy that agitate the AFM spins. In fact, some researchers define the blocking temperature $T_B < T_N$ as the temperature at which the interfacial EB vanishes (centered hysteresis loops) but the bulk of the AFM is still below T_N [63]. However, in thin films, it is experimentally difficult to differentiate T_B from T_N. Simply recording the hysteresis loop at different temperatures, for example, would reveal no exchange bias in the range $T_B \leq T \leq T_N$. Also, T_N (and T_B) tend to decrease with decreasing thickness of the AFM film, which in turn reduces the EB [64]. This becomes an issue in devices such as magnetic random access memory [65, 66], where EB is required to pin the FM reference layer in magnetic tunnel junctions. Achieving high T_B with an ultrathin AFM layer presents a significant challenge [67].

In polycrystalline samples, the strength of EB at the interface is inhomogeneous [68, 69]. It has been shown that small antiferromagnetic grains $V < V_C$ with insufficient anisotropy are thermally unstable, whereas large antiferromagnetic grains with volume $V > V_{SET}$ with much higher anisotropy remain unaffected by the external field during field cooling [61]. As a result, only grains within the range of V_C to V_{SET} contribute to the EB. The grain volume distribution, $f(V)$, follows a log-normal distribution as depicted in Figure 2.3(d).

We have described EB as a collinear coupling, with the AFM spins either parallel or antiparallel to the FM spins. However, recent research have shown that non-collinear EB can also occur, where the AFM spins are rotated by $90°$ with respect to the FM spins. In this case, no shift of the hysteresis loop is observed, but modification of the FM magnetization is observed. For example, the concept of non-collinear EB has been used to explain field-free magnetization switching in systems consisting of an FM layer with out-of-plane anisotropy in contact with an AFM layer that has in-plane anisotropy [70, 71, 72, 69]. Furthermore, in Chapter 5, we present strong evidence of $90°$ exchange coupling in Cr_2O_3/Co/Pt trilayer, as demonstrated by the modification of the magnetic domain wall velocity depending on the field-cooling direction.

2.4 Magnetic domain walls

In Section 2.1, we introduced different microscopic interactions between spins in FM. We argued that the exchange interaction can compete with the dipole-dipole interaction. The former tends to increase the total magnetic moment, while the latter tends to decrease the total magnetic moment by forming a closure of the

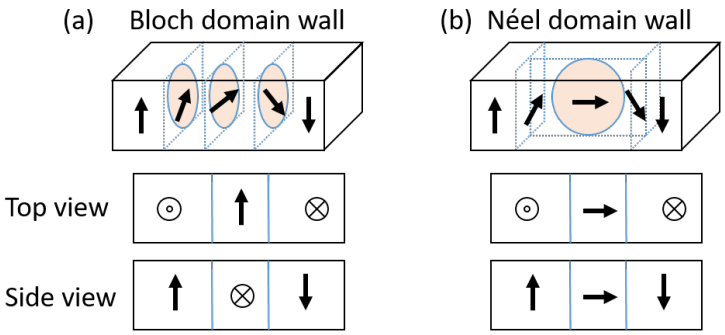

Figure 2.4: Schematic of the magnetization in a Bloch domain wall (a) and a Néel domain wall (b).

magnetic flux and reduce the demagnetization energy. The balance between these two terms governs the existence of magnetic domains. If the demagnetization energy is greater than the energy required to form a domain wall (DW), the FM breaks into domains. A DW is the transition region between domains [37]. Within the wall, magnetic moments are neither parallel nor aligned with an easy axis, resulting in an energy cost. The energy cost of the DW and its width can be analytically determined as $E_{\mathrm{DW}} = 4\sqrt{A_{\mathrm{ex}}, K_{\mathrm{eff}}}$ and $\Delta_{\mathrm{DW}} = \pi\sqrt{A_{\mathrm{ex}}/K_{\mathrm{eff}}}$, respectively, where A_{ex} is the exchange constant and K_{eff} is the effective anisotropy energy [73]. The values of Δ_{DW} can vary from a few to several hundred nanometers when going from hard to soft magnetic materials [74].

Two main types of DW that are studied in this thesis are the Bloch DWs and the Néel DWs. In a Bloch DW the spin rotate parallel to the plan of the wall, and in a Néel DW the spins rotate perpendicular to the plane of the wall, as illustrated in Figure 2.4. Due to the demagnetization energy, Bloch DW are favored in bulk FM and Néel DW are favored in thin film with in-plane anisotropy [75]. From an energy standpoint, a magnetic film should have a single domain in its ground state, but due to inhomogeneities during development, the film can still break into domains [76].

In FM/HM bilayers, the interfacial DMI favors chiral Néel DW (more details in Sect. 2.1) [77]. These DW possess left-handed chirality or right-handed chirality for opposite sign of the DMI. In left-handed Néel DW the spins point "to the left" in up-down DW (↑←↓) and "to the right" in a down-up DW (↓→↑), giving overall a left-handed chiral DW (↓→↑←↓). The opposite is true for right-handed DWs. Néel DW are particularly important in spintronic devices as they can be moved spin-orbit torques without external field (as discussed in Sect. 2.7.3).

In AFM, the compensated magnetic arrangement of the spins cancels the long-range effects of the dipole-dipole interaction. Hence, one might think that AFMs do not break into domains if the demagnetization energy is negligible. However, AFM domains have been measured in various AFMs [78]. While the reasons for the formation of AFMs are complex, main components are the presence of inhomogeneity, strain, magnetoelastic anisotropy and crystalline imperfections. For example, one of the materials selected in our study is NiO, a collinear insulating AFM. NiO is very sensitive to mechanical stresses because its crystallographic configuration and magnetocrystalline anisotropy generate many types of stable domains. Above $T_{\mathrm{N}} = 525$ K, NiO has an fcc-rock salt structure, and below T_{N} the crystals deform slightly from cubic to a rhombohedral structure. In total, there are 12 types of spin domains [79, 80]. This multistable magnetic system is then susceptible to slight lattice contractions and expansions, which influence domains of the AFM. In NiO/Pt bilayers, temperature-induced strain was identified as one of the switching mechanism induced by current injection [81].

The detailed description of the internal AFM DW structure remain a challenge due to the lack of sufficient experimental data. Recent work used advanced scanning diamond magnetometry to show the coexistence of Bloch and Néel DWs in Cr_2O_3 [18].

2.5 Imaging magnetic domains with magneto-optic effects

Magneto-optical (MO) effects describe how magnetic materials alter the polarization and intensity of light reflected or transmitted by the material itself. These effects have many useful applications, including the ability to probe and image magnetization orientation, study ultrafast magnetization dynamics, and observe domain wall motion [82, 83]. This section presents a phenomenological approach to introduce MO effects, following the methodology described in Ref. [76, 84]. We then describe in more details the configurations of the Magneto-Optical Kerr Effect (MOKE) microscope used in this thesis. The details about the components of the MOKE setup can be found in Sect. 3.4.

In all generality, we assume that light traveling through vacuum is an electromagnetic plane wave, with the electric field $\mathbf{E}$ perpendicular to the magnetic field $\mathbf{B}$. When light passes through a material, the time evolution of the electromagnetic field is governed by the displacement field $\mathbf{D}$, which is related to $\mathbf{E}$ through the complex

dielectric permeability tensor ϵ by the equation $\mathbf{D} = \epsilon\,\mathbf{E}$. This tensor encompasses all specific aspects of magneto-optical effects. For a crystal with cubic symmetry,

$$\epsilon = \epsilon_{\text{iso}} \underbrace{\begin{pmatrix} 1 & -iQ_{\text{V}}m_3 & iQ_{\text{V}}m_2 \\ iQ_{\text{V}}m_3 & 1 & -iQ_{\text{V}}m_1 \\ -iQ_{\text{V}}m_2 & -iQ_{\text{V}}m_1 & 1 \end{pmatrix}}_{\text{Faraday and Kerr effects}} + \underbrace{\begin{pmatrix} B_1 m_1^2 & B_2 m_1 m_2 & B_2 m_1 m_3 \\ B_2 m_1 m_2 & B_1 m_2^2 & B_2 m_2 m_3 \\ B_2 m_1 m_3 & B_2 m_2 m_3 & B_1 m_3^2 \end{pmatrix}}_{\text{Voigt effect}}, \tag{2.1}$$

where ϵ_{iso} is the dielectric constant of an isotropic non-magnetic material, and Q_{V} is the magneto-optical coefficient that describes the strength of the linear magneto-optical effect, which is roughly proportional to the saturation magnetization. m_{i} are the components of the magnetization vector $\mathbf{m}$, B_1 and B_2 are the coefficients of the intrinsic Voigt effect, which are identical for isotropic and amorphous materials [85]. The coefficients Q_{V}, B_1 and B_2 are complex numbers that depend on frequency. We note that the magnetic permeability is not involved because the frequency of visible light $\approx 500\,\text{THz}$ is several orders of magnitude larger than the ferromagnetic resonance frequency (Larmor frequency). Therefore, the magnetic moments cannot follow the alternating magnetic field of light, and only the description of $\mathbf{E}$ and $\mathbf{D}$ is relevant.

In Eq.2.1, the first part describes MO effects that are linear in magnetization, which can be utilized to image magnetization reversal in ferromagnets. These effects are referred to as Faraday or Kerr effects depending on whether the light is transmitted or reflected from the material. The Kerr effect has given rise to one of the most utilized optical apparatus in magnetism, the Magneto-Optical Kerr Effect (MOKE) microscope (see MOKE geometries below). The second part of Eq.2.1 describes MO effects that are quadratic in the magnetization. These effects can be utilized to observe the Néel vector of collinear antiferromagnets [50, 86].

Substituting Eq. 2.1 into Maxwell's equations, it can be shown that for light propagating along the magnetization direction, there exist two eigenmodes that are circularly polarized. Each circular mode has different indices of refraction, both real and imaginary, which result in two distinct effects. The difference in the real parts of the indices of refraction causes the two modes to propagate at different velocities, $\frac{c}{n'_+}$ and $\frac{c}{n'_-}$ respectively, with c the speed of light in a vacuum and $n'_{+,-}$ are the indices of refraction of the two modes. This difference results in a phase delay between the two modes as they propagate through the medium. As a result, the polarization axis of the incident light continuously rotates until it exits the material. This asymmetric

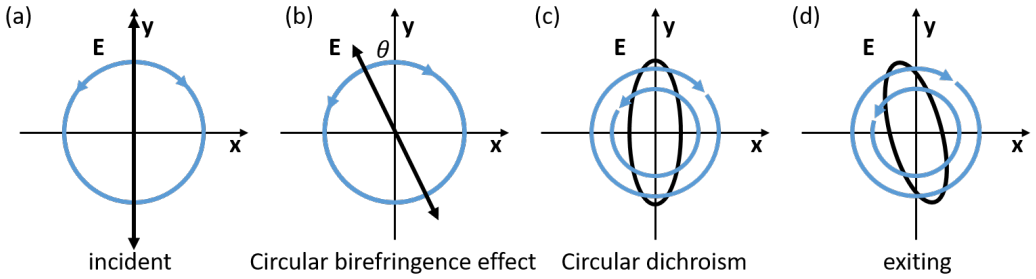

Figure 2.5: Schematic of the circular birefringence effect and circular dichroism on an incoming linearly polarized light. (a) The incoming linearly polarized light $\mathbf{E}$ can be decomposed into a superposition of two plane waves with opposite circular polarizations of equal amplitude (blue circles). (b) The circular birefringence effect rotates the polarization axis of $\mathbf{E}$. (c) The circular dichroism effect absorbs one circular polarization more than the other, thus inducing a recombined elliptically exiting light. (d) The polarization axis of the exiting light is rotated due to the circular birefringence and becomes elliptically polarized due to the circular dichroism.

optical effect is known as circular birefringence. On the other hand, the difference in the imaginary parts of the indices of refraction leads to different absorption rates, $\frac{\omega}{c}n''_+$ and $\frac{\omega}{c}n''_-$. In general, materials that exhibit anisotropic optical absorption of the partial waves are referred to as dichroic materials.

Consequently, if an incident linearly polarized light, which can be decomposed into a superposition of two plane waves with opposite circular polarization of equal amplitude, interacts with a ferromagnet, the polarization axis of the exiting light will be rotated due to the circular birefringence, and become ellipticaly polarized due to the circular dichroism, as illustrated in Figure 2.5.

2.5.1 MOKE geometries

There are three main Kerr configurations that can be used in MOKE microscopy depending on the orientation of the magnetization relative to the light indicidence direction [76]. The polar MOKE is used to measure or image the magnetization perpendicular to the surface, as illustrated in Figure 2.6-(a). It is most sensitive when the incident light is perpendicular to the surface and gives the largest Kerr signal. The longitudinal MOKE is used to image in-plane magnetization that is parallel to the plane of incidence of the light, as illustrated in Figure 2.6-(b). The longitudinal effect is possible with parallel p-polarized and perpendicular s-polarized light, with same amplitude but of opposite sign. The signal magnitude is proportional to the sine of the incident angle, $\sin\theta$, and therefore requires oblique incidence onto the surface.

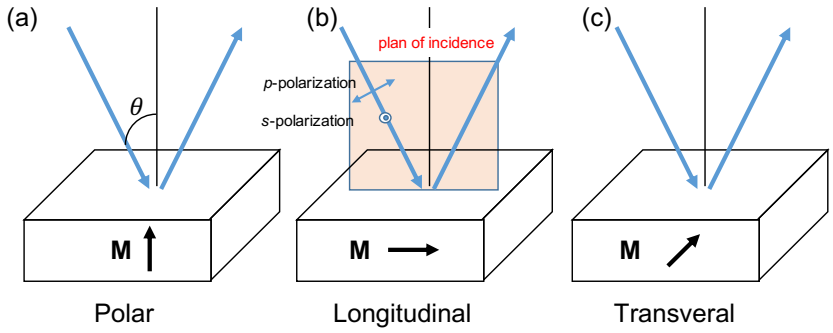

Figure 2.6: Schematic diagram of the MOKE configurations.

In fact, it is the component of $\mathbf{E}$ perpendicular to the magnetization that counts, which is the reason why the polar configuration is much easier than longitudinal MOKE. A third possibility is the transverse MOKE when the plane of incidence of the light is perpendicular to the magnetization, as illustrated in Figure 2.6-(c). The transverse MOKE causes an amplitude variation of the light, unlike the polar and longitudinal MOKE which cause Kerr rotation. To generate a measurable Kerr effect, the light has to be polarized at $45°$ to the plane of incidence. The perpendicular s-polarized light is not affected while the parallel p-polarization is modulated in amplitude, thus leading to an effective rotation.

2.6 Control of magnetic ordering by an applied field

2.6.1 Macrospin model

In the macrospin approximation, all spins are aligned, and the whole sample behaves as a single spin. In this approximation, called the Stoner-Wohlfarth model, the magnetization orientation at equilibrium is found by minimizing the sum of the Zeeman energy and magnetocrystalline anisotropy energy [87]. Under an external field, the time-dependent dynamics of the magnetization is described by the Landau-Lifshitz-Gilbert (LLG) equation [37],

$$\frac{\partial \mathbf{m}}{\partial t} = -\mu_0 \gamma \, \mathbf{H}_{\text{eff}} \times \mathbf{m} + \frac{\alpha}{|\mathbf{m}|} \mathbf{m} \times \frac{\partial \mathbf{m}}{\partial t}, \tag{2.2}$$

where μ_0 is the magnetic permeability, γ the gyromagnetic ratio, α the dimensionless damping parameter, and $\mathbf{H}_{\text{eff}}$ is the sum of the different fields acting on the

magnetization (external field, exchange interaction, dipole-dipole interaction, magnetocrystalline anisotropy). The first term describes the precession of $\mathbf{m}$ around the effective field $\mathbf{H}_{\text{eff}}$ axis at a speed proportional to the gyromagnetic ratio and the norm of $\mathbf{H}_{\text{eff}}$. The second term is the dissipative part of the equation which describes the reduction of the transverse component relative to the field axis.

2.6.2 Field-driven domain wall motion

The Stoner-Wohlfarth model is usually applicable in cases of very small particles, where the sample dimensions are comparable to the domain wall width, but it is often too simplistic to accurately describe the magnetization of larger samples. When performing an hysteresis loop while observing the magnetization reversal in thin films with a MOKE microscope, it becomes clear that the macrospin model does not hold. Close to the coercive field, domains nucleate in some locations of the sample and propagate. The nucleation occurs when the Zeeman energy and thermal energy are greater than the sum of the local anisotropy barrier and the energy required to form a domain wall surrounding the nucleated domain. Once nucleated, the external field can expand the domains until they merge with other domains or propagate across the entire sample.

A 1D-model of the domain wall motion in a defect-free sample was first proposed by Schryer and Walker in 1974 [88]. A sketch of the DW velocity v_{DW} as a function of external applied field is illustrated in Figure 2.7(a). In the low field region, the internal magnetization of the DW remains stable and the motion is in steady-state, which is the linear flow regime as the velocity is linearly proportional to the applied field. Past a critical field, called the Walker field $H_{\text{ext}} > H_{\text{W}} = \frac{\alpha M_{\text{S}}}{2}$, the internal domain wall magnetization starts to process around the field and alternates between Bloch and Néel domain walls. This precessional dynamics decreases the domain wall velocity in a non-linear fashion.

A more realistic model of field-driven DW motion needs to take into account local pinning barriers that can arise from inhomogeneities of the film thickness, the stoichiometric composition, or local stress [89]. These barriers act as anchors on the DW, impeding its motion. As a result, a minimum field, called the depinning field H_{d}, is needed to drive the DW across these sites. This depinning field shifts the DW velocity $v_{\text{DW}}(H_{\text{ext}})$ curve towards higher field. Additionally, at finite temperature, thermal fluctuations contribute to reducing the pinning barriers, which promote stochastic DW motion in the small driving field range, in this so-called creep regime,

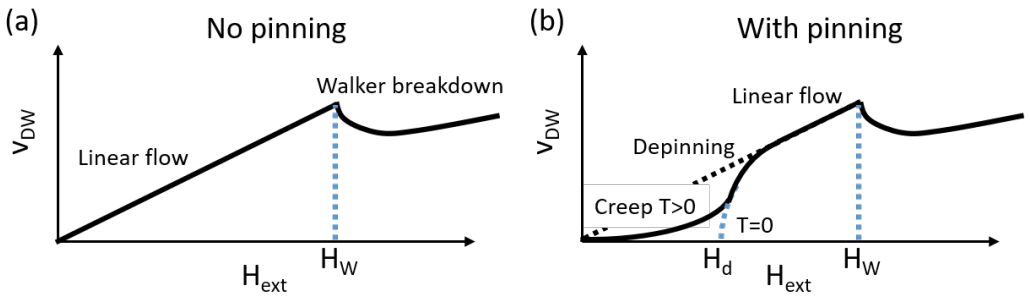

Figure 2.7: Field-driven domain wall velocity v_{DW} as a function of an applied external field along the easy-axis H_{ext}. (a) Motion in a defect-free sample which is characterized by a linear flow in the small field range and Walker breakdown at higher field $H_{\mathrm{ext}} \geq H_{\mathrm{W}}$. (b) Motion in a sample with pinning. In the small field range, thermal activation reduces the pinning energy barrier leading to the creep regime. At the depinning field H_{d} the velocity follows a power law increase until the linear flow regime.

v_{DW} follows an Arrhenius law. Overall, three main regimes are identified ranging from the smallest to the largest applied field [90, 91],

$$v_{\mathrm{DW}}(j) = \begin{cases} v_0 \exp\left(\frac{\Delta E}{k_{\mathrm{B}}T}\right) & \text{creep, } 0 \leq H_{\mathrm{ext}} < H_{\mathrm{d}}, \\ v_{\mathrm{d}} \left(\frac{H_{\mathrm{ext}} - H_{\mathrm{d}}}{H_{\mathrm{d}}}\right)^{\beta} & \text{depinning, } H_{\mathrm{ext}} \geq H_{\mathrm{d}}, \\ v_{\mathrm{d}} \frac{H_{\mathrm{ext}}}{H_{\mathrm{d}}} & \text{linear flow, } H_{\mathrm{ext}} \gg H_{\mathrm{d}}. \end{cases} \tag{2.3}$$

Here v_0 is a fitting parameter related to the material properties, $\Delta E = k_{\mathrm{B}} T_{\mathrm{d}} \left(H_{\mathrm{ext}}/H_{\mathrm{d}}\right)^{-\mu} - 1)$ describes the strength of the energy barrier with $\mu = 1/4$ the critical exponent that has been predicted and experimentally measured [92, 93, 94]. In the depinning regime, v_{d} is the velocity at the depinning threshold and $\beta = 0.25$ is another universal constant that has been experimentally measured [91]. Figure 2.7(b) shows v_{DW} as a function of external field with pinning.

2.7 Control of magnetic ordering by electric currents

Spintronic devices allow for magnetic ordering to be manipulated and detected by utilizing electric currents. To manipulate the magnetizazion, two primary types of effects can be identified, the spin transfer torque (STT) [95] and the spin-orbit torque (SOT) [56]. Both effects rely on the local interaction between spin-polarized conduction electrons and the magnetization. These effects can be used to induce magnetization switching in the sub-ns timescale, drive domain walls and probe the

magnetization orientation in various materials, including ferromagnets [56, 96], ferrimagnets [30, 28], and antiferromagnets [6].

2.7.1 Fundamentals of spin-orbit coupling

Spin-orbit coupling (SOC) is a relativistic phenomenon that describes the interaction between the spin of a particle and its motion in an electric field [37]. According to Maxwell's equations of electrodynamics and the Lorentz transformation of special relativity, a moving electron perceives a static electric field $\mathbf{E}$ as an effective magnetic field $\mathbf{B} = -\frac{1}{c^2}, \mathbf{v} \times \mathbf{E}$, where c is the speed of light and $\mathbf{v}$ is the speed of the electron. In a simple atomic model (Bohr representation), the electrons orbiting the nucleus experience the attractive electric field $\mathbf{E}$ of the nucleus as an effective field $\mathbf{B}$, which couples to the spin of the electron. The interaction energy is given by $\Delta H_{\mathrm{SO}} = \frac{\lambda}{\hbar^2}\mathbf{L}\cdot\mathbf{S}$, where λ is the coupling factor, $\hbar$ is the reduced Planck constant, $\mathbf{L} = \mathbf{r} \times \mathbf{p}$ is the orbital angular momentum, and $\mathbf{S}$ is the spin angular momentum. The coupling factor for a hydrogen-like atom depends on the atomic number, $\lambda \propto Z^4$, and the orbital fill factor [97]. Heavy elements such as Pt, Ta, and W exhibit larger SOC, which is beneficial for inducing large charge current to spin current, as discussed below.

2.7.2 Generation of spin currents by spin-orbit coupling

In conductors with large SOC, it has been theoretically predicted and experimentally demonstrated that the conduction electrons become spin polarized at the surface boundaries.This specific phenomenon relies on either an interfacial Rashba-Edelstein effect or on the bulk spin Hall effect.

The interfacial Rashba-Edelstein effect is due to symmetry breaking at the boundary of the conductor [98, 97]. In a centrosymmetric crystal, the conducting electrons moving at the surface (if in contact with vacuum) or at the interface (if in contact with an adjacent material) experience a different crystal field relative to the bulk of the conductor. The asymmetric crystal field vector $\mathbf{E}$ pointing in the direction normal to the surface couples to the electron spin via the SOC described above, which tends to align its spin in a plane perpendicular to its motion parallel to the effective magnetic field $\mathbf{B} \parallel \mathbf{v} \times \mathbf{E}$.

The bulk spin Hall effect (SHE) is a phenomenon that describes the conversion of charge current into spin current caused by spin-dependent scattering. The SHE

arises from three main mechanisms: skew scattering, and side-jump scattering and intrinsic contributions [99, 100, 101]. The first two mechanisms are considered extrinsic effects since the spin-dependent scattering events are caused by interactions with impurities and defects. These scattering interactions can be introduced as local potential barriers, $\nabla V(r)$, which couple to the electron spin via SOC. The third mechanism is the intrinsic SHE which does not involve scattering, but comes from the SOC in the band structure itself [100]. Overall, these three mechanisms convert a charge current into an accumulation of spin polarized charges at the boundaries.

2.7.3 Current-driven DW motion by spin-orbit torques

In this section, we discuss the electrical manipulation of magnetic order via spin-orbit torques (SOT). As described above, conducting electrons in heavy metals are spin-polarized at the surface boundaries due to SOC. These spin-polarized charges diffuse and interact with the magnetization of the adjacent layer via exchange coupling, generating two types of magnetic torques that are perpendicular to each other: the field-like torque and the damping-like torque [102].

For an electric current flowing in-plane along the current density vector $\mathbf{j} \parallel \mathbf{x}$, the spin polarization is $\boldsymbol{\sigma} \parallel \mathbf{y}$. In this configuration, the field-like torque is $\boldsymbol{\tau}_{\mathrm{FL}} \sim \mathbf{m}(\mathbf{z} \times \mathbf{j}) \sim \mathbf{m} \times \mathbf{y}$, with $\mathbf{z}$ pointing normal to the surface. $\boldsymbol{\tau}_{\mathrm{FL}}$ is comparable to an effective field parallel to the spin polarization $\boldsymbol{\sigma}$ and is independent of the magnetization direction. Its effect makes $\mathbf{m}$ precess.

The damping-like torque is $\boldsymbol{\tau}_{\mathrm{DL}} \sim \mathbf{m}(\mathbf{z} \times \mathbf{j} \times \mathbf{m}) \sim \mathbf{m} \times (\mathbf{y} \times \mathbf{m})$. $\boldsymbol{\tau}_{\mathrm{FL}}$ and $\boldsymbol{\tau}_{\mathrm{DL}}$ are always perpendicular to the magnetization direction. The ratio of the DL and FL components depends on the materials and the interface properties between the heavy metal and the magnetic material. For convenience, it is possible to define the field-like and damping-like fields by taking the product $\mathbf{m} \times \boldsymbol{\tau}$. Hence, $\mathbf{B}_{\mathrm{FL}} = B_{\mathrm{FL}}\,\mathbf{y} \parallel \boldsymbol{\sigma}$, and $\mathbf{B}_{\mathrm{DL}} = B_{\mathrm{DL}}\,\mathbf{y} \times \mathbf{m}$.

Let us now discuss the effects of these torques on the DWs. As discussed in Sect.2.4, Bloch-type and Néel-type DW configurations can be energetically favorable in magnetic thin films. In a coordinate system where the current flows along $\mathbf{x}$ and the $\mathbf{y}$-axis and $\mathbf{z}$-axis are in-plane and out-of-plane, respectively, the internal magnetization of Bloch DW is parallel to $\mathbf{y}$, which is parallel to $\boldsymbol{\sigma}$ and therefore $\mathbf{B}_{\mathrm{DL}} \approx 0$. The resulting torque on the DW magnetization vanishes and the DW does not move. However, when a longitudinal field is applied parallel to the current, $\mathbf{B}_{\mathrm{x}} \parallel \mathbf{j}$, the internal magnetization of the DW rotates towards $\mathbf{x}$, transforming the Bloch DW into a Néel DW, which maximizes the torque [103].

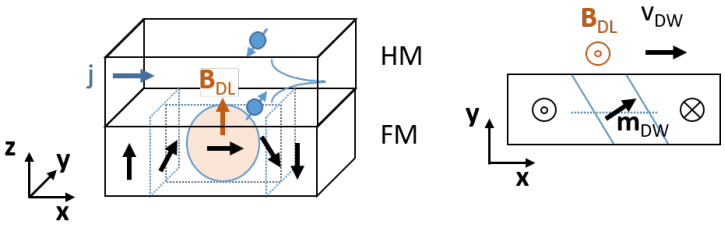

Figure 2.8: Current-driven DW motion by SOT. Schematic of the the damping-like field $\mathbf{B}_{\mathrm{DL}}$ acting on a right-handed chiral Néel DW wall. $\mathbf{B}_{\mathrm{DL}}$ acts as an effective field along $\mathbf{z}$ which triggers the propogation along $\mathbf{x}$. It also rotates the DW magnetization $\mathbf{m}_{\mathrm{DW}}$ along $\mathbf{y}$ causing titling of the DW because the DMI field favors $\mathbf{m}_{\mathrm{DW}}$ perpendicular to the DW. The tilt reduces the DW velocity because $\mathbf{B}_{\mathrm{DL}}$ is maximal when $\mathbf{m}_{\mathrm{DW}} \parallel \mathbf{x}$ and minimal when $\mathbf{m}_{\mathrm{DW}} \parallel \mathbf{y}$.

In addition to the external field, the interfacial DMI can favor a Néel DW as it acts like an effective field $\mathbf{B}_{\mathrm{DMI}} \parallel \mathbf{x}$ (see in Sect. 2.4). In a Néel DW configuration, $\mathbf{B}_{\mathrm{DL}}$ generates an effective field along $\pm\mathbf{z}$ that depends on the sign of $\boldsymbol{\sigma}$ and the DW magnetization. The rotation of the internal DW magnetization $\mathbf{m}_{\mathrm{DW}}$ towards $\mathbf{z}$ triggers the propagation of the DW. The DL torque also induces a rotation of $\mathbf{m}_{\mathrm{DW}}$ towards $\mathbf{y}$, causing the tilting of the DW. This is because the DMI favors $\mathbf{m}_{\mathrm{DW}}$ to be perpendicular to the DW [104, 49, 105], as illustrated in Figure 2.8. The amplitude of B_{DL} is decreased by the internal rotation towards $\mathbf{y}$ since it is maximal when $\mathbf{m}_{\mathrm{DW}} \parallel \boldsymbol{\sigma} \parallel \mathbf{x}$ [105]. The Oersted field $\mathbf{B}_{\mathrm{Oe}}$ also generates an effective field along $\mathbf{y}$, which can increase or decrease the domain wall velocity v_{DW} depending on whether it adds or subtracts from the rotation of $\mathbf{m}_{\mathrm{DW}}$ along $\mathbf{y}$ induced by $\mathbf{B}_{\mathrm{DL}}$. $\mathbf{B}_{\mathrm{FL}}$ generates an effective field along $\mathbf{y}$, affects the domain wall velocity v_{DW} in the same manner as the Oersted field.

When a current is applied, the DW initially accelerates and the internal magnetization tilts before reaching a constant velocity at steady-state. Analytic expressions for v_{DW} were derived for a simplified $q-\phi$ model with two collective coordinates, namely the position of the DW (q) and the tilting angle of $\mathbf{m}_{\mathrm{DW}}$ with respect to the current (ϕ), neglecting the effects of $\mathbf{B}_{\mathrm{FL}}$ and $\mathbf{B}_{\mathrm{Oe}}$ [47, 49, 106]. The resulting equation for v_{DW} is

$$v_{\mathrm{DW}} = \frac{\pi}{2}\gamma\Delta \frac{B_{\mathrm{DL}}}{\sqrt{\alpha^2 + (\frac{B_{\mathrm{DL}}}{B_{\mathrm{DMI}}+B_{\mathrm{x}}})^2}} = \frac{\pi}{2}\gamma\Delta \frac{B_{\mathrm{DL}}\left(B_{\mathrm{DMI}}+B_{\mathrm{x}}\right)}{\sqrt{\alpha^2\left(B_{\mathrm{DMI}}+B_{\mathrm{x}}\right)^2 + B_{\mathrm{DL}}^2}}, \tag{2.4}$$

where γ is the gyromagnetic ratio, $\Delta = \sqrt{A_{\mathrm{ex}}/K_{\mathrm{eff}}}$ is the DW width, α is the damping factor. Equation 2.4 can also be expressed in terms of the current density with $\eta\, j = B_{\mathrm{DL}}$ with η the current-to-torque conversion factor.

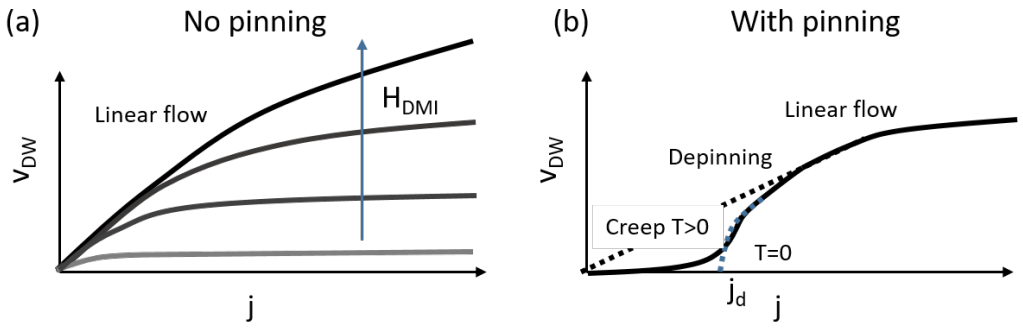

Figure 2.9: Current-driven DW velocity by SOT as a function of applied current. (a) The motion in a defect-free sample is characterized by a linear flow regime in the small current range, followed by saturation of the velocity in a larger current range. (b) DW motion in a sample with pinning. In the small current range, thermal activation reduces the pinning energy barrier leading to DW creep. At the depinning current j_d, the velocity follows a power law increase until linear flow and eventually saturation, as seen in the defect-free sample (a).

Qualitatively, v_DW shows a linear increase in the small current density regime known as the flow regime, followed by a saturation of v_DW in the larger current density regime, as illustrated in Figure 2.9(a). The flow regime is proportional to j, which is in agreement with the flow regime observed in field-driven DW motion, because $B_\mathrm{DL} \parallel \mathbf{z}$ is essentially equivalent as applying an external field $B_\mathrm{ext} \parallel \mathbf{z}$ (Section 2.6.2). The saturation at larger current density occurs when $\mathbf{m}_\mathrm{DW}$ rotates to form a Bloch DW.

In Eq. 2.4, the DMI and external fields contribute equally to v_DW. The effect of B_DMI is to stabilize the Néel DW, with higher values maintaining the Néel DW configuration until higher current densities, resulting in large saturation velocity [47], as illustrated in Figure 2.9(a). On the other hand, B_x can either reinforce or oppose B_DMI, leading to a decrease in DW velocity until it stops moving at $B_\mathrm{x} = -B_\mathrm{DMI}$. This is a particularly useful experimental method for estimating the effective amplitude of B_DMI. We used this technique in Chap. 5 to estimate the DMI in a Cr_2O_3/Co/Pt trilayer.

In this model, the width of the DW $\Delta = \sqrt{A_\mathrm{ex}/K_\mathrm{eff}}$ is assumed to be constant. It contributes linearly to the velocity, such that wider DWs move faster than narrow DWs. This can be explained intuitively by considering a scenario where one DW is made of a single spin, while another DW is made of tens of spins. When a current is applied, each spin rotates by a certain angle towards $\mathbf{z}$ due to the action of B_DL. Therefore, if the current is applied for a duration long enough to allow the full rotation of the single spin DW, the same current would allow the rotation of a DW

with tens of spins. Hence, the displacement of the DW is linearly proportional to Δ.

Taking into account the pinning barriers is important to describe the DW motion in the small current range. As described for field-driven DW motion (see in Chap. 2.6.2), pinning sites impede the DW motion. Similarly to the behavior described for field-driven DW motion [91, 89, 107, 108], a universal behavior can be developed for current-driven DW motion by SOT in the presence of pinning [109],

$$v_{\mathrm{DW}}(j) = \begin{cases} v(j_{\mathrm{d}})\ \exp\left(-\frac{\Delta E}{k_{\mathrm{B}}T}\right) & \text{creep, } 0 \leq j < j_{\mathrm{d}} \\ \frac{v_{\mathrm{T}}(j_{\mathrm{d}})}{x_0}\ \left(\frac{j-j_{\mathrm{d}}}{j_{\mathrm{d}}}\right)^{\beta} & \text{depinning, } j \geq j_{\mathrm{d}} \\ v_{\mathrm{T}}(j_{\mathrm{d}})\ \frac{j}{j_{\mathrm{d}}} & \text{linear flow, } j \gg j_{\mathrm{d}} \end{cases} \tag{2.5}$$

where j_{d} is the depinning current threshold, $v(j_{\mathrm{p}})$ is the velocity at the depinning threshold, $\Delta E = k_{\mathrm{B}}T[(j/j_{\mathrm{d}})^{-\mu} - 1]$ is the energy barrier height. $v_{\mathrm{T}}(j_{\mathrm{d}}) = v(j_{\mathrm{d}})(\frac{T_{\mathrm{d}}}{T})^{\psi}$ is the hypothetical velocity in the absence of pinning. The critical exponent $\mu = 1/4$, $\beta = 0.25$ and $\psi = 0.15$, and the parameters $x_0 = 0.65$ are the same universal exponent found field-driven DW motion [109] [see in Sect. 2.6.2]. The creep, depinning and flow regime are schematized in Figure 2.9(b). Overall the current-driven DW motion by SOT has qualitative similarities as the field-driven DW in the small current and field regime.

2.8 Current-induced switching of antiferromagnets

In Chapter 4, Sect. 4.2, we provide a detailed description of the electric writing and reading scheme of antiferromagnets. We present the state-of-the-art knowledge until mid-2020 on the electric pulsing and reading geometries, as well as the underlying physical effect involved. We discuss the origin of the resistance changes that occur after pulsing, including the magnetic effects caused by the reorientation of the AFM domains and the nonmagnetic effects caused by annealing and electromigration.

In late 2020, a new research investigated the contribution of current-induced spin-orbit torques, heat, and thermomagnetoelastic effects in NiO/Pt thin films [81]. They fabricated high-quality NiO(001)(10 nm)/Pt(2 nm) bilayers epitaxially grown on MgO(100) substrates. Unlike previous reports [12, 13], where the antiferromagnetic domains were relatively small, in their samples, the domain sizes were in the range of tens of μm. The larger domains were imaged using MOKE microscopy, which helped gain a clearer understanding of the antiferromagnetic switching mechanism,

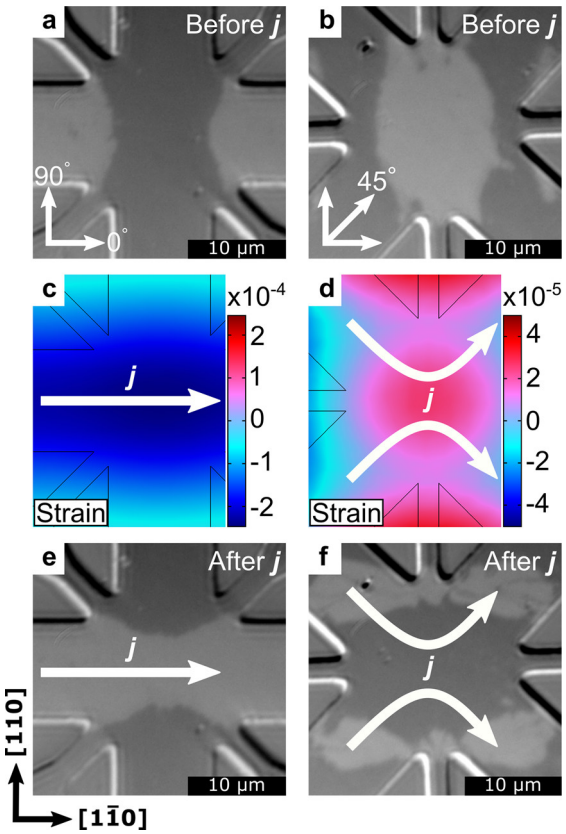

Figure 2.10: Figure taken from Ref. [81]. Comparison of the switching between different device geometries in NiO/Pt epitaxially grown on MgO substrates. Kerr images of the initial domain structure in the star device with easy-axis along [110] (a) and [100] (b). Simulations of the current-induced strain for a straight pulse along $[1\bar{1}0]$ in the [110] star device (c) and for X-shaped pulses along $[1\bar{1}10]$ in the [100] star device (d). Domain structure in the [110] star device (e) and [100] star device (f) after applying five pulses in the directions indicated in (c) and (d).

as shown in Figure 2.10. Based on the comparison of transport and magneto-optical measurements, the researchers concluded that the AFM switching is not solely dependent on the current direction but rather on the device geometry. They discovered that a combination of strain and heat enables the switching, with strain breaking the degeneracy and defining the final state, while heating is necessary to assist the switching by overcoming the anisotropy barrier. In mid-2021, direct imaging of current-induced switching in α-Fe_2O_3 epitaxially grown on Al_2O_3 was observed using XMLD-PEEM [110]. The researchers observed reorientation of the AFM domains both along and outside the current path, suggesting that thermally induced magnetostriction may play a significant role in the current-induced switching of antiferromagnetic domains.

2.9 Generation of torques by injection of orbital current

In Sections 2.7.2 through 2.7.3, we explain the generation of torques in ferromagnetic (FM) materials through the injection of a spin current from adjacent nonmagnetic (NM) materials with spin-orbit coupling (SOC). Recently, the injection of an orbital current was predicted as an alternative means to generate torques in FM, called orbital torques [111, 112, 113]. An orbital current describes the flow of orbital angular momentum, analogous to the spin current. The effect can originate from the orbital Hall effect (OHE) where a charge current gives rise to a transverse orbital current [114, 115]. The OHE does not require strong SOC, making it present in a wide range of materials. The amount of generated orbital current is given by the orbital Hall conductivity, which interestingly can be several orders of magnitude larger than the spin Hall conductivity [116, 117], providing a means to achieve high torque efficiency.

Differently from the spin current, which acts on the magnetization via exchange coupling, the orbital current does not couple directly to the magnetization. Instead, it requires conversion into a spin current by SOC [111]. The conversion of the orbital current into a spin current eventually allows it to interact with the magnetization via the exchange coupling, resulting in orbital torques that generate a field-like and a damping-like torques with the same symmetries as the spin torques. This makes it difficult to differentiate between spin and orbital torques. To demonstrate the existence of orbital torques, several experimental approaches have been pursued.

One approach relies on measuring torques in FM/NM bilayers with the FM layer having strong SOC to convert the orbital current, and comparing it with another FM with weak SOC [111]. These measurements revealed large torques in Ni/Cr bilayers compared to Co/Cr because the SOC is larger in Ni than in Co [118]. Another approach is to measure the torques as a function of the NM thickness, which should gradually increase and saturate for thicknesses above the orbital diffusion length [118]. A different approach relies on inserting a conversion layer X with strong SOC in between the layers to form a FM/X/NM trilayer. The orbital current from the NM layer is converted into a spin current by the X layer because of its SOC. Large torques have been measured using Gd,Tb and Pt, as the conversion layer in Co/(Gd,Tb)/Cr trilayers [118] and in CoFeB/Pt/Cr [119]. In this trilayer configuration, the presence of a conversion layer X also generates spin current through the SHE, which contributes to the torques. Since the torques were much larger in the FM/X/NM trilayers than in the test samples made of FM/X and FM/NM bilayers, it has been concluded that the conversion layer X harvests the orbital

current from the NM layer. Finally, the competition between orbital torque and spin torque in FM/NM bilayers can be investigated by varying the SOC in the FM via its stoichiometry, as proposed in [111]. Rare-earth transition-metal ferrimagnetic alloys could be used instead of FM, as RE compounds have strong SOC, and altering the relative content of RE and TM can change the SOC in the magnetic layer. In Chapter 6, we will study domain wall motion in $Co_{1-x}Gd_x$ via orbital injection from an adjacent Cr layer. By increasing the Gd content, we expect an increase in the SOC of CoGd and thus measure an increase in the generated torques by Cr, resulting in high domain wall velocity. To the best of our knowledge, no experimental evidence of this effect has been reported yet.

3 Methods

This chapter describes the methods used for the growth of samples, the fabrication of devices, the electrical transport measurements, and the magneto-optical Kerr microscopy technique used for magnetic domain imaging. In addition to these techniques, we also analyze the time trace of the voltage across the device during the pulsing experiment and estimate the temperature increase due to current-induced Joule heating.

3.1 Thin-film deposition and characterization

Dr. Charles-Henri Lambert, and Dr. Min-Gu Kang, deposited and characterized the samples studied in Chapter 4-5, and Chapter 6 respectively. I deposited and characterized samples that were used for calibration of the deposition rates.

The samples studied in this thesis consist of stacks of thin films of nonmagnetic and magnetic materials. The films are grown on dielectric substrates with a custom-built sputter deposition system (PLASSYS MP800s). Sputter deposition is a physical vapor deposition technique that allows for depositing insulators (oxides), semiconductors, and metals. It operates with energetic Ar atoms hitting the atoms of the targets and propelling them towards the substrate in a vacuum chamber. An electric field inonizes the Ar in plasma between a cathode (target) and an anode (substrate). Typically, the Ar pressure during the growth is a few mTorr and the base pressure $\approx 10^{-7} - 10^{-8}$ mTorr. The sputtered atoms are not ionized and travel ballistically or diffusively towards the substrate. A permanent magnet placed on the cathode confines the Ar+ close to the target due to Lorentz forces, which increases the sputter efficiency. This technique is called DC magnetron sputtering and is used for depositing metals. It is unsuitable for insulators since the Ar+ would accumulate on the surface of the target and repel other positive ions, eventually stopping the sputtering process. RF magnetron sputtering instead uses an alternating RF electric field, which removes charge buildup with each cycle.

After deposition, the crystal structure of the films is investigated by x-ray diffraction (XRD) and their thickness is measured via x-ray reflectivity. Typically, X-ray diffrac-

tion (XRD) 2θ-scans are performed to evaluate the degree of crystallinity and the epitaxial growth. The in-plane symmetries of the crystal structures are measured by XRD azimuthal ϕ-scans. Eventually, atomic force microscopy is used to measure the surface roughness.

3.2 Fabrication of devices

After completing the characterization of the sample, we fabricated micrometer-sized devices using optical photolithographic techniques. The samples are first cleaned in an ultrasonic bath using acetone and then isopropanol for approximately 5 min. Next, a layer of resist (ma N1420) is applied to the sample by spin-coating for 45 s at 4000 rpm and then annealed for 125 s at $120°$. The samples are then ready for exposure using a manual mask aligner and a UV broadband source at 400 nm (MJB3) with a power of 200 W for 35 s. We then use a developer solution (ma D533S) for 40 seconds while agitating the sample and checking under a microscope to ensure that the non-exposed resist is removed. If necessary, the samples can be developed for additional 5 s intervals until all the non-exposed resist is completely removed. After development, the devices are fabricated by reactive ion etching (RIE 80), continuing until the last conducting layer is removed to guarantee that the electric current flows exclusively through the device. Finally, the samples are cleaned and sonicated in acetone and isopropanol to remove any residual resist.

3.3 Electrical setup

For magneto-transport measurements, a current source (Keithley 6221 DC/AC) is used to apply a sensing current to the devices. The devices are wired-bonded and mounted on motorized sample holders for angle-scan and field-scan measurements in electromagnets capable of producing fields of up to 2 T. Measurements using an AC current of 10 Hz are typically performed to retrieve the first and second harmonics of the Hall and longitudinal resistance, which give the linear and quadratic response of the device, respectively odd and even response with the current direction. The acquisition time for these measurements is typically between 0.5 and 2 s.

For the electrical switching of antiferromagnets with voltage pulses, a voltage pulse generator (Agilent 8114A) is used to generate pulses of length between 50 ns and 1 ms with a nominal rise time of approximately 50 ns and pulse amplitude between

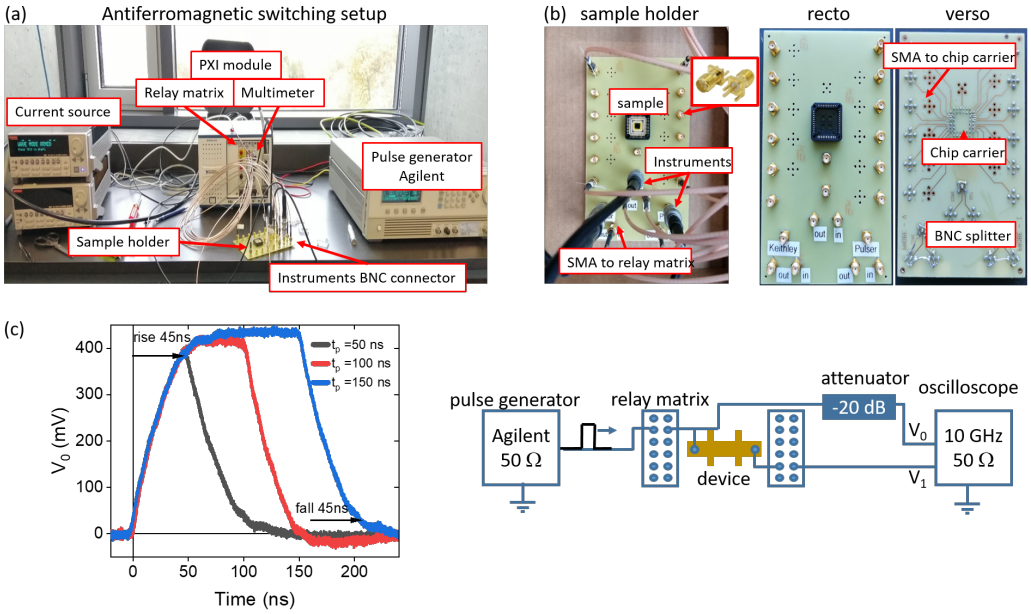

Figure 3.1: (a) Setup configuration of the antiferromagnetic switching experiment (see text for details of the instrumentation). (b) Homemade PCB with the sample holder (top) and BNC to SMA cable splitters (bottom). Each SMA port is connected to a relay that reroutes the sensing and pulsing path along any direction of the device. (c) Time traces of the voltage applied to a Hall bar device made NiO(10 nm)/Pt(5 nm) deposited on SiO_2 with a resistance of 600 Ω (device studied in Chap. 4), when applying pulses of different nominal lengths (50 ns, 100 ns, 150 ns) and a pulse amplitude of 42 V. The rise-time and fall-time for the three different pulse lengths is approximately 45 ns. Schematic of the electric setup to measure the time trace on the right side

2 V and 50 V. In this experiment, it is also necessary to reroute the sensing current and voltage pulses along different directions of the device. To do this, a setup is built with an RF signal relay matrix (PXIe-2541) with high-frequency transmission to control the current path in the device by setting which arms are connected to the instruments, floating, or grounded. A picture of the setup is shown in Figure 3.1-(a). A chassis (PXIe-1071) holds the modules and connects to the current source and pulse generator via GPIB connectors.

A PCB board is fabricated to split the core part (signal) from the outer part (ground) of the BNC cables of the instruments into two separate SMA connectors, as shown in Figure 3.1-(b). These SMA connectors are individually connected to the matrix inputs (with a maximum of twelve) via shielded SMA cables. The matrix outputs (with a maximum of eight) are connected to the device via shielded SMA cables. The overall synchronization of the instruments, rerouting of the path, and recording of the data are managed through an in-house-developed Matlab interface.

In Chapter 5 and 6, the magnetic domain wall motion experiments were conducted using a sample holder mounted on a wide-field MOKE microscope setup shown in Figure3.2(a). To minimize the temperature increase induced by Joule heating, these experiments required the use of shorter voltage pulses. The pulse generator (Kentech UTV100P) applied pulses with lengths ranging from 1 ns to 100 ns, amplitudes between 2 V and 55 V, and a nominal rise time of approximately 300 ps. The device was directly connected to the pulse generator, eliminating the need for a relay matrix. The sample holder, illustrated in Figure 3.2(b), consisted of a PCB chip with gold pads soldered to a coaxial cable (RG/U 50 Ω). Since the device resistance was often greater than 50 Ω, an impedance mismatch between the pulse generator and the device resulted in significant pulse shape distortions, which were observed in the voltage time trace shown in Figure 3.2(c). To mitigate this undesired effect, a 50 Ω SMD resistor was wire-bonded in parallel to the device, as indicated by the black rectangle in Figure 3.2(b).

3.3.1 Time trace of the voltage pulses

We conducted a study of the device response across a wide range of pulse lengths and amplitudes. To ensure that the device was receiving the intended pulse shape, it was essential to accurately measure the time trace of both the applied and transmitted voltage. For this purpose, we use an Agilent Infiniium DSO81304A oscilloscope, with 10 GHz sampling rate and $50\ \Omega$ internal resistance. The applied voltage is measured with one channel of the scope connected to a bias-T in parallel with the generator and sample holder, as shown in the electrical diagrams in Figure 3.1-(c) and Figure 3.2-(c). An attenuator is used to lower the voltage below the maximum input of the oscilloscope. To measure the transmitted voltage, a second channel of the oscilloscope is connected in serie between the device output and ground.

Figure 3.1(c) shows the pulse signal in the experimental antiferromagnetic switching setup, consisting of the Agilent pulse generator, relay matrix, and PCB sample holder. The pulse length are set to $\tau_p = 50, 100, 150$ ns and the pulse amplitude is set to 42 V. The device is a Hall bar with a width of $10 - \mu$m patterned on an Al_2O_3/Pt(5 nm) sample. The 2-points resistance is $\approx 200\ \Omega$. The applied pulse has a square shape with a rise/fall time ≈ 45 ns, while the pulse rise/fall measured directly at the Agilent output (not shown) is ≈ 10 ns. This behavior is a signature of parasitic capacitance, which can come from two things. First, the PCB sample holder is not designed for $50\ \Omega$ impedance matching. Second, BNC splitters consist of SMA female connectors soldered to the PCB. The core is a pin surrounded by the four ground pins, as shown in the inset of Figure 3.1(b), and these pins can add parasitic

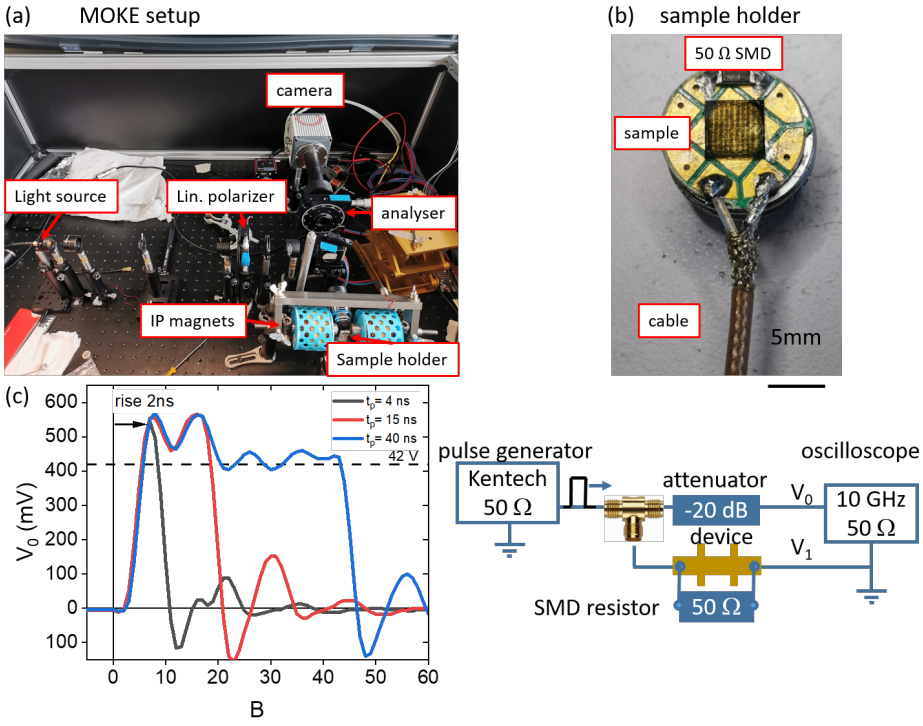

Figure 3.2: (a) Setup configuration of the wide-field MOKE system. (b) The sample holder is a PCB with the sample placed in the center. A device is wire-bonded to a gold pad on the PCB. To reduce the impedance mismatch, a $50\ \Omega$ SMD resistor is wire-bonded in parallel to the device. A coaxial cable (RG/U $50\ \Omega$) is connected to the voltage generator and soldered to the PCB holder. (c) Time traces of the voltage applied to a racetrack device made Cr_2O_3(120 nm)/Co(0.85 nm)/Pt(2 nm) deposited on Al_2O_3 with a resistance of 1200 Ω (device studied in Chap. 5), when applying pulses of different nominal lengths (4 ns, 15 ns, 40 ns) and a pulse amplitude of 40 V. The rise-time and fall-time for the three different pulse lengths is approximately 2 ns. Schematic of the electric setup to measure the time trace on the right side.

capacitance. We tested the setup without the relay matrix and observed a similar rise/fall time (not shown), demonstrating the relay matrix adds small parasitic capacitance. Interestingly, such a long rise time gives the advantage that reflections and voltage ringing [see in Figure 3.2(c)] due to impedance mismatch are almost completely flattened. Considering the rise time ≈ 45 ns (AFM configuration), we limited our study to pulse lengths of duration $\tau_p \geq 100$ ns.

Figure 3.2(c) shows the time trace of the applied pulse in the experimental MOKE setup, consisting of the Kentech pulse generator and the PCB sample holder shown in Figure 3.2(a). There is no relay matrix. The device is a double Hall bar with a width of $5 - \mu$m patterned on an $Al_2O_3/Cr_2O_3(120\ \text{nm})/Co(0.85\ \text{nm})/Pt(2\ \text{nm})$ sample. The 2-points resistance is $\approx 1600\ \Omega$. The pulse has a square shape with a rise/fall time ≈ 2 ns, while the pulse rise/fall measured directly at the Kentech

output (not shown) is ≈ 0.5 ns. As discussed above, the larger rise time is probably due to parasitic capacitance from the PCB sample holder. The transient oscillations (ringing) of the applied voltage seen in the graph are due to impedance mismatch and parasitic impedance and capacitance. Considering the rise time ≈ 2 ns (AFM configuration), we limited our study to pulse lengths of duration $\tau_{\mathrm{p}} \geq 4$ ns.

3.3.2 Estimate of the device temperature during the pulse

High pulse amplitudes are often required during our experiments of spin-orbit torque (SOT) switching and domain wall motion. This can result in significant heat being generated in the conductive materials due to Joule dissipation. The amount of heat generated is directly proportional to the square of the current flowing through the conductive material and the material's resistance. The heat is mainly dissipated through conduction via the substrate, while radiation and convection play a minor role [120]. In a simplified model, the rate at which heat diffuses through the substrate is determined by the thermal diffusion coefficient, represented by the equation $\alpha = \kappa/(c\,\rho)$, where κ, c and ρ are the thermal conductivity, the specific heat and the density of the substrate, respectively. This coefficient can be thought of as a measure of the substrate's thermal inertia, with a small coefficient indicating that the substrate will heat and cool quickly, and a large coefficient indicating the opposite. However, it should be noted that while ρ is generally constant as a function of temperature, κ and c can vary with temperature, implying that the heat diffusivity is not constant during the pulse, which makes it difficult to analytically derive or even computationally model the temperature change in the device.

The device resistance can be experimentally estimated by monitoring the changes in longitudinal resistance during the pulse and comparing these changes to the device resistance measured as a function of temperature [121]. To measure the device resistance, the electrical configuration described above for measuring the applied and transmitted voltage can be reused. In this configuration, one channel of the oscilloscope is connected to the device input pad, denoted as V_0, and a second channel is connected after the device and ground, denoted as V_1. The time trace and schematic can be seen in Figure 3.3(a)-(b). The device and the second channel are connected in series, meaning that the transmitted voltage, V_1, is given by $V_1(t) = 50/[50 + R_{device}(t)]V_0(t)$, where the $50\ \Omega$ is for the internal channel resistance. If we assume that the internal resistance does not change during the pulse (i.e. no heat-induced changes in resistance), the evolution of the device resistance during the pulse is given by $R_{device}(t) = 50\,[V_1(t)/V_0(t) - 1]$. To relate this to temperature, the longitudinal resistance can be calibrated by heating the

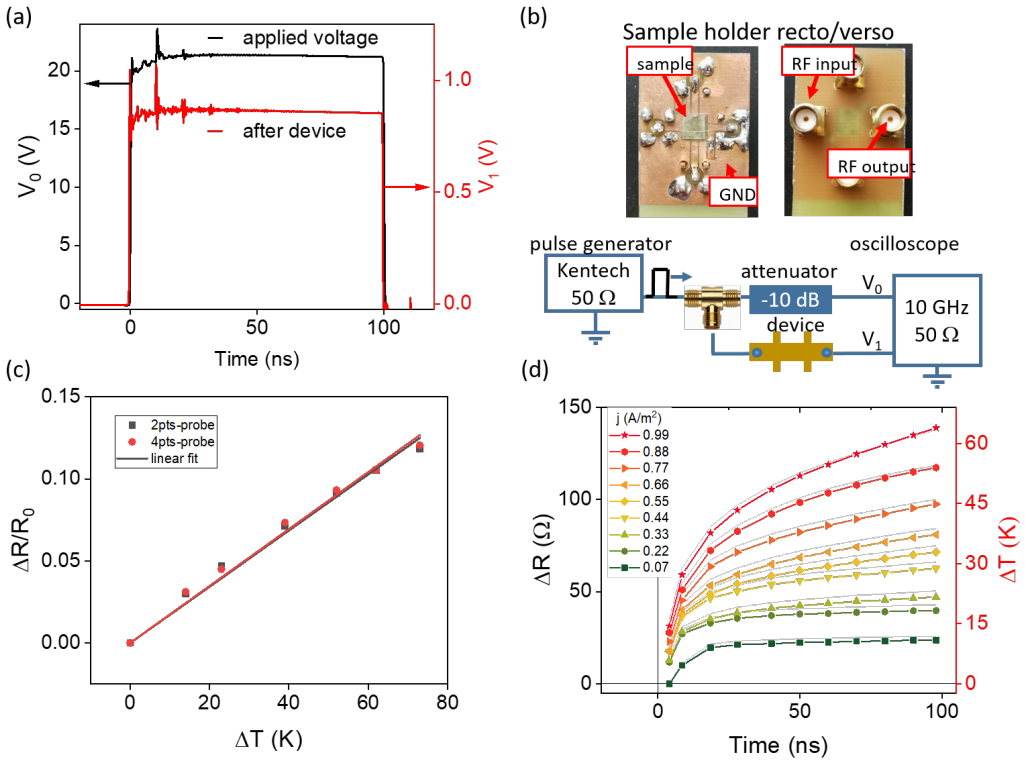

Figure 3.3: Estimate of the temperature increase due to Joule heating. The device is a race-track made of YIG(10 nm)/ TmIG(20 nm)/ Pt(5 nm) grown on $Gd_3Sc_2Ga_3O_{12}$ (GSGG) substrate. (a) Time trace of the applied and transmitted voltage across and (b) electric setup. (c) Calibration of the device resistance as a function of increasing temperature. The sample is heated on a heating stage and the temperature is recorded next to the sample. (d) Device resistance (left-axis) and estimated device temperature (right-axis) during the pusle. The colors indicate different current densities calculated from the device base resistance at room temperature $R_0 = 1130\ \Omega$ and the set voltage.

sample on a heating stage. The sample is fixed with a piece of Kapton tape and the Pt-100 thermistor placed next to it to measure the temperature as accurately as possible. The longitudinal resistance is measured with 4-point probes (using a small sensing current) and the thermistor is measured with a multimeter, as shown in Figure 3.3(c). Several loops of temperature increase and decrease are recorded to ensure that the resistance change is reproducible. For example, it was observed in some samples that certain metals can oxidize or anneal, producing irreversible changes in resistance. This method requires an applied voltage to measure the longitudinal resistance, therefore the device resistance is unknown before or after the pulse. Before the pulse, it can be easily assumed that the device resistance is the same as at room temperature. After the pulse, it can be assumed that the cooling rate follows a trend opposite to the heating rate, returning to room temperature after a time comparable to the pulse duration [120].

We used this method to estimate the temperature increase in racetrack devices made of YIG(10 nm)/ TmIG(20 nm)/ Pt(5 nm) trilayers grown on (111) oriented $Gd_3Sc_2Ga_3O_{12}$ (GSGG). The results were used in Ref.[34] to understand the role of thermal activation during current-induced skyrmion motion. We were able to estimate the increase under a pulse length range of 10 ns to 100 ns and a current density range of $1 \cdot 10^{11}$A/m^2 to $1 \cdot 10^{10}$A/m^2, as shown in Figure 3.3(d). The pulses start at time 0 ns and the color indicates different current densities. The left axis illustrates the device resistance with the base resistance of the device at 295K ($R_0 = 1130\ \Omega$). The right axis illustrates the corresponding increase in temperature, as calculated from calibration measurements.

3.4 MOKE microscope

We use a home-built Magneto-Optic Kerr Effect (MOKE) microscope to measure magnetic hysteresis loops, field-driven and current-driven domain wall motion in ferromagnetic devices. The LED light source (Prizmatix Mic-LED-455L, 100mW) emits blue light with a wavelength of $\lambda = 455 \pm 24$nm. The objective (Zeiss EV Epiplan-Noefluar 50x/0.8 Pol M27) has a numerical aperture of $NA = 0.8$. Due to the Abbe diffraction limit, the theoretical minimum resolvable distance is $d = \lambda/2NA \approx 282$ nm, while in practice the spatial resolution is ≈ 350 nm. The optical alignment is based on the so-called Köhler illumination, which is designed to eliminated the variations in the intensity or angle of incidence of the light that would otherwise cause optical aberration or distortion in the image [76]. The reflected light is captured by a water-cooled CMOS camera (Hamamatsu C11440-22CU). One electromagnet generates the out-of-plane field $B_z = [0\text{ mT}, 60\text{ mT}]$, and two electromagnets generate the in-plane field $B_x = [0\text{ mT}, 160\text{ mT}]$. The larger in-plane field is obtained by connecting the electromagnets with soft-iron bars forming a C-frame configuration, which closes the field lines and thus increases the field between the poles. The field magnitude is measured with a Hall probe (MAGNET-PHYSIK HU-ST1-184605). The probe cannot be placed close to the sample because the gap between the objective and the sample is < 1 mm. Instead, the probe is placed a few centimeters away, and the measured field is multiplied by a calibrated factor. The automation of the setup, instruments, measurement procedure, and image processing is performed on a LabView program developed by Marvin Müller. The signal-to-noise ratio is improved using standard time and spatial averaging of the image. Then, the magnetic contrast is enhanced by taking differential MOKE images,

obtained by subtracting a reference image captured in a fully magnetized state from each image.

3.5 Computation of the magnetic domain wall velocity

In Chapter 5 and Chapter 6, we study the current-induced magnetic domain wall (DW) motion using the MOKE setup. We plot the variations of the DW velocity as a function of different parameters to extract the magnetic properties of the samples. To give an accurate estimate, it is often necessary to average the DW velocity several times per experimental parameter (about three to five images per data point) which can be time consuming. While the experiment is done manually, the analysis can be performed automatically. For this purpose, we developed a Matlab code to measure the DW displacement from the MOKE images and calculate the DW velocity. This code can be found in the Appendix 8.1.

Here we detail the image processing procedure. The code starts by asking the user to specify the location of the file containing the images. It then loads the file names and filters them to keep only the files with a specific prefix, which is useful for tracking which set of measurements is being analyzed. The code opens the first image in the filtered list and ask the user to select the region of interest that contains the racetrack. Subsequent images will then be cropped to these coordinates, focusing the analysis on the DW displacement.

The function "f-DW-Width-Auto" is responsible for calculating the DW displacements. It starts by importing the image and then crops it according to the specified region of interest, as shown in Figure 3.4(a)-(b). After that, the function creates a binary image by converting all pixels above a specified contrast threshold (defined by the user) to 1 and all pixels below the threshold to 0, which generates a matrix of ones and zeros. The function measures the domain wall length using two methods: the maximum displacement x_{DWmax} and the mean displacement x_{DWmean}.

To calculate the maximum displacement x_{DWmax}, the function sums the white pixels in each row, creating a histogram from the horizontal line of pixels. It then finds the k largest elements (usually k=3) and averages their values to calculate the maximum displacement x_{DWmax}, which is illustrated with the red dashed lines in Figure 3.4(c). On the other hand, to calculate the mean displacement x_{DWmean}, the function finds the start and end points of the displacement by reusing the values found for the maximum displacement. The start point is located by finding the first column containing ones in the row from the k largest values, while the end point

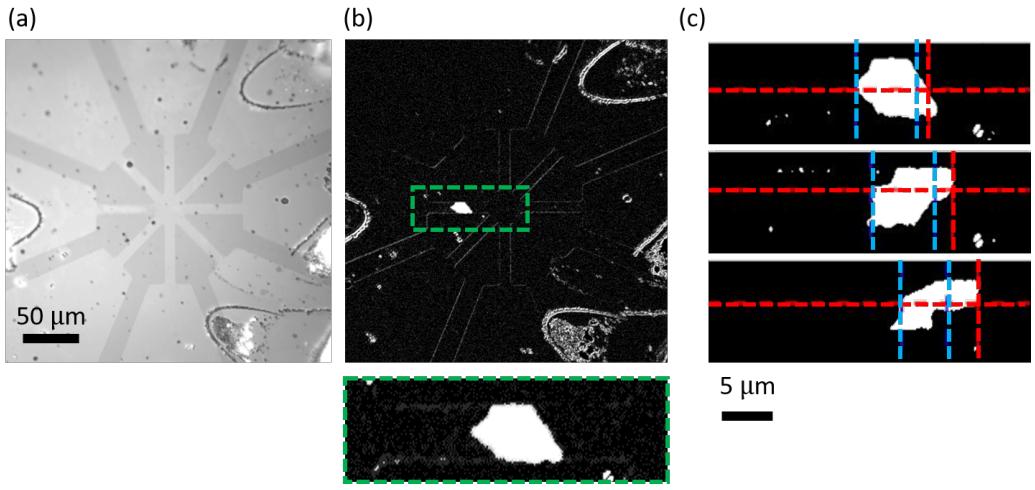

Figure 3.4: Example of image processing for calculating the DW velocity. The device is patterned 8 arms star with a width of $5 - \mu$m made of $Al_2O_3/Cr_2O_3(120\text{ nm})/Co(0.85\text{ nm})/Pt(2\text{ nm})$ sample (the device is studied in Chapter 5). (a) Optical image of the device. (b) MOKE images of a the domain wall displacements. The user is asked to select the region of interest that contains the racetrack (green rectangle). The zoom-in of the selected area is shown in the inset. (c) The image is processed to generate a binary image with only black and white pixels. Then, the maximum displacement is estimated (red dashed lines), and the mean displacement is estimated (blue dashed lines). The code then computes the velocities taking into account the number of pulses and the pulse length.

is found by adding x_{DWmax} to the start point coordinates. It then sums all pixels within that interval (from start to end) and divides by the height of the racetrack to calculate x_{DWmean}, which is illustrated with the blue dashed lines in Figure 3.4(c).

Eventually, two velocities v_{DWmax} and x_{DWmean} are calculated by dividing x_{DWmax} and x_{DWmean} by the total pulse duration, which is the product of the total number of pulses and the pulse length. The lengths in pixels are converted into meters using the scale $260 \cdot 10^{-6}\text{m}/2048$ pixels. The code extracts parameters of the experiment from the filenames, such as the number of pulses, the length and amplitude of the pulses, and the field strength. These parameters are used to compute the mean and standard deviation of velocities obtained from images with identical parameters.

It is worth noting that the function "f-DW-Width-Auto" may produce errors if some defects and dust appear as white pixels due to mechanical drift of the sample holder. These errors typically occur when the DW displacement is short and are difficult to distinguish from artifacts. To detect errors, each image is displayed to the user with the estimated displacements x_{DWmax} and x_{DWmean}, as shown in Figure 3.4(c). If errors are present, the user can use "f-DW-Width-Man" to manually select the starting and ending points that contain the DW displacement, thereby eliminating

artifacts from other parts of the racetrack. The code will then calculate x_{DWmax} as the length of this interval and x_{DWmean} using the same method as described in "f-DW-Width-Auto".

4

Systematic study of nonmagnetic resistance changes in antiferromagnetic / heavy metal devices

Summary

Intense current pulses are often required to operate microelectronic and spintronic devices. Notably, strong current pulses have been shown to induce magnetoresistance changes attributed to domain reorientation in antiferromagnet/heavy metal bilayers and non-centrosymmetric antiferromagnets. In such cases, nonmagnetic resistivity changes may dominate over signatures of antiferromagnetic switching. We report systematic measurements of the current-induced changes of the transverse and longitudinal resistance of Pt and Pt/NiO layers deposited on insulating substrates, namely Si/SiO_2, Si/Si_3N_4, and Al_2O_3. We identify the range of pulse amplitude and length that can be used without affecting the resistance and show that it increases with the device size and thermal diffusivity of the substrate. No significant difference is observed in the resistive response of Pt and NiO/Pt devices, thus precluding evidence on the switching of antiferromagnetic domains in NiO. The variation of the transverse resistance is associated to a thermally-activated process in Pt that decays following a double exponential law with characteristic timescales of a few minutes to hours. We use a Wheatstone bridge model to discriminate between positive and negative resistance changes, highlighting competing annealing and electromigration effects. Depending on the training of the devices, the transverse resistance can either increase or decrease between current pulses. Further, we elucidate the origin of the nonmonotonic resistance baseline, which we attribute to training effects combined with the asymmetric distribution of the current. These results provide insight into the origin of current-induced resistance changes in metal layers and a guide to minimize nonmagnetic artifacts in switching experiments of antiferromagnets.

This chapter is based on the publication "Systematic study of nonmagnetic resistance changes due to electrical pulsing in single metal layers and metal/antiferromagnet bilayers" (Ref. [122]). Dr. Charles-Henri Lambert conceived and designed the initial experimental setup. Dr. Giacomo Sala and I co-developed the software interface and implemented the relay matrix for automated measurements. I performed the measurements, the data analysis and simulation. Dr. Giacomo Sala, Dr. Can Avci, Dr. Saul Vélez, Dr. Charles-Henri Lambert, Prof. Pietro Gambardella and I interpreted the results and co-wrote the manuscript.

4.1 Introduction

The compensated magnetic lattice and the strong exchange coupling between antiparallel magnetic moments make antiferromagnets (AFMs) appealing for data storage applications [7, 21]. The absence of a net magnetization limits the cross-talk between devices in densely-packed layouts and minimizes the influence of external magnetic fields on the magnetic order parameter. Moreover, the dynamic resonant modes associated with the staggered antiferromagnetic structure are orders of magnitude higher in frequency compared to ferromagnets [9, 123], thus opening unique prospects for terahertz spintronics [6, 8]. For a long time, however, controlling the orientation of the magnetic moments in AFMs by means of scalable and integration-friendly methods was deemed to be impossible. Recent experiments provide a solution to this problem, as it was shown that current injection in noncentrosymmetric metallic AFMs [124, 125, 126, 8, 127, 128, 129, 130, 131, 132, 133] as well as in heavy metal layers deposited on insulating AFMs [12, 134, 13, 15, 135, 136] lead to the in-plane rotation of the Néel vector due to the current-induced spin-orbit torques [56]. Reading of the Néel vector reorientation in metallic AFMs and AFM/heavy metal bilayers can then be performed by measuring the anisotropic magnetoresistance of the AFM and spin Hall magnetoresistance of the heavy metal, respectively. Together, these effects allow for all-electrical manipulation and detection of antiferromagnetic order.

The electrical switching of AFMs requires a sufficient torque to reorient the magnetic moments, which in turn requires a high current density. In addition to the torque, Joule heating plays a critical role in the switching by assisting the magnetic moments in overcoming the magnetic anisotropy energy barrier between two different easy axis orientations [127, 17]. Intense currents, however, can also produce irreversible changes of the materials due to thermal annealing [137] and electromigration [138]. Although the switching of the Néel vector in AFM/heavy metal bilayers such as

NiO/Pt has been confirmed by imaging techniques, including x-ray photoemission electron microscopy [12, 13], birefringence [86] and spin Seebeck microscopy [15], transport measurements on single-layer Nb and Pt thin films have shown nonmagnetic resistive signatures very similar to the ones attributed to magnetoresistance changes [139, 140, 141]. Analogous resistive signatures in AFM/Pt bilayers are considered as a proof of current-induced switching in an increasing variety of AFMs, such as hematite [135, 136], Mn_2Au [142], PtMn [143], MnN [131], Mn_3Sn [133] and synthetic antiferromagnets [144]. Given the multiple factors that influence the resistivity of these bilayers, it is important to investigate the pulsing conditions and device characteristics that lead to the appearance of nonmagnetic resistance changes in metallic systems, containing AFMs or not.

In this study, we perform a systematic characterization of the current-induced resistance changes in Pt and NiO/Pt cross-shaped devices deposited on different substrates. We report measurements of the transverse and longitudinal resistance as a function of the amplitude and length of the current pulses, device size, and training history. In agreement with the nonmagnetic resistive effects revealed by previous studies [139, 140, 141], we show that both gradual and step-like resistance changes can be induced in Pt depending on the training of the devices and independently of the presence of NiO. Therefore, the resistance variations in NiO/Pt cannot be considered as signatures of domain switching in NiO. Using a simple Wheatstone bridge model, we identify competing effects that either decrease or increase the local resistivity, which we attribute to current-induced annealing and electromigration, respectively. Moreover, we show that the resistance changes depend strongly on the pulse length and training history of the devices as well as on the device size, which results in a broad variety of resistive signals.

This paper is organized as follows: Section 4.2 describes the pulsing and read-out schemes commonly employed in AFM devices and in this work. Sections 4.3 and 4.4 introduce the Wheatstone bridge model used to interpret the nonmagnetic resistance changes and the experimental systems, respectively. Sections 4.5 and 4.6 present the behavior of the transverse resistance upon application of pulses of increasing amplitude and the relaxation process after excitation. Sections 4.7 and 4.8 report the device response as a function of the pulse length and the substrate thermal diffusivity. Section 4.9 and 4.10 focus on the influence of the device size in the presence of artifacts and how asymmetric responses between two pulsing directions affect the behavior of the transverse resistance.

4.2 Electrical writing and reading scheme of antiferromagnets

In metallic AFMs with non-centrosymmetric crystal structure, switching is usually ascribed to the inverse spin galvanic effect [145]. Owing to spin-orbit coupling and the lack of inversion symmetry, an electric current flowing in these AFMs generates a non-equilibrium spin polarization of opposite sign on each magnetic sublattice. The resulting staggered torque tends to align the Néel vector perpendicular to the current. Reversible switching can be achieved by pulsing along two orthogonal directions, thus inducing a rotation of $\pm 90^{\circ}$ of the Néel vector. This manipulation of the magnetic orientation can then be electrically detected via a transverse magnetoresistance measurement [124]. The inverse spin galvanic effect was initially predicted for Mn_2Au [145] and experimentally confirmed in CuMnAs [124, 125, 8, 132], Mn_2Au [126, 127, 128, 129], and in magnetically intercalated transition metal dichalcogenides [130].

In insulating AFMs, the switching process relies on the spin-current transferred from an adjacent metallic layer with strong spin-orbit coupling. The latter scheme is similar to spin-orbit torque switching demonstrated for metallic ferromagnet [146] and insulating ferrimagnets [147, 56]. Several mechanisms have been proposed in order to explain the perpendicular switching of AFMs due to a non-staggered spin torque. In NiO(001)/Pt bilayers, it was suggested that the damping-like spin-orbit torque originating from the current-induced spin accumulation at the Pt interface induces coherent switching of antiferromagnetic domains by orienting the Néel vector towards the writing current [134]. Alternatively, the field-like spin-orbit torque acting on the uncompensated interfacial spins of NiO could drive a coherent rotation of the spins perpendicular to the writing current in Pt/NiO(111)/Pt trilayers [12]. Finally, mechanisms based on the action of the spin current on antiferromagnetic domain walls have been suggested in NiO/Pt [148, 13, 15]. A spin current would directly act on the magnetic moments in the domain walls, driving walls with opposite chirality in opposite directions [149]. As this process does not discriminate between the expansion or contraction of domains, an additional degeneracy-breaking mechanism is required in order to achieve net switching. The latter is provided by a translational ponderomotive force due to the damping-like torque, which favors the expansion of domains with Néel vector parallel to the current [13]. Recently, an additional current-induced mechanism that does not involve SOT switching was proposed for a hematite/Pt bilayer deposited on Al_2O_3 [135] as well as for NiO/Pt deposited on MgO [81], wherein the current-induced Joule heating produces thermal expansion

of the substrate and results in mechanical stress that couples to the magnetic order of the AFM through its high magnetostrictive coefficient.

All these switching mechanisms are based on a deterministic writing scheme that aligns the Néel vector either parallel or perpendicular to the writing current, depending on the driving torque being damping-like or field-like, respectively, or magnetostriction. Following one or more writing pulses, an electrical read-out is performed by measuring the variation of the transverse resistance. In metallic AFMs the read-out signal is the transverse component of the anisotropic magnetoresistance — also called the planar Hall effect — which is sensitive to the in-plane orientation of the Néel vector relative to the current [150, 124]. In insulating AFMs adjacent to a heavy metal, the signal relates to the transverse component of the spin-Hall magnetoresistance, which is also sensitive to the in-plane orientation of the spins relative to the current direction [151, 152, 19, 153]. The anisotropic magnetoresistance and spin-Hall magnetoresistance have the common property of being quadratic in the magnetization, which means that they are invariant upon 180° reversal of the Néel vector. Both effects are extremal when the Néel vector sets at $+45°$ ($-45°$) or, equivalently, at $-135°$ ($+135°$) to the sensing current.

To summarize, the writing process described above accounts for 90° switching of the domains either towards or perpendicular to the writing current, and the read-out signal amplitude is maximal when the sensing current flows at an angle of $\pm 45°$ from the writing line. Hence, the common device geometry is a Hall cross with either 4 or 8 symmetrical arms. In the 4 arms geometry, the set writing pulse, henceforth called P1, is applied along one diagonal of the cross, whereas the reset writing pulse, henceforth called P2, is applied along the other diagonal and orthogonal to P1. During read-out, a small sense current is injected between two opposite arms of the cross and the transverse resistance is measured by probing the Hall voltage between the two arms perpendicular to the sensing current, as illustrated in Figure 4.1(a). In this work, we consider only the 4 arms geometry, even though similar results are obtained on 8-arms crosses.

4.3 Wheatstone bridge model of a Hall cross

According to the considerations presented above, the change of transverse voltage, ΔV_{xy}, due to the switching of antiferromagnetic domains should have opposite sign following the writing pulses P1 and P2. Furthermore, if the switching volume is reversible, the signal should be symmetric in amplitude for P1 and P2 pulses.

As shown in this study, however, similar transverse voltage variations to the ones expected for the signature of AFM switching can be observed in Hall crosses due to purely nonmagnetic effects. In order to understand the effects of the pulses onto a nonmagnetic resistive device, it is convenient to model the Hall cross as a Wheatstone bridge. We consider a division of the Hall cross into four quadrants of equal size and corresponding resistances R_1, R_2, R_3 and R_4, as depicted in Fig. 4.1(a). During the pulsing, the current density is higher around the corners due to the current crowding effect[154]. The intense heat generated by the current can affect the metallic structure, which in return would change the resistance of the quadrants: P1 would modify mostly R_1 and R_4 whereas P2 would modify mostly R_2 and R_3. As the sensing current is deflected proportionally to the local resistance, a net voltage arises at the junction of the quadrants, as expected for an unbalanced Wheatstone bridge. For the sensing configuration illustrated in the rightmost panel of Fig. 4.1(a), the transverse voltage is $V_{xy} = (R_1/(R_1 + R_2) - R_3/(R_3 + R_4)) \cdot V_s$, where V_s is the voltage applied by the sensing current source. The resistances of the arms can be discarded in this model as the arms through which the sensing current flows do not influence the transverse voltage and there is no current passing through the voltage arms.

The Wheatstone bridge model highlights two important characteristics of the measurement scheme of AFMs in cross-shape devices. Firstly, $V_{xy} = 0$ when $R_1 \cdot R_4 = R_2 \cdot R_3$. Secondly and most importantly, the change of transverse voltage consecutive to a pulse, ΔV_{xy}, caused by the variation of R_1 and R_4 has opposite sign than the one caused by the variation of R_2 and R_3. Specifically, ΔV_{xy} is negative for a decrease of R_1 or R_4, but positive for a decrease of R_2 or R_3. Moreover, ΔV_{xy} is positive for a increase of R_1 or R_4, but negative for a increase of R_2 or R_3. This is a crucial point as it shows that a negative ΔV_{xy} after P1 means that the resistance at the corners has decreased relative to the unpulsed state, whereas a positive ΔV_{xy} after P1 means that the resistance has increased. Thus the sign of ΔV_{xy} allows for discriminating current-induced annealing effects, which tend to reduce the resistance of metal layers, from temporary thermoresistive effects and permanent electromigration effects, which tend to increase the resistance.

4.4 Device fabrication and experimental setup

We focus on two different sets of samples: a series of Pt(5 nm) reference layers and a series of NiO(10 nm)/Pt(5 nm) bilayers deposited on three different substrates. The numbers between brackets indicate the thickness of each layer. NiO was grown

at 550 °C, followed by Pt deposition at room temperature after cooling down under vacuum. These layers were sputter-deposited on three different substrates, Si/SiO_2(500 nm), Si/Si_3N_4(400 nm) and sapphire (Al_2O_3), at the same time in order to minimize thickness variations. In these conditions, we obtain a typical roughness of less than 1 nm; all layers are preferentially oriented along the (111)-growth direction. X-ray diffraction measurements indicate a high crystalline epitaxial quality of the NiO layers grown on Al_2O_3, whereas no diffraction peaks are observed for NiO deposited on Si/SiO_2(500 nm) and Si/Si_3N_4(400 nm) for such thickness. A separate batch deposited on Al_2O_3 including a Fe layer on top of NiO confirmed the presence of antiferromagnetic order by means of a reversible exchange bias upon cooling in opposite magnetic fields. All layers were subsequently patterned using reactive ion etching in single and double Hall crosses of different width, from 2.5 μm to 12.5 μm in steps of 0.5 μm. The resistivity of each sample was measured with 4 points probes in double Hall crosses, giving $\rho_{\text{SiO/Pt}} = 3.20 \cdot 10^{-7}\ \Omega\,\text{m}$, $\rho_{\text{SiO/NiO/Pt}} = 3.30 \cdot 10^{-7}\ \Omega\,\text{m}$, $\rho_{\text{SiN/Pt}} = 3.12 \cdot 10^{-7}\ \Omega\,\text{m}$, $\rho_{\text{SiN/NiO/Pt}} = 3.20 \cdot 10^{-7}\ \Omega\,\text{m}$, $\rho_{Al_2O_3/Pt} = 2.38 \cdot 10^{-7}\ \Omega\,\text{m}$, $\rho_{Al_2O_3/NiO/Pt} = 2.17 \cdot 10^{-7}\ \Omega\,\text{m}$. Although the NiO layer does not significantly affect the Pt resistivity, the high crystalline quality of the NiO and Pt films deposited on Al_2O_3 leads to a lower resistivity than the Si-based substrates. These resistivities are comparable to those obtained for Pt using similar fabrication methods and deposition conditions [155, 156, 157].

The writing pulses were provided by a voltage source that generates rectangular pulses of variable width (50 ns - 1 ms) and amplitude (2 V - 40 V). For instance, a pulse of 10 V corresponds to a current density along the diagonal $j_w = V/(R_p\, t\, \sqrt{2} w) = 0.71 \cdot 10^{12}$ A/m^2, where V is the pulse amplitude, $R_p = 200\,\Omega$ is the pulse path resistance measured at the output terminals (typical value), $t = 5$ nm is the film thickness and $\sqrt{2}w = \sqrt{2} \cdot 10$ μm is the diagonal of the cross. For reading the transverse voltage, a current source provided an alternating current with peak-to-peak amplitude of 0.5 mA at a frequency of 10 Hz, corresponding to a current density in the sensing arms of 10^{10} A/m^2 in the same device. The alternating current substantially lowers the noise limit using a pseudo-lock-in detection scheme. The transverse voltage was measured 2 s after pulsing to allow the device to cool down using an integration time of 0.5 s. A relay matrix alternates between the writing (P1 and P2) and the reading configurations. Those relays are essential to control the current path in the device by setting which arms are under tension, floating, or grounded.

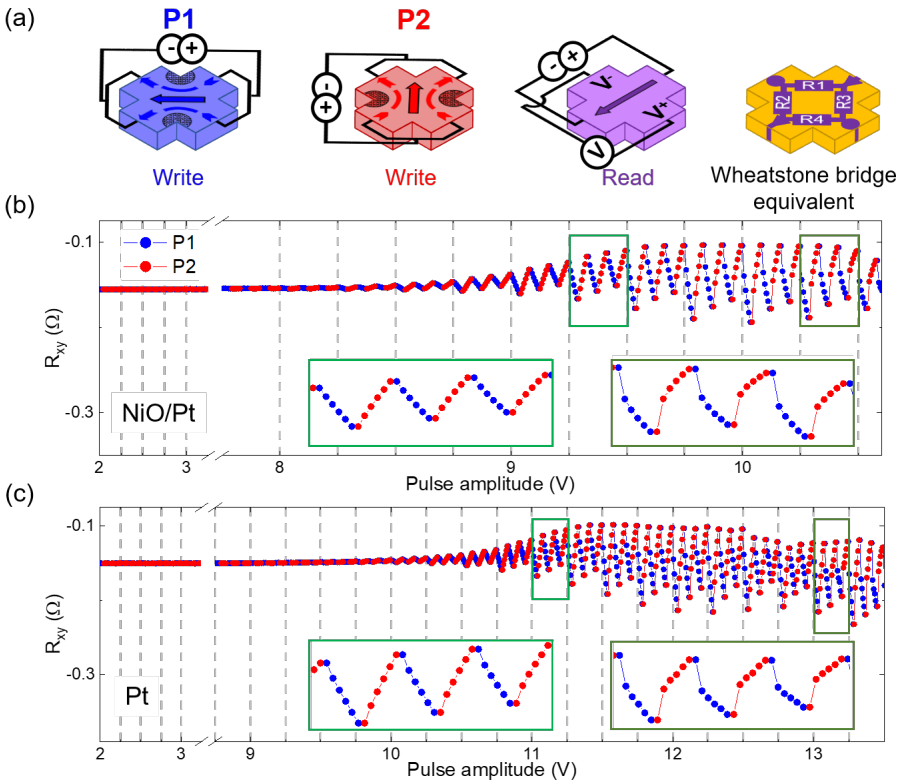

Figure 4.1: (a) Illustrative diagrams of the pulsing and reading schemes and Wheatstone bridge model of a Hall cross with the corresponding resistances R_1, R_2, R_3 and R_4. (b) R_{xy} as a function of writing pulse amplitude measured in Al_2O_3/NiO/Pt and (c) Al_2O_3/Pt 10 μm-wide Hall crosses. The pulse amplitude is increased in steps of 0.25 V in correspondence of the gray dashed lines. For each step, a sequence of 3 repeats, made of 5 consecutive P1 pulses and 5 consecutive P2 pulses of length $\tau = 1$ ms is applied. The transverse resistance measured after each pulse is plotted as a blue or red dot for P1 and P2 pulses, respectively. The insets show the saw tooth (left) and step-like (right) resistance changes.

4.5 Transverse resistance as a function of pulse amplitude

In most of the reported current-induced switching experiments, the antiferromagnetic materials were epitaxial films. We thus first characterize the response of the epitaxial samples Al_2O_3/NiO/Pt and Al_2O_3/Pt. Following the pulse-sense scheme described in Sect. 4.2, Fig. 4.1(b)-(c) illustrates the typical variation of the transverse resistance of Al_2O_3/NiO/Pt and Al_2O_3/Pt 10 μm-wide single Hall crosses following the application of orthogonal pulses P1 and P2. The pulse amplitude is gradually increased in steps of 0.25 V. For each step, a sequence of 3 repeats, each made of 5 consecutive P1 pulses followed by 5 consecutive P2 pulses of length $\tau = 1$ ms, is

implemented (delimited by the dashed lines). The transverse resistance measured after each pulse is plotted as a blue or red dot for P1 and P2 pulses, respectively. We observe a consecutive decrease and increase of the transverse resistance following P1 and P2 pulses, respectively. The resistance variation increases with the pulse amplitude in both the magnetic and nonmagnetic samples. A change of resistance of $\Delta R_{xy} = 0.05\ \Omega$ is measured for a pulse amplitude of 9.25 V in Al_2O_3/NiO/Pt and 11 V in Al_2O_3/Pt, corresponding to a current density j_w along the diagonal of $0.75 \cdot 10^{12}$ A/m^2 and $0.76 \cdot 10^{12}$ A/m^2, respectively.

The shape of the signal evolves as the devices undergo several repeats. At first, R_{xy} has a saw-tooth shape as the resistance changes gradually after each of the 5 consecutive pulses along P1 and P2. At larger voltage, the resistance changes in a step-like manner, where the effect of the first pulse is comparably much larger than the 4 successive pulses [see insets in Fig. 4.1(b)-(c)]. The saw-tooth shape has been previously associated with resistive changes of the nonmagnetic layer, whereas the step-like shape has been considered as a signature of AFM switching [134, 12, 13, 86]. This distinction is not supported by the data presented in Fig. 4.1, in agreement with recent works on magnetic and nonmagnetic samples [139, 140, 141]. We also observe a stabilization of the amplitude of the resistance changes after 5 consecutive pulses with increasing pulse amplitude, which we assign to a training effect. As the behavior of the Al_2O_3/NiO/Pt and Al_2O_3/Pt samples is both qualitatively and quantitatively similar, we attribute the variations of R_{xy} to pulse-induced changes of the Pt resistivity.

The variation of R_{xy} is attributed to the higher current density passing along the corners of the Hall cross [shaded areas in Fig. 4.1(a)]. According to the Wheatstone bridge model described in Sect.4.3, the negative and positive ΔR_{xy} after pulsing along P1 and P2, respectively, correspond to a decrease of the local resistivity. These observations indicate that the temperature rise during the pulse anneals the metal layer, which decreases its resistivity after the cooling of the device. As the pulse amplitude increases, the annealing process becomes less effective and ΔR_{xy} tends to saturate. This conclusion is corroborated by the work of T. Wagner *et al.* [140], in which Nb thin films deposited at room-temperature on an MgO substrate showed a similar decrease of the resistivity along the pulsed-corners of the device. Furthermore, this behavior agrees with previous studies of the resistivity of Pt films, which show an initial decrease followed by an increase of the Pt resistivity as a function of annealing temperature owing to thermally-induced redistribution of structural imperfections [158, 157]. Finally, measurements performed on the SiO_2/NiO/Pt, SiO_2/Pt, Si_3N_4/NiO/Pt and Si_3N_4/Pt all show a similar behavior with no systematic differences between them that could evidence a magnetic signal.

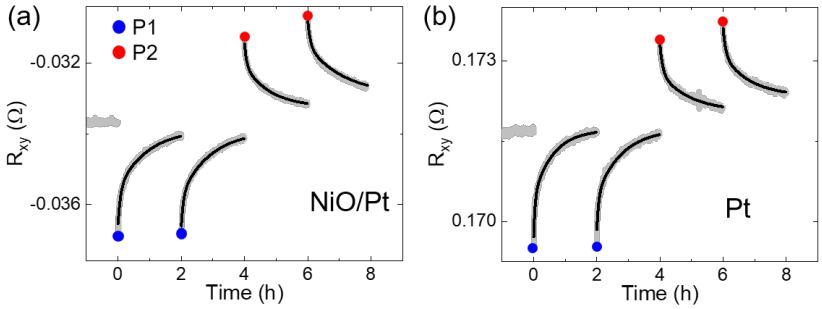

Figure 4.2: Relaxation of the transverse resistance following single pulses P1 (blue dots) and P2 (red dots) for Al_2O_3/NiO/Pt (a) and Al_2O_3/Pt (b) in 10-μm-wide Hall crosses. The timing of each pulse is indicated by a vertical dashed line. The solid black lines are fits with a double exponential function (see text for details).

In the literature, the nonmagnetic variation of R_{xy} in AFM/Pt bilayers has been assigned to two other effects. One is the temporary increase of the local resistivity due to Joule heating that persists during the sensing [141]. The other is electromigration occurring at the corners of the Hall cross, which causes the formation of hillocks and metal voids that increase the local resistivity [141, 140]. Both these effects would result in ΔR_{xy} of opposite sign with respect to our measurements. Concerning the first effect, the waiting time between the writing and reading events is about 2 s, which is long enough for the device to thermalize to the substrate temperature [120, 121]. As for electromigration, we cannot exclude that it coexists with thermal annealing. Likely, however, electromigration dominates at voltages higher than 20 V in our 10 μm-wide Hall crosses ($j_w > 1.7 \cdot 10^{12}$ A/m^2), as we also observe an increase of the resistance preceding the device breakdown at high current density (see Sect. 4.9). Other models have linked ΔR_{xy} to a Seebeck voltage along the direction of the current-induced temperature gradient in Pt [139]. Accordingly, if the Seebeck voltage is at the origin of the change of the transverse resistance, the measured voltage should be independent of the sensing current. Contrary to this hypothesis, we find a linear relationship between ΔV_{xy} and the sensing current between 0.1 mA and 10 mA, which confirms the resistive origin of ΔR_{xy}.

4.6 Temporal relaxation of the transverse resistance after pulsing

After pulsing, R_{xy} relaxes towards the pre-pulse value on a time scale of hours. Figure 4.2 illustrates the typical evolution of R_{xy} over 2 h following single pulses

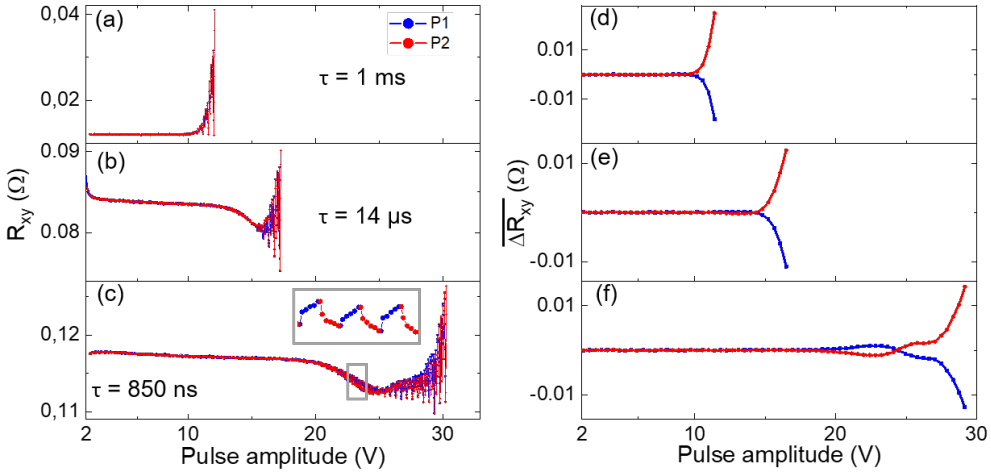

Figure 4.3: (a)-(c) R_{xy} as a function of writing pulse amplitude measured in a Al_2O_3/Pt 10 μm-wide Hall cross for pulses of length (a) 1 ms, (b) 14 μs, and (c) 850 ns. The pulse amplitude is increased in steps of 0.25 V. For each step, a sequence of 3 repeats of 5 consecutive P1 pulses and 5 consecutive P2 pulses is applied, as in Fig. 4.1(b)-(c). (d)-(f) $\overline{\Delta R_{xy}}$ is the average change of resistance after 5 pulses calculated over 3 repeats at constant pulse amplitude from the traces in (a)-(c). The pulsing ramps were stopped when $\overline{\Delta R_{xy}} \geq 0.01\ \Omega$. The inset shows R_{xy} trace with inverted sign change.

P1 (blue) and P2 (red) in Al_2O_3/NiO/Pt and Al_2O_3/Pt. The timing of the single pulses is denoted by the dashed lines. As a reference, R_{xy} of the pristine device is recorded starting 1 h before the first pulse P1 to demonstrate the absence of drift in the measurements. The relaxation, which we observe in nonmagnetic and magnetic samples alike, is characterized by different short and long time scales that cannot be captured by a simple exponential fit. To fit the data, we thus use a double exponential function $R_{xy}(t) = y_0 + A_1 \cdot exp(-(t-t_0)/\lambda_1) + A_2 \cdot exp(-(t-t_0)/\lambda_2)$, where $t_0 = 2$ s is the time interval between the pulse and the sense current, $A_{1,2}$ are amplitude parameters, and $\lambda_{1,2}$ are the relaxation times. Such double exponential decay is typical of relaxation processes in metallic glasses, where the fast process is local and reversible and the slow one involves large scale irreversible structural rearrangements due to the subdiffusive motion of atoms [159, 160].

The fits of P1 and P2 curves (black lines in Fig. 4.2) give a short decay time $\lambda_1 = 4 \pm 0.6$ min and 4.2 ± 0.2 min for Al_2O_3/NiO/Pt and Al_2O_3/Pt, respectively, and a long decay time $\lambda_2 = 48 \pm 5$ min and 56 ± 3 min. These short and long decay times are of the same order of magnitude in the six different samples considered in this study. Also, we find that the fit coefficients do not depend significantly on the substrate or the presence of the NiO layer. A similar relaxation process was observed in MgO/Pt, Si/Pt and glass/Pt[139], but was attributed to slow cooling through

the substrate and a long lasting transverse voltage due to the Seebeck effect across the device. This interpretation, however, requires the amplitude of the transverse voltage to be independent of the sensing current, which is not compatible with the linear relation between the transverse voltage and the sensing current found in our measurements (see Section 4.5). Other studies of Pt and NiO/Pt have related the long lasting relaxation of R_{xy} to the diffusional creep induced by electromigration with the Pt grain boundaries acting as sources and sinks for point defects [141].

We further note that the long lasting relaxation process is not observed in the consecutive pulse-sense-pulse measurements reported in Fig. 4.1(b)-(c) as the time interval between these steps is too short (about 2 s). However, in such consecutive measurements, the relaxation manifests itself as a drift of the resistance baseline. Moreover, the relaxation can induce a sign inversion of ΔR_{xy} in consecutive pulse-sense-pulse measurements, which we discuss in the following section.

4.7 Transverse resistance as a function of pulse amplitude and pulse length

In this section, we analyze the response of the devices when the length of the writing pulses is reduced from 1 ms to below 1 μs. Following the same procedure described in Sect. 4.5, Fig. 4.3(a)-(c) shows the change of R_{xy} in a Al_2O_3/Pt 10 μm-wide Hall cross as a function of pulse amplitude for pulse lengths of 1 ms, 14 μs, and 850 ns. In order to avoid extensive training and break down of the devices during the measurements, the pulse amplitude is increased in steps of 0.25 V until $\overline{\Delta R_{xy}} \geq 0.01\ \Omega$, where $\overline{\Delta R_{xy}}$ is the arithmetic mean of the change of resistance after 5 pulses over the 3 repeats that are recorded at the same pulse amplitude. Figure 4.3(d)-(f) reports $\overline{\Delta R_{xy}}$ calculated from the traces in Fig. 4.3(a)-(c). We observe that the minimum pulse amplitude required to obtain a noticeable $\overline{\Delta R_{xy}} \geq 0.001\ \Omega$ increases systematically for shorter pulses: 10.5 V, 11 V, and 20 V for a pulse length of 1 ms, 14 μs, and 850 ns, respectively. This highly nonlinear relation between the pulse amplitude and pulse length suggests an interplay between the current-induced Joule heating of the device and heat dissipation through the substrate. Such behavior is expected if $\overline{\Delta R_{xy}}$ is due to current-induced annealing, as the probability of thermally activated processes depends linearly on time and exponentially on the inverse of the temperature.

The curves shown in Fig. 4.3 evidence also a variation of the baseline of R_{xy}, which changes from straight in (a) to nonmonotonic in (b) and (c). This effect is ascribed

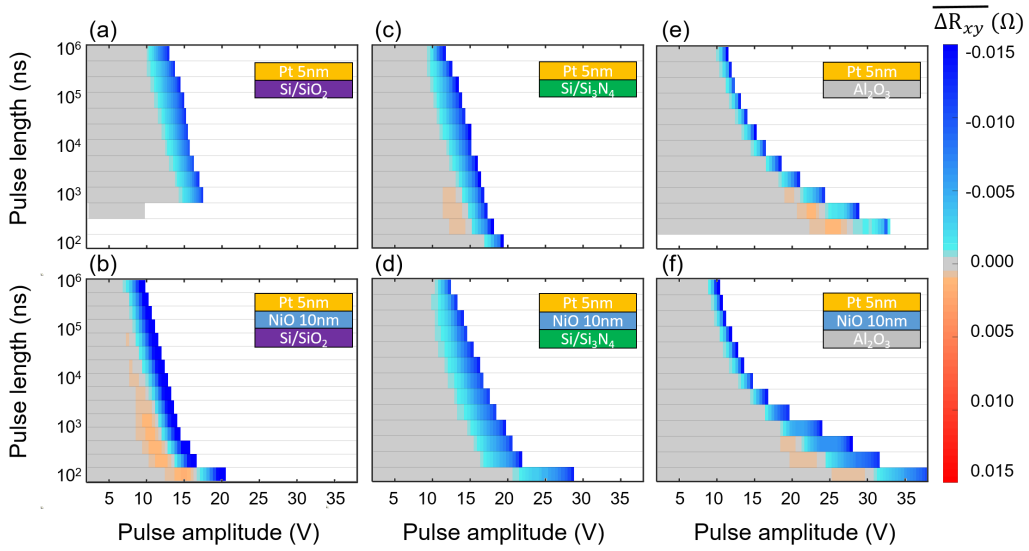

Figure 4.4: Comparison of the average transverse resistance change as a function of pulse amplitude and pulse length in a 10-μm-wide Hall cross of (a) SiO_2/Pt, (b) SiO_2/NiO/Pt, (c) Si_3N_4/Pt, (d) Si_3N_4/NiO/Pt, (e) Al_2O_3/Pt and (f) Al_2O_3/NiO/Pt. The plots show $\overline{\Delta R_{xy}}$ measured after 5 consecutive P1 pulses and averaged over 3 repeats at constant pulse amplitude, following the same measurement scheme reported in Fig.4.3. For each pulse length, a ramp of increasing pulse amplitude is applied until $\overline{\Delta R_{xy}} \geq 0.01\Omega$. The color scale represents the amplitude and sign of $\overline{\Delta R_{xy}}$. Grey-shaded areas indicate no resistance change.

to the training of the device. In a pristine device, as the voltage is ramped up for the first time, R_{xy} decreases after P1 pulses and comes back to its previous value after an equal number of P2 pulses, as shown in Fig. 4.3(a). As the ramp in Fig. 4.3(a) ends with 5 pulses along P2, R_{xy} is large and tends to relax at the beginning of the second ramp, shown in Fig. 4.3(b). Depending on the length, spacing, and amplitude of the pulses, the interplay of excitation and relaxation effects results in a changing baseline of R_{xy}, as discussed in more detail in Sect. 4.10.

Measurements performed with shorter pulses evidence another remarkable effect, namely the inversion of the sign of ΔR_{xy} preceding the onset of the larger variations of ΔR_{xy}, which can be observed in the inset of Fig. 4.3(c). The sign inversion becomes more clear when plotting $\overline{\Delta R_{xy}}$, namely the average excursion of the trace as a function of the pulse amplitude. At high voltage, $\overline{\Delta R_{xy}}$ is consistent with a decrease of R_{xy} induced by pulsing, as described in Sect. 4.5. At intermediate amplitude, however, the sign of $\overline{\Delta R_{xy}}$ is inverted, as seen by the difference of the blue and red curves in Fig. 4.3(f) and in the inset of Fig. 4.3(c). The sign inversion

typically appears when multiple pulses are applied to Pt and NiO/Pt devices and when the training state is more advanced.

We assign this transient sign inversion to heat-assisted relaxation induced by a current pulse, which can dominate over annealing in trained devices. During the first ramp, each pair of the device quadrants, $R_{1,4}$ and $R_{2,3}$ (see Sect. 4.3), undergoes the same annealing effect and ΔR_{xy} for P1 (P2) is successively negative (positive). Then, in the small amplitude regime at the beginning of the following ramps, the four quadrants uniformly relax and give $\Delta R_{xy} \approx 0$. Upon increasing the pulse amplitude, the temperature of the quadrants gradually rises, which speeds up the relaxation of these quadrants compared to the unpulsed quadrants. This asymmetric change of resistance induces a positive (negative) ΔR_{xy} after P1 (P2) pulses. This transient state takes place only in a small range of pulse amplitudes, namely when the current supplies enough heat to accelerate the relaxation rate without initiating the annealing process. The amplitude of this effect depends on the training history of the sample and changes from device to device.

4.8 Influence of the antiferromagnetic layer and substrate

In order to investigate the influence of the NiO layer and of the substrate on the transverse resistance, we compare the average $\overline{\Delta R_{xy}}$ as a function of the pulse amplitude and pulse length for Pt and NiO/Pt deposited on Si/SiO_2, Si/Si_3N_4 and Al_2O_3, as shown in Fig. 4.4(a)-(f). In these plots, the colors represent the amplitude of $\overline{\Delta R_{xy}}$ measured after P1 pulses and the grey areas represent the range where $\overline{\Delta R_{xy}} \approx 0$. No measurements were acquired in the white areas because the change of resistance exceeded the limit $\overline{\Delta R_{xy}} \geq 0.01\ \Omega$. The measurements of $\overline{\Delta R_{xy}}$ recorded after P2 pulses are roughly symmetric and opposite in sign to P1, corresponding to complementary color maps with inverted blue and red colors.

We find that the presence of NiO makes very little difference in the response of the devices. Neither the NiO/Pt sample with high epitaxial quality grown on Al_2O_3 nor those grown on SiO_2 and Si_3N_4 show significant differences with respect to the single Pt layers, confirming that the resistance variation in such structures originates from Pt rather than from switching of the AFM.

In all devices, the pulse amplitude required to attain a given variation of R_{xy} increases as the pulse length is reduced. However, the rate at which $\overline{\Delta R_{xy}}$ rises as a

function of pulse amplitude and pulse length is closely related to the substrate. In order to maintain the same $\overline{\Delta R_{xy}}$ amplitude when reducing the pulse length by a factor 1000, the pulse amplitude needs to be increased by a factor 2 for the samples grown on SiO_2 and Si_3N_4 and by a factor of 3 for the samples grown on Al_2O_3. This observation can be rationalized in terms of the thermal diffusivity $\mu_s = \kappa_s/(\rho_s\, c_s)$ of the substrate, which exemplifies how well a material conducts heat in terms of the thermal conductivity κ_s relative to its volumetric capacity for storing thermal energy, as given by the product of the density ρ_s and specific heat c_s. At room-temperature, the thermal diffusivity calculated from thin film parameters is $\mu_{SiO2} \approx 0.8$ mm^2 s^{-1} for SiO_2 ($\kappa = 1.3$ W m^{-1} K^{-1}, $\rho = 2200$ kg m^{-3}, $c = 730$ J kg^{-1} K^{-1}), $\mu_{Si3N4} \approx 0.9$ mm^2 s^{-1} for Si_3N_4 ($\kappa = 1.4$ W m^{-1} K^{-1}, $\rho = 2100$ kg m^{-3}, $c = 730$ J kg^{-1} K^{-1} [120, 161]), and from bulk parameters $\mu_{Al2O3} \approx 28$ mm^2 s^{-1} for Al_2O_3 ($\kappa = 46.06$ W m^{-1} K^{-1}, $\rho = 3980$ kg m^{-3}, $c = 418$ J kg^{-1} K^{-1} [162]). The gray shaded areas in Fig. 4.4 show that the substrates with high thermal diffusivity allow for using a larger range of pulse amplitudes and pulse lengths without inducing changes of R_{xy}. This finding is explained by the fact that substrates with a large thermal diffusivity can transfer heat fast without heating up too much compared to substrates with a low thermal diffusivity.

As a corollary, we note that the heat effectively dissipated in Pt depends on the balance between electrical power supplied to the system, heat transfer by conduction through the NiO and the substrate, and convection and radiation at the top of the devices. However, the convective and radiation heat losses are much smaller than the conduction heat transfer [163] and roughly equal for all the devices investigated in this study. Therefore, we conclude that the thermal diffusivity of the substrate is the main parameter affecting the heat accumulation in Pt induced by a given current in devices of equal size.

The temperature increase attained during the pulse is related to the electrical energy dissipated in the device, $E = \tau V^2/R_p$, where τ is the pulse length, R_p the resistance of the pulse path, and V the applied voltage. Figure 4.5 plots the energy required to induce a relative change $\overline{\Delta R_{xy}}/R_{xx} \geq 10^{-5}$ as a function of pulse length. The curves confirm that samples grown on SiO_2 and Si_3N_4 substrates require less energy compared to Al_2O_3 in order to attain a similar change in resistance. Moreover, when comparing the Al_2O_3 and Si-based substrates, the curves follow the same trend for long pulses but diverge for short pulses, showing that the samples grown on Al_2O_3 dissipate heat more efficiently for shorter pulses compared to longer pulses. We attribute this trend to the timescale required to transfer heat from the device to the substrate. For short pulses, $\tau \leq 10$ μs, the temperature rises sharply in the device but not in the substrate. For longer pulses, on the other hand, the heat dissipated

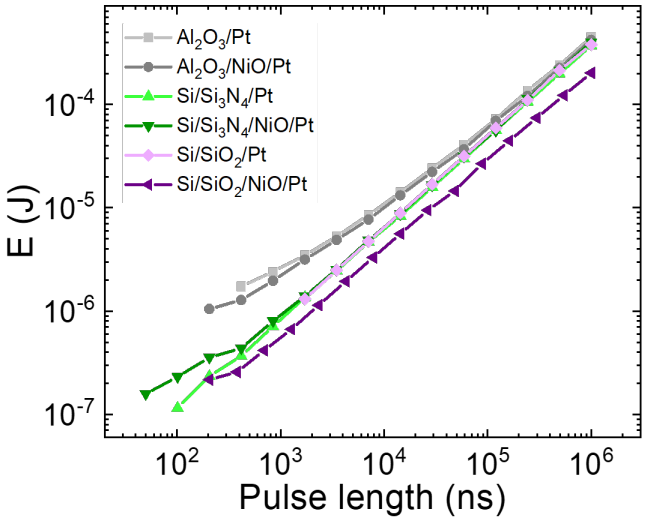

Figure 4.5: Electrical energy $E = \tau V^2/R_p$ required to obtain a relative change of the transverse resistance $\overline{\Delta R_{xy}}/\Delta R_{xx} \geq 10^{-5}$ as a function of pulse length computed from the data in Fig. 4.4.

in the device diffuses to the substrate and warms it up. The heat diffusivity of the Si-based substrates varies little with increasing temperature [161, 164], whereas the heat diffusivity of Al_2O_3 drops from $\sim$28 $mm^2\,s^{-1}$ at room temperature, to $\sim$15 $mm^2\,s^{-1}$ at 100 °C, and $\sim$ 8 $mm^2\,s^{-1}$ at 400 °C [162]. Therefore, Al_2O_3 becomes significantly less efficient in dissipating heat for the longer pulses, which explains the converging trend of the curves shown in Figure 4.5.

4.9 Size effects

The power density dissipated in Pt is given by $V^2/(\rho\, L^2)$, where L is the effective length of the pulse path, which is approximately independent of the device width. As the current distribution in the Hall cross is inhomogeneous, however, we find that the device width strongly influences the amplitude of ΔR_{xy}. More precisely, we observe that ΔR_{xy} increases as the ratio between the area of the Hall cross and the length of the excited path decreases. Figure 4.6(a) reports ΔR_{xy} as a function of pulse amplitude for Si_3N_4/Pt Hall crosses with width ranging from 2.5 μm to 12.5 μm in steps of 2.5 μm. To study the asymmetry induced by the writing current, only the top right quadrant of the device is pulsed, exciting mainly R_1 (see Sect. 4.3), in sequences of 10 pulse-repeats starting from 2 V and increasing in steps of 0.25 V until the device fails.

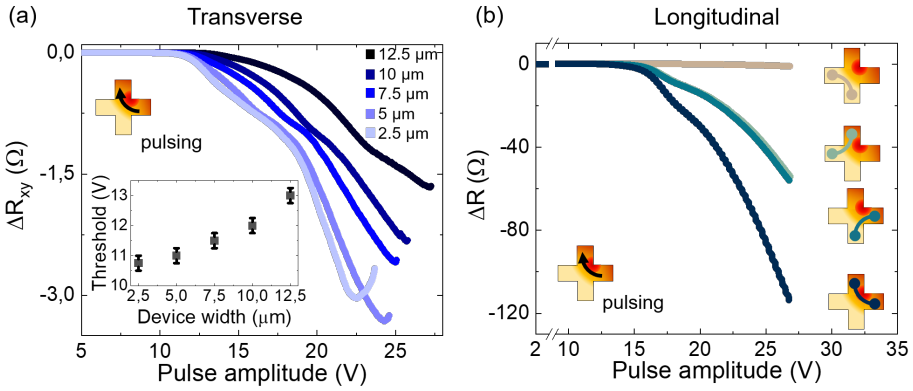

Figure 4.6: (a) Change of the transverse resistance ΔR_{xy} as a function of pulse amplitude for pulses sent around one corner of a Hall cross (see arrow). The data are measured in Si_3N_4/Pt(5nm) Hall crosses of different widths. (b) Change of the longitudinal resistance ΔR of the four quadrant paths of a 5-μm-wide cross as a function of pulse amplitude for pulses sent around one corner of the cross. The pulsing and measuring geometry are indicated in the schematic diagrams. The initial resistance of each path is, on average, $R_0 = 703 \pm 1\ \Omega$.

We observe that ΔR_{xy} is negative and decreases markedly up to a pulse amplitude of about 25 V, after which it starts increasing just before reaching the device breakdown. As argued in Sect. 4.5, the decrease of R_{xy} in this geometry corresponds to a decrease of the local resistivity, whereas the final upturn corresponds to an increase of the local resistivity. These measurements support the conclusion that competing effects take place in the crosses, consistently with thermal annealing and electromigration dominating the intermediate and higher voltage range, respectively. Importantly, smaller crosses present larger ΔR_{xy} signals compared to larger crosses. The inset in Fig. 4.6(a) shows that the pulse amplitude threshold for observing $\Delta R_{xy} \geq 0.01\ \Omega$ increases with the width of the cross, which we attribute to the larger proportion between the device area and the current-crowded area.

The variation of the longitudinal resistance ΔR measured between two adjacent arms of the cross, shown in Fig. 4.6(b), is consistent with the decrease of R_{xy} derived from the Wheatstone model. Moreover, we observe that the resistance changes not only occurs at the corresponding corner where the current density is the highest, but also in its surroundings and the pulsed arms. Before the breakdown of the device, the maximum relative change of the longitudinal resistance is $\Delta R/R \approx -16\ \%$ measured along the pulse path (black curve), $\approx -8\ \%$ in the two adjacent quadrant paths (light and dark green curves), and $\approx -0.14\ \%$ in the quadrant opposite to the pulse path (orange curve).

4.10 Influence of training effects on the resistance baseline

In this section, we analyze the nonlinear variation of the baseline of R_{xy} as a function of the pulse amplitude, which determines the shape of the traces shown in Fig. 4.1(b)-(c) and Fig. 4.3(a)-(c). We argue that this shape is due to training of the devices. To understand the effects of training, we first measure R_{xy} after pulsing the device only along P1, as shown in Fig. 4.7(a), then only along P2, as shown in Fig. 4.7(b), and finally run the sequence of alternate P1 and P2 pulses already described in Sect. 4.5, as shown in Fig. 4.7(c). The ramps shown in Fig. 4.7 (a)-(c) are taken consecutively with no waiting time between each other. During the first ramp, R_{xy} progressively decreases with the increasing number of P1 pulses. The signal of the second ramp starts from the value of R_{xy} attained at the end of the first ramp and varies in the opposite direction with an increasing number of P2 pulses. We note that here the relaxation process (Fig. 4.2) is not visible because of the short period of time elapsed during the ramp. By overlapping the first and second ramp [black dashed line and red line in Fig. 4.7(b)], we observe that the end value of R_{xy} in the P2 ramp is smaller by about $\approx 20\ \%$ compared to the P1 ramp. This asymmetry between the P1 and P2 response is attributed to the training of the device during the first ramp, as P1 pulses also partially affect the resistance of the P2 pulse path (see Fig. 4.6). This interpretation was confirmed by inverting the order of the pulses, namely when the P2 ramp preceded the P1 ramp in a pristine device, which led to the opposite asymmetry. Thus, the amplitude of ΔR_{xy} following P1 and P2 pulses depends on the pulsing history as well as from possible structural imperfections in the Hall cross due to inhomogeneous growth or patterning.

When considering a ramp of alternating P1 and P2 pulses, the asymmetry of ΔR_{xy} between P1 and P2 pulses results in a nonmonotonic baseline of R_{xy} that can be mistaken for drift, but is actually the signature of unequal responses to P1 and P2 pulses. In Figure 4.7(c), as the same number of pulses have been applied to the four corners in (a) and (b), the resistance changes along the paths of P1 and P2 are partially balanced. Hence, the ramp with alternate pulses along P1 and P2 is close to symmetric. In general, however, the device never goes back to a fully balanced state after pulsing along P1 and P2, giving rise to different baseline shapes, as observed, e.g., in Fig. 4.1(b)-(c) and Fig. 4.3(a)-(c). To see how this occurs in practice, we have simulated the P1 and P2 pulsing ramps starting from the curves shown in Fig. 4.7(a)-(b), computing the sum of the points measured along P1 and P2 (alternating 5 P1 pulses and 5 P2 pulses), and artificially removing or introducing asymmetries

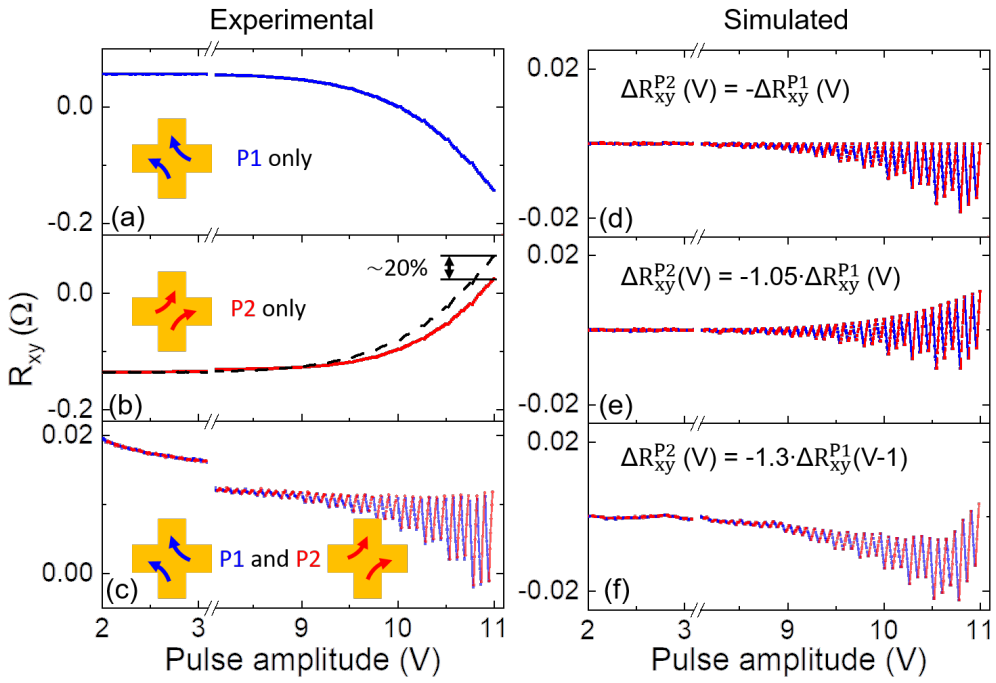

Figure 4.7: Variation of R_{xy} in a 10-μm-wide Si_3N_4/Pt cross as a function of pulse amplitude for P1 (a), P2 (b), and P1 and P2 pulses (c). In each ramp, the pulse amplitude is increased in steps of 0.25 V. For each step, a sequence of 3 repeats of 5 consecutive P1 or P2 pulses of length $\tau = 1$ ms is applied. (d) Simulated device response to P1 and P2 pulsing calculated from the curves shown in (a,b) by assuming a symmetric response along P1 and P2, $[\Delta R_{xy}^{P2}(V) = -\Delta R_{xy}^{P1}(V)]$, (e) a 5% higher ΔR_{xy} for P2 pulses, $[\Delta R_{xy}^{P2}(V) = -1.05 \cdot \Delta R_{xy}^{P1}(V)]$, and (f) a 30% higher amplitude and a 1 V shift of the threshold for P2 pulses, $[\Delta R_{xy}^{P2}(V) = -1.3 \cdot \Delta R_{xy}^{P1}(V-1)]$.

in response to P2 pulses ($\Delta R_{xy}^{P2}(V)$) relative to P1 ($\Delta R_{xy}^{P1}(V)$). The results are shown in Fig. 4.7(d)-(f), where we reproduce different baselines by assuming (d) a symmetric response with $\Delta R_{xy}^{P2}(V) = -\Delta R_{xy}^{P1}(V)$, (e) a 5% higher response along P2, $\Delta R_{xy}^{P2}(V) = -1.05 \cdot \Delta R_{xy}^{P1}(V)$, and (f) an asymmetric response of the device along P2 by shifting the voltage axis by 1 V and increasing the amplitude of the response by 30% such that $R_{xy}^{P2}(V) = -1.3 \cdot \Delta R_{xy}^{P1}(V-1)$. In agreement with the experiments, we see that the resistance change can take three forms: the baseline of ΔR_{xy} can stay constant at the first value of the series with R_{xy} moving back and forth with pulses along P1 and P2 [Fig. 4.7(d)], tilt upwards or downwards [Fig. 4.7(e)], or describe a nonmonotonic curve similar to a "pipe" [Fig. 4.7(f)].

Interestingly, the shape of R_{xy} reported in Fig. 4.7(e) can be misinterpreted as a symmetric response to P1 and P2 pulses because the excursion of R_{xy} appears to be symmetric around a central value. However, a symmetric response implies the

ability to return always to the initial value of R_{xy}, as shown in Fig. 4.7(d). More complex shapes are obtained when there is an asymmetry in both the amplitude response and threshold voltage required to induce appreciable changes of R_{xy}, as shown in Fig. 4.7(f). Note that in Ref.[130], a similar shape as the one reported in Fig. 4.7(f) has been associated with a partial reorientation of the Néel vector in an antiferromagnetic transition metal dichalcogenide. However, we repeatedly observed this behavior in Pt samples as well as NiO/Pt bilayers (see Fig. 4.7(c)), which shows that special care should be taken when analyzing the signal trace in such a device geometry and pulsing configuration.

4.11 Conclusions

In conclusion, we presented a comparative analysis of the current-induced resistance variation in Pt and NiO/Pt samples. A systematic study of the pulse amplitude and pulse length dependence of the transverse resistance performed on epitaxial and non-epitaxial films did not evidence significant differences between Pt and NiO/Pt layers. All our results are consistent with changes of the Pt resistivity occurring at the corners of the Hall crosses due to the current crowding effect. As also seen in recent works [139, 140, 141], the resistance can change in a saw tooth or step-like manner in both magnetic and nonmagnetic samples, and therefore the signal shape cannot be used to unambiguously identify magnetic switching, even if ex-situ imaging confirms the reversal of antiferromagnetic domains [134, 12, 13, 86]. Using a simple Wheatstone bridge model of a Hall cross, we identified competing effects responsible for the resistance changes: a decrease of the local resistivity surrounding the pulsed corner due to thermal annealing of the Pt layer and an increase of the resistivity due to electromigration preceding the device breakdown. After pulsing, the transverse resistance relaxes back towards the value before the pulse following a double exponential law with a short and long relaxation time of about a few minutes and 1 hour, respectively. The interplay between voltage amplitude and relaxation can give rise to nonmonotonic changes and even sign inversion of the variation of resistance. The substrate, apart from determining the crystalline quality of the samples, plays an essential role in dissipating heat away from the Pt line during pulsing. Substrates with a large thermal diffusivity such as sapphire allow for using a significantly broader range of pulse amplitudes without causing changes of the resistance due to current-induced annealing of Pt, thus providing a better chance of measuring magnetic switching by electrical means without artifacts. At constant pulse amplitude, larger devices show reduced resistance changes compared

to smaller devices owing to the larger proportion between the device area and the current-crowded area. Finally, we find that the current-induced changes of the transverse resistance are superimposed onto a nonmonotonic baseline whose shape depends on structural imperfections and device asymmetry as well as on the pulsing history of the sample. Our results provide a systematic overview of current-induced resistance changes in single metal layers and antiferromagnet/metal bilayers. These signals have a nonmagnetic origin and might either obscure or overlap with the magnetoresistive signals due to the switching of antiferromagnetic domains in antiferromagnet/metal bilayers.

Acknowledgments This work was funded by the Swiss National Science Foundation (grant number PZ00P2-179944).

5 Control of domain wall motion velocities with exchange bias

Summary

We investigate the motion of magnetic domain walls driven by magnetic fields and current-driven spin-orbit torques in an exchange-biased system with perpendicular magnetization. We consider Cr_2O_3/Co/Pt trilayers as model system, in which the magnetization of the Co layer can be exchanged-biased out-of-plane or in-plane depending on the field cooling direction. In field-driven experiments, the in-plane exchange bias favors the propagation of the domain walls with internal magnetization parallel to the exchange bias field. In current-driven experiments, the domain walls propagate along the current direction, but the domain wall velocity increases and decreases symmetrically (anti-symmetrically) for both current polarities when the exchange bias is parallel (perpendicular) to the current line. At zero external field, the exchange bias modifies the velocity of current-driven domain wall motion by a factor of ten. We also find that the exchange bias remains stable under external fields up to 15 kOe and ns-long current pulses with current density up to 3.5×10^{12} A/m. Our results demonstrate versatile control of the domain wall motion by exchange bias, which is relevant to achieve field-free switching of the magnetization in perpendicular systems and current-driven manipulation of domain walls velocity in spintronic devices.

This chapter is based on the publication "Control of field- and current-driven magnetic domain wall motion by exchange-bias in Cr_2O_3/Co/Pt trilayers" (Ref. [165]). Dr. Charles-Henri Lambert fabricated the samples and performed crystallographic characterization using XRD techniques. Dr. Federico Binda assisted in understanding and analyzing the XRD measurements. I conducted the transport measurements and DW motion experiments, and analyzed the data. Patrick Helbingk designed and fabricated new poles for the electromagnets in the MOKE microscope setup. Dr. Saul Vélez, Dr. Paul Noël, Dr. Charles-Henri Lambert, Prof. Pietro Gambardella, and I interpreted the results and co-wrote the manuscript.

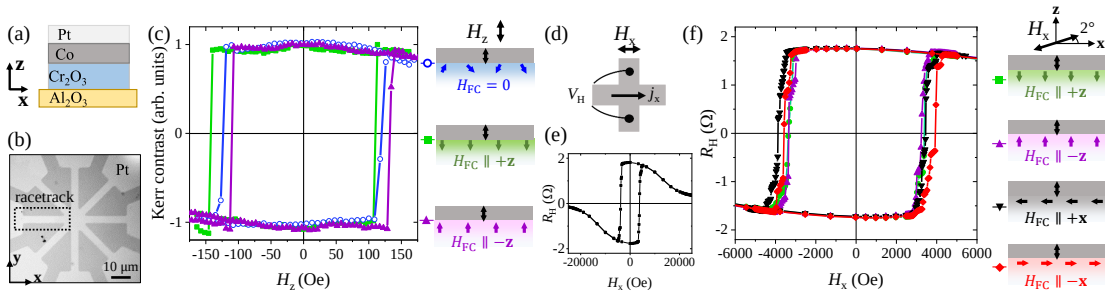

Figure 5.1: (a) Cross-section schematic of the sample and coordinate system. (b) Image of the device consisting of 8 converging racetracks. (c) Hysteresis loop measured by integrating the MOKE contrast over a single racetrack as a function of OOP field H_z after zero field cooling (blue) and field cooling with $H_{FC} \parallel \pm\mathbf{z}$ (green and purple). The magnetization vector $\mathbf{m}$ of the Co layer is represented by the double black arrow and the expected alignment of the uncompensated Cr magnetic moments after zero-field cooling by the colored arrows. The Cr magnetic moments are aligned opposite to the field cooling direction as they couple antiferromagnetically to the Co magnetization. (d) Electric wiring and (e) anomalous Hall resistance R_H as a function of H_x. The field H_x is applied along the x-axis, parallel to the sensing current j, and with $\theta = 2°$ tilt towards the z-axis to promote sharp switching of the magnetization. The device shows clear OOP anisotropy with R_H converging towards 0 at high field as the magnetization is pulled in-plane. (f) Hysteresis loops measured by the anomalous Hall effect as a function of H_x after OOP field cooling ($H_{FC} \parallel \pm\mathbf{z}$ with $\theta = 90°$, green and purple) and IP field cooling ($H_{FC} \parallel \pm\mathbf{x}$ with $\theta = 0°$, black and red).

5.1 Introduction

Magnetic domain wall (DW) motion has been extensively studied in thin film structures to understand magnetization reversal processes [166, 167, 168, 91, 169] and realize memory and logic devices [170, 171, 172, 173]. Magnetic information can be encoded in DW along continuous strips, the so-called racetrack memories, and an external magnetic field or electric current can precisely displace the DW [22, 23, 24, 25]. Out-of-plane (OOP) magnetized ferromagnet/heavy metal (FM/HM) layers are very promising in this respect because their strong perpendicular magnetic anisotropy results in narrow DW with simple Néel or Bloch structure, which can be easily displaced by an OOP external magnetic field [94, 168, 174, 175, 104] or current-driven spin-orbit torques [56, 47, 176, 43, 48, 44, 49, 177, 105]. The type of DW and their chirality is determined by the Dzyaloshinskii-Moriya interaction (DMI) [47, 178], and the response of DW to external stimuli in these systems can be further tuned by interfacial engineering [179, 180, 181, 182, 183], coupling to additional magnetic layers [184, 185], and electric fields [186, 187].

Typically, reversing the direction of the field or current results in an opposite but symmetric displacement of the DW. Superposing an in-plane (IP) magnetic field breaks this symmetry, which results in different DW velocities depending on whether the DW moves parallel or antiparallel to the IP field direction [174, 175, 188]. This feature is of particular interest for magnetic logic devices where the IP field can promote or restrict the DW propagation along one IP direction, similar to a magnetic diode. However, variable and selective external fields cannot be easily embedded in miniaturized devices.

Instead of an IP magnetic field, the exchange bias field at the interface between an antiferromagnet (AFM) and a FM [59] can be used to break the symmetry and manipulate the DW dynamics. This concept has been successfully used in the context of field-free magnetization switching by spin-orbit torques [70, 71, 72, 69] as well as for field-driven DW motion, for which anti-symmetries in the domain structure and between the ascending and descending branch of the magnetization loop were found in exchange-biased systems [189, 190, 191, 192, 193, 194, 195, 196, 197]. Moreover, exchange bias can be used to create pinning sites in crossed FM and AFM wires [198, 199, 200] and to modify the DW tilt angle [201]. However, a systematic study of how exchange bias affects the DW motion in both field-driven and current-driven experiments is presently lacking.

Here we show that exchange bias in AFM/FM/HM trilayers with perpendicular magnetization can be used to control the direction of motion and velocity of the DW. We observe almost unidirectional expansion of domains along the exchange bias field in field-driven DW propagation, and a symmetric (anti-symmetric) modulation of the current-driven DW velocity under positive and negative current when the exchange bias field is parallel (perpendicular) to the current. Our model system is a Cr_2O_3/Co/Pt trilayer. The Co/Pt subsystem is well-known for its strong perpendicular magnetic anisotropy and efficient field- [168, 174, 175] and current-driven [176, 43, 48, 44, 177] DW dynamics. Cr_2O_3 is an insulating AFM that has been widely used to induce OOP exchange bias in Co/Pt and Co/Pd multilayers [202, 203, 204, 205, 62] as well as IP exchange bias in permalloy and CoPt thin films [206, 207, 208]. Additionally, our study shows that Cr_2O_3/Co/Pt can be exchange-biased either OOP or IP depending on the field cooling direction. Cr_2O_3 is also of particular interest as the AFM spin order can be efficiently manipulated via the magnetoelectric effect [202, 203, 204, 209] and is a prototype material for the realization of magnetoelectric random access memory [210, 211].

This paper is organized as follows: Section 5.2 describes the sample fabrication and experimental setup. Section 5.3 presents the magnetic characterization of

Cr_2O_3/Co/Pt as a function of field cooling direction. Section 5.4 and 5.5 report the field- and current-driven DW motion measurements as a function of exchange bias, respectively. In Section 5.6, we compare the effect on the DW velocity of exchange bias and an IP external magnetic field, which allows us to estimate the exchange bias field and DMI in our sample. Finally, we summarize our results in Sect. 5.7.

5.2 Sample fabrication and experimental setup

A trilayer of Cr_2O_3(120 nm)/Co(0.85 nm)/Pt(2 nm) was grown by magnetron sputtering on a Al_2O_3(0001) substrate. The numbers between brackets indicate the thickness of each layer. The Ar pressure during the growth was 3 mTorr and the base pressure lower than 5×10^{-8} mTorr. The Cr_2O_3, Co and Pt layers were all sputtered from nominal composition targets. The Cr_2O_3 layer was grown at 800° C and annealed at the same temperature for one hour, then cooled to room temperature for the deposition of the Co and Pt layers. The epitaxy of the Cr_2O_3 was investigated by X-Ray diffraction (XRD) and its thicknesses were measured via X-Ray reflectivity. XRD results confirmed the epitaxial growth of Cr_2O_3 thin film with the (0001) orientation on the Al_2O_3(0001) substrate. This corresponds to the typical growth on sapphire (0001) of rhombohedral Cr_2O_3 with the rhombohedron diagonal pointing out-of-plane (see Appendix 5.A). No traces of secondary crystal orientations of Cr_2O_3 could be measured. In this text we use the conventional hexagonal cell with the 4-axis notation to denote the crystallographic planes. Additional XRD azimuthal scans performed around the Cr_2O_3 [0001] direction confirmed the absence of crystal twinning. Atomic force microscopy analysis showed a smooth and homogenous film surface with root-mean-square roughness smaller than 0.5 nm. Finally, UV-lithography and reactive ion milling were used to pattern a set of 5 μm-wide and 50 μm-long racetracks, as shown in Fig. 5.1(a,b).

To set the exchange bias direction, the sample was placed on a heating stage and field cooled from $T = 320$ K to room temperature in a magnetic field $H_{\mathrm{FC}} = 1600$ Oe. The shift of the magnetic hysteresis loop opposite to the field cooling direction indicates the presence of negative exchange bias, as illustrated in Fig. 5.1(c)-(f), in agreement with previous reports in similar systems [62, 212, 205]. The Néel temperature was estimated as the minimum field-cooling temperature required to erase the exchange bias, $T_{\mathrm{N}} = 320$ K (see Appendix 5.B). The increase of T_{N} with respect to the bulk value of 307 K (Ref. [206]) is attributed to the compressive strain of Cr_2O_3(0001) grown on Al_2O_3(0001), as discussed in Appendix 5.B and Ref. [213]. Local reorientation of the exchange bias along the racetrack is also possible via

current-induced Joule heating. For this purpose, we employed a direct current of $j = 0.5 \times 10^{12}$ A/m^2 in a field of $H_{\mathrm{FC}} = 1600$ Oe. This technique is interesting for applications where the heat can be generated only locally, which is more energy-efficient than heating the whole sample [214, 215]. Experiments performed for both positive and negative current polarities showed that the the exchange bias is determined by the external magnetic field and that there is no significant effect of the spin-orbit torques, unlike in other AFM systems with higher T_{N} (Refs. [216, 217, 218]).

A wide-field magneto-optical Kerr effect microscope (MOKE) in polar configuration was used to image the OOP magnetization component of the Co layer. Magnetic contrast was enhanced by taking differential MOKE images, obtained by subtracting from each image a reference image captured in a fully magnetized state. Two sets of electromagnets generate the OOP and IP external field. Hysteresis loops measured by integrating the MOKE contrast over the racetrack area as a function of the OOP magnetic field H_{z} allowed us to evidence the presence of OOP exchange bias after field cooling, as shown in Fig. 5.1(c). For the current-driven DW motion, voltage pulses were injected in a racetrack using a sub-ns pulse generator. The impedance matching of the racetrack and pulse generator was achieved by connecting a $50\,\Omega$ resistor in parallel to the device, which reduces back reflection and shortens the pulse rise/fall time. We computed the average DW velocity along the racetrack, v_{DW}, as the total area spanned by the DW displacement divided by the racetrack width and pulse length.

The resistance of the 2 nm-thick Pt layer is expected to be much smaller than that of the 0.85 nm-thick Co layer, hence most of the current flows through the Pt layer. With this assumption, the device resistivity was estimated to be $\rho = 2.15 \times 10^{-7}$ Ωm from a 4-probe measurement of the longitudinal resistance $R = 1075\ \Omega$ of a 5-μm-wide and 50-μm-long Hall bar device. To evidence the presence of IP exchange bias, we measured the anomalous Hall resistance, $R_{\mathrm{H}} = V_{\mathrm{H}}/I$ with V_{H} the Hall voltage and I the sensing current, of the Co layer as a function of the external field H_{x} applied along the x-axis, with a 2° tilt towards the z-axis, as shown in Fig. 5.1(d-f). As R_{H} is proportional to the OOP component of the magnetization, this type of measurement yields information on the influence of IP exchange bias on the switching of the Co layer. All the measurements were performed at room temperature.

5.3 Out-of-plane and in-plane exchange bias in Cr_2O_3/Co/Pt

We measured the coercivity, H_c, and exchange bias field, H_{EB}, for OOP and IP field cooling by recording hysteresis loops as a function of OOP and IP applied fields, respectively. For the OOP hysteresis loop, we integrated the MOKE contrast over the racetrack shown in Fig. 5.1(b) as a function of the OOP field H_z. The hysteresis loop of the zero-field cooled device (blue curve) shown in Fig. 5.1(b) has a coercivity $H_c = 130 \pm 3$ Oe and is centered around $H_z = 0$ Oe, demonstrating no exchange bias. MOKE images show that the reversal occurs by domain nucleation and propagation. Upon positive (negative) OOP field cooling, the hysteresis loop (green and purple curves) shifts to negative (positive) field, corresponding to an OOP exchange bias of $H_{EB} = -(+)25 \pm 3$ Oe. The OOP H_{EB} is comparable to previous measurements performed near-room temperature in Cr_2O_3/Co/Pt [205]. In a simple model, we can represent the AFM spin configuration at the interface pointing opposite to the field cooling direction, as illustrated in Fig. 5.1(c), which couples antiferromagnetically to the Co spin and shifts the loops [62]. We measured no OOP exchange bias upon IP field cooling.

To measure the IP exchange bias, we recorded R_H as a function of the IP field, H_x, with 2° tilting towards the z-axis to allow sharp rotation of the magnetization, as explained above and illustrated in Fig. 5.1(d). The hysteresis loop as a function of H_x of the zero field-cooled device is plotted in Fig. 5.1(e). At $H_x = 3500$ Oe, R_H changes sign abruptly due to the reversal of the OOP Co magnetization. This reversal field corresponds to the OOP coercivity as $\cos(2^\circ) \times 3500 \approx H_c$. At fields above 3500 Oe the Hall resistance decreases and ultimately tends towards zero for $H_x > 20000$ Oe when the magnetization lies in plane ($m_z \approx 0$). Figure 5.1(f) shows the hysteresis loops as a function of H_x after positive (negative) OOP field cooling (green and purple curves) and IP field cooling (black and red curves). The loops are centered for the OOP field-cooled device, but shifted for the IP field-cooled device by 350 ± 50 Oe opposite to the field cooling direction. We cannot directly attribute these shifts to IP exchange bias along the x-axis as its projection along the z-axis is essentially zero, and thus should not contribute to the required OOP switching field. However, the shifts demonstrate that the AFM spin configuration at the interface is different upon OOP or IP field cooling. Similar shifts were observed when measuring IP hysteresis along the y-axis after field cooling along the y-axis, indicating no IP anisotropy. Similarly to AFM spin configuration upon OOP field cooling, we suppose that the AFM spins acquire an IP component opposite to the IP field during field

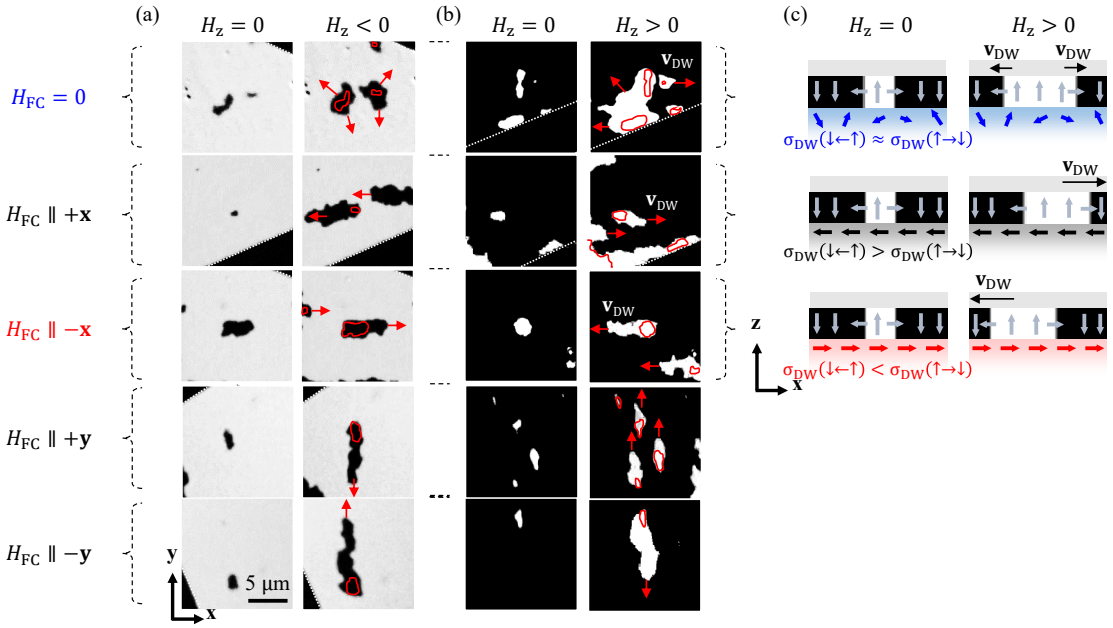

Figure 5.2: MOKE images of (a) down domains with $\mathbf{m} \parallel -\mathbf{z}$ (black contrast) and (b) up domains with $\mathbf{z} \parallel +\mathbf{z}$ (white contrast) after nucleation (left column) and expansion (right column) under $H_z = \mp\mathbf{z}$. The field pulse duration is 5 s. The first row shows the zero field-cooled device where the domains expand in all directions, and the next rows show the domains after IP field cooling with $H_{FC} = +(-)\mathbf{x}$ and $+(-)\mathbf{y}$. The down (up) domains expand preferably antiparallel (parallel) to the direction of H_{FC}. The red contours indicate the initial shape of the domains before the application of H_z; the red arrows indicate the favored DW motion. (c) Schematic of chiral DW and associated domain DW energy, σ_{DW}, for different field cooling directions. The IP exchange bias reduces σ_{DW} when it is aligned with the internal DW magnetization. Upon applying H_z, DW with small energy move faster than DW with large energy (see text for details).

cooling, as illustrated in Fig 5.1(f). The ensuing IP exchange bias modifies the energy landscape of the DW and induces anti-symmetric switching behavior as a function of H_x, as discussed in detail in Sect. 5.4. We further note that we measured negligible training effects on the exchange bias upon repeated cycling of the applied field (see Appendix 5.B).

The shift of the OOP hysteresis loops opposite to the field cooling direction indicates a collinear coupling at the interface between the Cr_2O_3 and the Co layers, with both AFM and FM spins pointing OOP. This behavior is consistent with the epitaxial growth of Cr_2O_3 with the (0001) orientation that favors the AFM spins alignment perpendicular to the surface [206, 62]. On the other hand, the shift of the hysteresis loops as a function of H_x indicates that the AFM spins can also be reoriented IP,

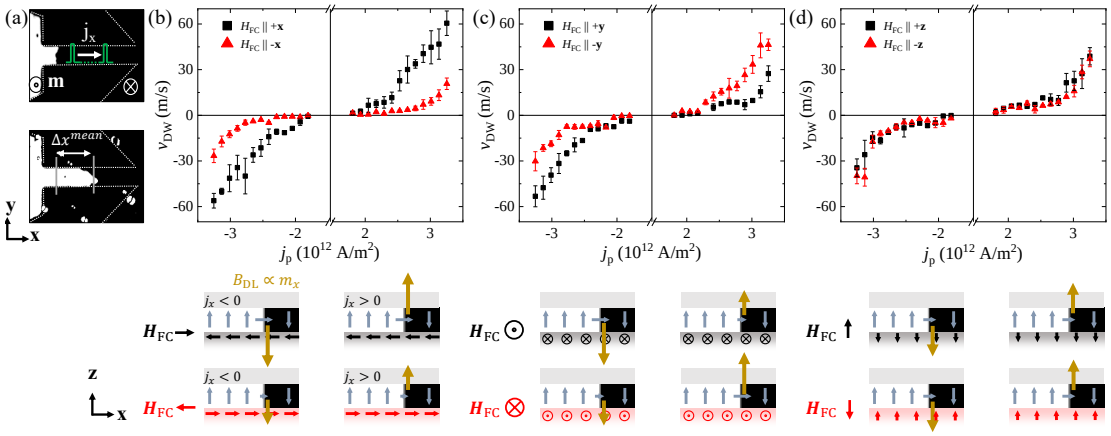

Figure 5.3: (a) MOKE images of an up-down DW before (top) and after (bottom) applying thirty 4-ns-long pulses of current density $j_p = 2.5 \times 10^{12}$ A/m^2 with 10 Hz repetition rate. (b-d) v_{DW} versus j_p of up-down DW in the absence of external field after field cooling with $H_{FC} \parallel \pm\mathbf{x}$ (b), $H_{FC} \parallel \pm\mathbf{y}$ (c), and $H_{FC} \parallel \pm\mathbf{z}$ (d). For each current density, v_{DW} is averaged over four pulse sequences; the error bars represent the standard deviation of each measurement. The sketches under each panel exemplify the effect of the exchange bias on $\mathbf{m}_{DW}$ (gray arrows) and B_{DL} (yellow arrow).

while the Co magnetization remains OOP. Similar IP canting of the Cr_2O_3(0001) spins was observed upon coupling to a NiFe layer with IP anisotropy [206, 207].

Additionally, the stable IP spin configuration of the Cr_2O_3 surface coupled to OOP Co spins supports the picture of noncollinear coupling between IP AFM spins and OOP FM spins as suggested in field-free switching of OOP FM layer by spin-orbit torques [70, 71, 72, 69].

5.4 Field-driven DW motion

The effect of the exchange bias onto the magnetization is further investigated by inspecting the field-driven DW motion, as reported in Fig. 5.2. For isotropic samples, in the absence of an exchange bias, an OOP field acts as a driving force onto the DW magnetization and makes the domains expand with no preferential direction [94, 168, 219, 47, 104]. An in-plane field, H_{IP}, however, can break this symmetry, because the DW energy, hence the DW velocity v_{DW}, depend on the relative orientation between the DW magnetization and H_{IP}, as reported in FM/HM systems [174, 175, 188].

In FM/HM systems, the DMI acts as an effective field H_{DMI} on the DW magnetization and stabilizes chiral Néel-type DW [47, 178], as illustrated in Fig. 5.2. In such a case, for H_{IP} applied parallel to H_{DMI}, the internal DW energy density is given by

$$\sigma_{\mathrm{DW}} = \sigma_0 + K_{\mathrm{D}}\,\lambda - \pi\,M_{\mathrm{s}}\,\lambda\,|H_{\mathrm{IP}} + H_{\mathrm{DMI}}| \tag{5.1}$$

with σ_0 the Bloch-type DW energy density, K_{D} the anisotropy energy density of the DW, and λ the DW width [47]. In the creep regime, when the DW are pinned, a decrease of the DW energy induces an increase of the DW velocity [94, 89, 175, 174, 108, 220, 221]. In the flow regime (not reached in our experiment), the DW velocity increase (decrease) is mainly due to the increase (decrease) of the DW width [222, 188]. As a result, applying H_{z} alone makes the domains expand in all directions, but adding H_{IP} lifts the DW degeneracy and leads to a higher velocity of the DW when H_{IP} is parallel to H_{DMI}.

By analogy with the effect of H_{IP} in FM/HM systems, we expect that the IP exchange bias will affect the DW dynamics. We examine the expansion of the domains under H_{z} by MOKE for different field-cooling directions, as shown in Fig. 5.2(a,b). The domains are nucleated using an alternating H_{z} from an uniformly magnetized state, and the images are taken before (H=0) and after applying $H_{\mathrm{z}} \lessgtr 0$ for $5\,\mathrm{s}$. In the zero-field cooled device the up and down domains tend to expand in all directions, similarly to a non exchange-biased FM/HM system. The rough contour of the domains is a signature of pinning due to the presence of the AFM layer and inhomogeneities in the sample. Interestingly, when the sample is IP field cooled with $H_{\mathrm{FC}} \parallel \pm\mathbf{x}, \pm\mathbf{y}$, the up domain tends to expand along the field-cooling direction, whereas the down domains expand opposite to it. A similar result is obtained when H_{IP} is applied to a zero-field cooled device. This shows that the exchange bias field acts as an effective field on the DW magnetization. Consequently, the internal DW energy density (Eq. 5.1) can be modified as

$$\sigma_{\mathrm{DW}} = \sigma_0 + K_{\mathrm{D}}\,\lambda - \pi\,M_{\mathrm{s}}\,\lambda\,|H_{\mathrm{IP}} + H_{\mathrm{DMI}} + H_{\mathrm{EB}}|. \tag{5.2}$$

Furthermore, because the DW velocity is higher when the exchange bias is parallel (antiparallel) to the up-down (down-up) DW magnetization and the DW motion is favored parallel to H_{DMI} according to Eq. 5.2, we deduce that H_{DMI} points "to the right" in up-down DW ($\uparrow\rightarrow\downarrow$) and "to the left" in a down-up DW ($\downarrow\leftarrow\uparrow$), giving overall a right-handed chiral DW ($\downarrow\leftarrow\uparrow\rightarrow\downarrow$), as expected for Pt on top of Co (Ref. [46, 223]). This model, in which the IP exchange bias influences v_{DW} through the variation of the DW energy density (Eq. 5.2), provides a straightforward interpretation of our results. We point out, however, that a quantitative comparison of the DW motion

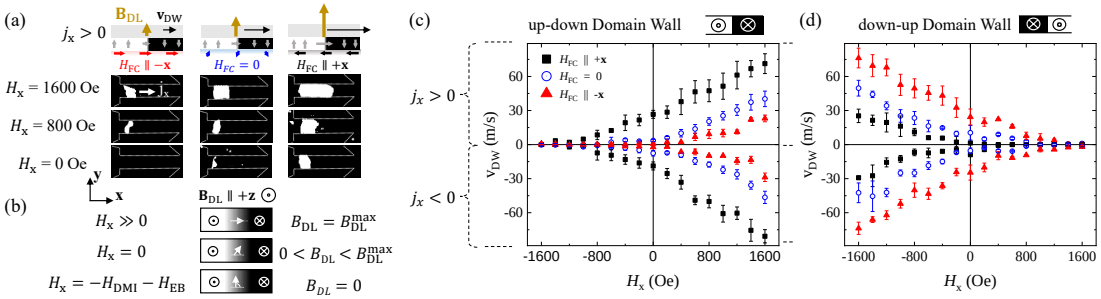

Figure 5.4: (a) MOKE images of the displacement of up-down DW after applying thirty 4-ns-long pulses of current density $j_p = 2.5 \times 10^{12}$ A/m^2 under $H_x = 1600, 800, 0$ Oe (top to bottom rows) for different field-cooling directions. (b) Schematics illustrating how $\mathbf{m}_{DW}$ and B_{DL} change depending on H_x, H_{DMI} and H_{FC}. (c) v_{DW} versus H_x for up-down and (d) down-up DW. $H_{FC} \parallel +(-)\mathbf{x}$ increases (decreases) the effective IP field $H_x \pm H_{EB}$ acting on the DW, horizontally shifting the curves to larger (smaller) fields with respect to zero field cooling. The current density is fixed to $|j_p| = 2.5 \times 10^{12}$ A/m^2, the pulse length and repetition rate are the same as in Fig. 5.3.

in Cr_2O_3/Co/Pt trilayers relative to Co/Pt would require including the effects of disorder on the DW velocity [89], in particular those due to exchange bias and the Cr_2O_3 substrate.

5.5 Current-driven DW motion

The current-driven DW motion in FM/HM systems is based on the absorption of the spin accumulation at the HM interface, which induces a damping-like spin-orbit-torque (DL-SOT) on the internal DW magnetization, $\mathbf{m}_{DW}$, [56, 47, 43, 48, 44, 49, 177, 105]. For Néel DW with $\mathbf{m}_{DW} \parallel \mathbf{j} \parallel \mathbf{x}$, the torque results in an effective easy-axis field, B_{DL}, which rotates $\mathbf{m}_{DW}$ towards $\pm\mathbf{z}$ depending on the relative alignment of $\mathbf{j}$ and $\mathbf{x}$. This rotation induces the propagation of the DW. The sign of B_{DL} changes upon inverting the current direction. Additionally, the torque induces a rotation of $\mathbf{m}_{DW}$ towards $\mathbf{y}$, which causes tilting of the DW as H_{DMI} favors $\mathbf{m}_{DW}$ perpendicular to the DW [104, 49, 105].

Starting from a DW with $\mathbf{m}_{DW} \parallel \mathbf{x}$, as in a racetrack, the application of an IP field H_x does not exert a torque on the DW magnetization, but rather enhances or opposes the effective field H_{DMI} that stabilizes the Néel DW configuration along $\mathbf{x}$. Because B_{DL} is maximum when $\mathbf{m}_{DW} \parallel \pm\mathbf{x}$, H_x increases or decreases the current-driven v_{DW}. The change of v_{DW} for a fixed H_x is anti-symmetric with respect to current inversion. A field H_y, on the other hand, either supports or opposes the rotation of

$\mathbf{m}_{\mathrm{DW}}$ towards $\mathbf{y}$. As a consequence, H_{y} results in an anti-symmetric variation of v_{DW} depending on the current direction [44, 49].

Based on the results of Sect. 5.4, we expect that the IP exchange bias should produce similar effects on v_{DW} as those described above for the IP fields $H_{\mathrm{x,y}}$. We thus investigate the current-driven DW motion in Cr_2O_3/Co/Pt racetracks for different directions of the IP exchange bias. We emphasize here the importance of minimizing Joule heating in our samples because of the relatively low Néel temperature of Cr_2O_3. We achieve this by utilizing short current pulses of limited amplitude. We verified that the exchange bias vanishes when applying pulses longer than $10\,\mathrm{ns}$ with current density $j_{\mathrm{p}} > 2 \times 10^{12}\,\mathrm{A/m^2}$ and cannot be retrieved without performing another field cooling (see in Fig. 5.8).

Images of an up-down DW before and after applying a series of current pulses in the absence of an external field are shown in Fig. 5.3(a). The DW was initially positioned in the racetrack using a combination of H_{x} and H_{z} external fields. The DW tends to be pinned at defects and at the edges of the racetrack, which deforms the DW boundary. Figure 5.3(b-d) shows v_{DW} as function of j_{p}, for $H_{\mathrm{FC}} \parallel \pm\mathbf{x}$, $\pm\mathbf{y}$, and $\pm\mathbf{z}$ with no applied external field. All the curves are characterized by a finite critical current for DW motion, a gradual increase of v_{DW} corresponding to the creep regime, and a curvature change representing the depinning threshold followed by a linear region in which v_{DW} increases proportionally to j_{p}, as expected in the flow regime. These curves are typical of spin-orbit torque-driven Néel DW motion [176, 43, 44].

However, we find substantial differences in the curves as a function of the field cooling direction. $H_{\mathrm{FC}} \parallel +(-)\mathbf{x}$ decreases (increases) the depinning threshold along both the positive and negative current direction [Fig. 5.3(b)]. For up-down DW, $H_{\mathrm{FC}} \parallel +(-)\mathbf{y}$ increases (decreases) the depinning threshold for positive current, and decreases (increases) it for negative current [Fig. 5.3(c)]. The opposite effects are observed for down-up DW. Hence, the effects of the IP field cooling on v_{DW} have the same symmetries as the effects of H_{x} and H_{y} in FM/HM system discussed above. The DW velocity versus current characteristics with $H_{\mathrm{FC}} \parallel \mathbf{y}$ is that of a DW diode, a useful component of magnetic DW logic circuits [173, 224]. Using the exchange bias, this functionality is obtained without a specific design of the racetrack [225, 226] or applying external magnetic field. On the other hand, $H_{\mathrm{FC}} \parallel \pm\mathbf{z}$ does not affect v_{DW} within the accuracy of our measurements [Fig. 5.3(d)].

Overall, we find that the exchange bias changes the low current regime by shifting the depinning threshold, whereas the DW mobility in the high current regime appear to be less affected. The exchange bias field significantly increases or decreases v_{DW} in

a symmetric or anti-symmetric way depending on the field-cooling direction, which is particularly interesting for controlling the DW motion in the absence of external fields.

5.6 Estimate of the IP exchange bias field by current-driven DW motion

The magnitude of the effective fields H_{EB} and H_{DMI} acting on $\mathbf{m}_{\mathrm{DW}}$ can be estimated by measuring v_{DW} versus H_{x} and finding the field at which $v_{\mathrm{DW}} = 0$. The reasoning here is similar to that applied to FM/HM systems in the absence of exchange bias [44, 227]. In these systems, when $H_{\mathrm{x}} + H_{\mathrm{DMI}} = 0$ the DW changes from Néel to Bloch-type, as the latter is the favored DW configuration for a thin film with OOP magnetization in the absence of DMI. This in turn stops the DW motion because $B_{\mathrm{DL}} = 0$ when $\mathbf{m}_{\mathrm{DW}} \parallel \pm\mathbf{y}$ [47]. In our exchange-biased Co layer the same occurs when $H_{\mathrm{x}} + H_{\mathrm{EB}} + H_{\mathrm{DMI}} = 0$, as illustrated in Fig. 5.4(a,b).

Figure 5.4(c,d) shows v_{DW} versus H_{x} measured for up-down DW (c), and down-up DW (d), for positive and negative current (upper and lower part of the panels) at fixed current density. We observe that v_{DW} of the up-down (down-up) DW increases for positive (negative) H_{x} and both DW move along the current direction at $H_{\mathrm{x}} = 0$. This behavior is characteristic of right-handed chiral Néel DW [43, 44, 227], which confirms the positive (negative) sign of H_{DMI} along $\mathbf{x}$ for up-down (down-up) DW as determined in Sect. 5.4. $H_{\mathrm{FC}} \parallel \pm\mathbf{x}$ shifts the curves to lower (higher) H_{x} with respect to zero field cooling, and the shift is symmetric for positive and negative current (upper and lower part of the graphs respectively). These shifts correspond to an effective IP field acting on the DW and can be attributed to the IP exchange bias, $H_{\mathrm{EB}} \approx 800\,\mathrm{Oe}$. At zero external field, the average v_{DW} increases by a factor ten, from $|2.4|$ m/s to $|23.6|$ m/s, when H_{EB} is along or opposite to H_{DMI}. By considering the field interval over which $v_{\mathrm{DW}} = 0$ in Fig. 5.4(c,d) for the DW in which the DMI and exchange bias field oppose each other, we estimate $H_{\mathrm{DMI}} \approx 1700$ Oe, which is consistent with reported values in Co/Pt systems [175, 174, 228].

We note that H_{EB} is larger than the shift of the hysteresis loops obtained by the anomalous Hall measurements of the OOP magnetization as a function of a tilted IP field, which amounts to $350 \pm 50\,\mathrm{Oe}$ [see Fig. 5.1(f)]. This is not surprising because the shifted loops in Fig. 5.1(f) reflect the influence of the IP exchange bias on DW nucleation, whereas the measurements in Fig. 5.4 reflect the influence of exchange bias on $\mathbf{m}_{\mathrm{DW}}$ and DW motion. More surprising is the fact that the IP exchange bias

is about one order of magnitude larger than the OOP exchange bias estimated by the shift of the hysteresis loops as a function of H_z. This is unexpected given the OOP anisotropy of the Co layer and of bulk Cr_2O_3(0001). We propose two different interpretations of this result. One possibility is that the model used to estimate the IP exchange bias cannot capture the full complexity of the system because it assumes a variation of v_{DW} solely based on the variation of the DW energy density, as exemplified by Eq. 5.2. Another possibility is that the in-plane compressive strain of Cr_2O_3(0001) grown on Al_2O_3(0001) favors the transition from easy-axis OOP anisotropy of bulk unstrained Cr_2O_3 to easy-plane IP anisotropy, as theoretically predicted [229]. The latter effect is supported by the 0.6% elongation of the Cr_2O_3 crystal structure along the [0001] direction measured by XRD (see Appendix 5.A).

We observe that v_{DW} has a nonlinear dependence on H_x close to the field at which $H_x + H_{EB} + H_{DMI} = 0$, unlike the linear dependence that is usually reported or assumed for FM/HM systems [44, 182, 49, 230]. We attribute this behavior to the gradual change of the DW from Néel to Bloch-type [Fig. 5.4(b)]. The change starts when $H_x + H_{EB} + H_{DMI}| \leq \frac{2}{\pi} H_K$ [227], where $H_K = \frac{\ln(2)\, t\, \mu_0\, M_s}{\pi \Delta}$ is the shape anisotropy field that favors Bloch DW, t is the FM thickness, M_s the saturation magnetization, and Δ the DW width. Taking $t = 0.85\,\text{nm}$, $M_s = 7.2 \times 10^5\,\text{A/m}$ from SQUID measurements, the perpendicular anisotropy field $\mu_0\, H_K^{\perp} = 1.5\,\text{T}$ from Fig. 5.1(e), the effective anisotropy energy $K_{eff} = \frac{\mu_0\, H_K^{\perp}\, M_s}{2} = 5.4 \times 10^5\,\text{J/m}^3$, and the exchange stiffness $A = 15\,\text{pJ/m}$ (Ref. [231]), we estimate $\Delta = \sqrt{A/K_{eff}} = 5.3\,\text{nm}$. Combining these values we find an estimated DW shape anisotropy $H_K \approx 350\,\text{Oe}$ which is in agreement with the range of fields over which v_{DW} changes nonlinearly starting from zero [Fig. 5.4(c,d)].

5.7 Conclusions

In summary, we studied the effect of exchange bias on the field- and current-driven DW motion of an AFM/FM/HM trilayer with perpendicular magnetic anisotropy and Néel DW stabilized by the DMI. We found that the exchange bias field in Cr_2O_3(0001)/Co/Pt can be set either OOP or IP depending on the field cooling direction, while the Co magnetization remains OOP. The possibility to induce IP exchange bias in a system with perpendicular magnetic anisotropy allows for tailoring the DW velocity and introduce directional asymmetry in the DW dynamics. Upon applying an OOP magnetic field, we find that an IP exchange bias induces almost unidirectional expansion of the DW with internal magnetization parallel to the exchange bias field. Upon applying a current, an IP exchange bias significantly offsets the depinning

threshold of the DW, leading to a manifold increase (decrease) of the DW velocity when the exchange bias field is set along the current direction parallel (antiparallel) to the DW magnetization. If the exchange bias field is set perpendicular to the current direction, the DW velocity increases (decreases) when the bias field opposes (favors) the tilt of the DW magnetization away from the current direction. To a first approximation, our results show that the IP exchange bias field adds to the effective DMI field and external IP field to determine the DW motion driven by an OOP field or spin-orbit torques. Exchange bias can thus be used to replace an external field to set a preferential direction of field-driven and current-driven DW motion in perpendicular AFM/FM/HM systems. By exploiting local current-induced heating, the exchange bias field can in principle be set independently on different racetracks, which is of interest to offset or harmonize the DW motion in magnetic memory and logic devices.

Acknowledgements

We are grateful to G. Krishnaswamy and A. Hrabec for insightful discussions. This work was funded by the Swiss National Science Foundation (Grant No. PZ00P2-179944 and 200020-200465). P.N. acknowledges support from the ETH Zurich Postdoctoral Fellowship Program 19-2 FEL-61. S.V. acknowledges support by the Spanish Ministry of Science and Innovation (Grant No. PID2021-122980OA-C53) and by the Comunidad de Madrid through the Atraccion de Talento program (Grant No. 2020-T1/IND-20041).

Data availability

The data that support the findings of this study have been deposited in the Research Collection database of the ETH Zurich and are available from https://doi.org/10.3929/ethz-b-000545102.

5.A Epitaxial growth of Cr_2O_3 on Al_2O_3(0001)

We characterized the crystal structure of Cr_2O_3 by XRD investigating a trilayer of Cr_2O_3(120 nm)/Co(1.1 nm)/Pt(2 nm) deposited on Al_2O_3(0001) in the same

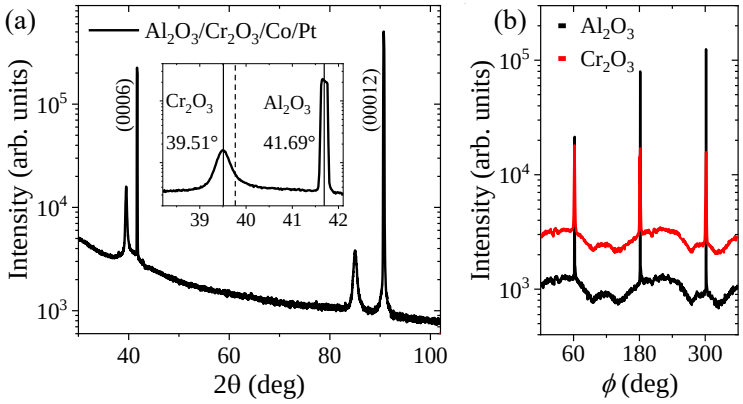

Figure 5.5: (a) XRD 2θ-scan of Cr_2O_3/Co/Pt deposited on α-$Al_2O_3(0001)$. The inset shows the enlarged scan around the peak corresponding to the (0006) plane of Cr_2O_3. The dashed line indicates the expected peak position of the (0006) plane of unstrained single-crystalline Cr_2O_3 (Ref. [213]). (b) Azimuthal XRD scan around the $[0001]$ direction of Cr_2O_3 (aligned to the $[0001]$ direction of Al_2O_3) showing the reflexes of the $(10\bar{1}4)$ planes for both Al_2O_3 (red) and Cr_2O_3 (black).

conditions as the sample used to examine DW motion. Figure 5.5(a) shows the XRD 2θ-scan. The peaks at $41.69°$ and $90.73°$ correspond to the (0006) and (00012) planes of Al_2O_3, respectively [232]. The peaks at $39.51°$ and $85.04°$ correspond to the (0006) and (00012) planes of Cr_2O_3 respectively (Ref. [233]). The absence of major additional peaks confirms the epitaxy of Cr_2O_3 film growing exclusively with the (0001) orientation. Further, the peak of the (0006) plane of Cr_2O_3 at $39.51°$ is shifted with respect to the peak position of unstrained single-crystalline Cr_2O_3 at $39.77°$ (Ref. [213], dashed line in the inset). This shift indicates that the Cr_2O_3 unit cell is elongated along the out-of-plane direction. The out-of-plane lattice parameter c_{exp} of the film is measured using Bragg's law of diffraction $n\lambda = 2d\sin(\theta)$, where n is the diffraction order, $\lambda = 1.541$ Å the wavelength of the Cu $K_{\alpha 1}$ radiation and θ the Bragg angle. We estimate $c_{\text{exp}} = 13.671$ Å of the deposited Cr_2O_3 film (from the (0006) plane at $2\theta = 39.51°$) which differs from $c_0 = 13.593$ Å of unstrained single-crystal Cr_2O_3 (Ref. [213]). The unit cell is then elongated by $(c_{\text{exp}} - c_0)/c_0 = 0.6\%$ with respect to unstrained crystal.

We attribute this deformation to the in-plane lattice mismatch between the Cr_2O_3 epitaxial film and the Al_2O_3 substrate since the latter has an in-plane lattice parameter 4% smaller than the former. The Cr_2O_3 unit cell then exhibits an in-plane compressive strain, and consequently, also an out-of-plane tensile strain [213]. As discussed in detail in Appendix 5.B, this lattice deformation is expected to increase the Néel temperature T_N with respected to unstrained single-crystalline Cr_2O_3.

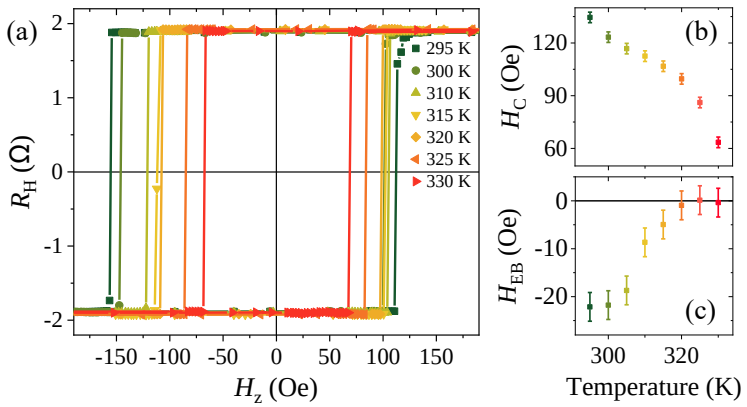

Figure 5.6: (a) Hysteresis loops at different temperatures. The exchange bias is set once before starting the full set of hysteresis loops by field cooling the sample from 320 to 295 K in an out-of-plane field $H_{FC} = 1600$ Oe. (b) Coercive field and (c) exchange bias field estimated from the loops shown in (a).

Absence of twinning in Cr_2O_3. Figure 5.5(b) shows the azimuthal XRD scan around the $[0001]$ direction of Cr_2O_3 (aligned to the $[0001]$ direction of Al_2O_3) showing the reflexes of the $(10\bar{1}4)$ planes for both Al_2O_3 (red) and Cr_2O_3 (black). The patterns of Al_2O_3 and Cr_2O_3 have the same three-fold in-plane symmetry, confirming the growth of twin-free Cr_2O_3 epitaxial films [234]. Furthermore, the alignment of the patterns shows that the in-plane orientation of the rhombohedral Cr_2O_3 lattice is aligned with the Al_2O_3 lattice [232].

5.B Exchange bias vs temperature and estimate of T_N

To estimate T_N we measured the anomalous resistance R_H as a function of the out-of-plane magnetic field H_Z after setting the exchange bias by field cooling the sample from 320 to 295 K in an out-of-plane field $H_{FC} = 1600$ Oe and recording hysteresis loops at different temperatures up to 330 K. The device is a single Hall cross of width 5 μm. The hysteresis loop, the coercive field H_c and the exchange bias field H_{EB} as a function of temperature are presented in Fig. 5.6(a-c). The coercive field and the exchange bias decrease gradually with increasing temperature. The coercive field is $H_C = 133 \pm 5$ Oe at $T = 295$ K and decreases to $H_C = 67 \pm 5$ Oe at $T = 320$ K. The exchange bias is $H_{EB} = 22 \pm 5$ Oe at $T = 295$ K and vanishes at $T \geq 320$ K, indicating that $T_N \approx 320$ K.

Absence of training effects. Figure 5.7(a) shows ten consecutive magnetization cycles recorded at room temperature after field cooling the sample from 320 K in an out-of-plane field $H_{FC} = 1600$ Oe. The coercive field and exchange bias are reported in

Fig. 5.7(b-c). These values do not vary significantly from cycle to cycle, indicating the absence of a training effect.

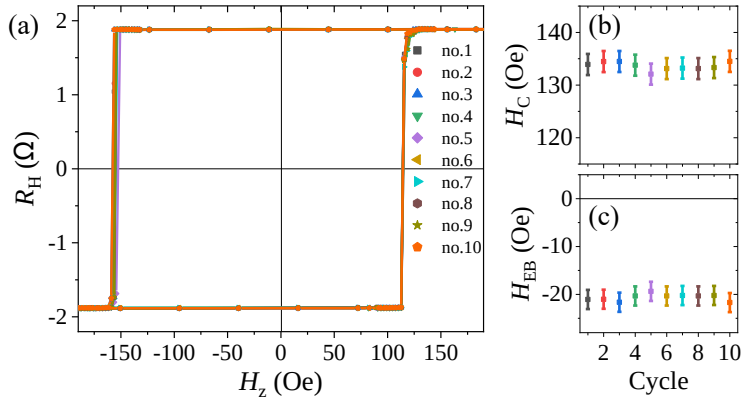

Figure 5.7: (a) Ten consecutive magnetization loops recorded by measuring the anomalous Hall resistance after field cooling the sample from 320 to 295 K in an out-of-plane field $H_{FC} = 1600$ Oe. (b) Coercive field and (c) exchange bias field estimated from the loops shown in (a).

Increase of the Néel temperature due to strain. The value of T_N deduced from the vanishing of exchange bias is higher than the bulk Néel temperature of Cr_2O_3. In line with theoretical calculations, we attribute the increase of T_N to the residual strain of Cr_2O_3 thin films grown on $Al_2O_3(0001)$. Kota et al. [235] calculated that T_N increases by 20% for a 5% increase of the ratio c_{exp}/a_{exp} relative to the unstrained ratio c_0/a_0, where a is the in-plane lattice parameter and c the out-of-plane lattice parameter of Cr_2O_3.

To estimate the experimental ratio, we use the out-of-plane lattice parameter $c_{exp} = 13.671$ Å calculated from the XRD 2θ-scan presented in Fig. 5.5(a) and assume the in-plane lattice parameter $a_{exp} = a_0 = 4.959$ Å. The assumption of using the unstrained value of a is partially motivated by observations made in Ref. [213], where TEM measurement performed on a 250-nm-thick Cr_2O_3 grown on α-Al_2O_3 showed in-plane relaxation of the Cr_2O_3 lattice. Because of the reduced thickness of our films compared to Ref. [213], however, we expect that $a_{exp} \lesssim a_0$ due to the compressive strain imposed by the Al_2O_3 substrate.

We then find $c_{exp}/a_0 = 2.76$, which is about 0.6% larger than the corresponding ratio in the unstrained crystal, $c_0/a_0 = 2.74$. According to the linear relation between strain and change of T_N from Ref. [235], the out-of-plane tensile strain corresponds to a 2.3% increase of T_N. Considering the bulk Néel temperature of 307 K (Ref. [62]), this gives an estimated Néel temperature of 314 K. Because a_{exp} is likely smaller than a_0 in our films, this estimate provides a lower limit for the expected increase of

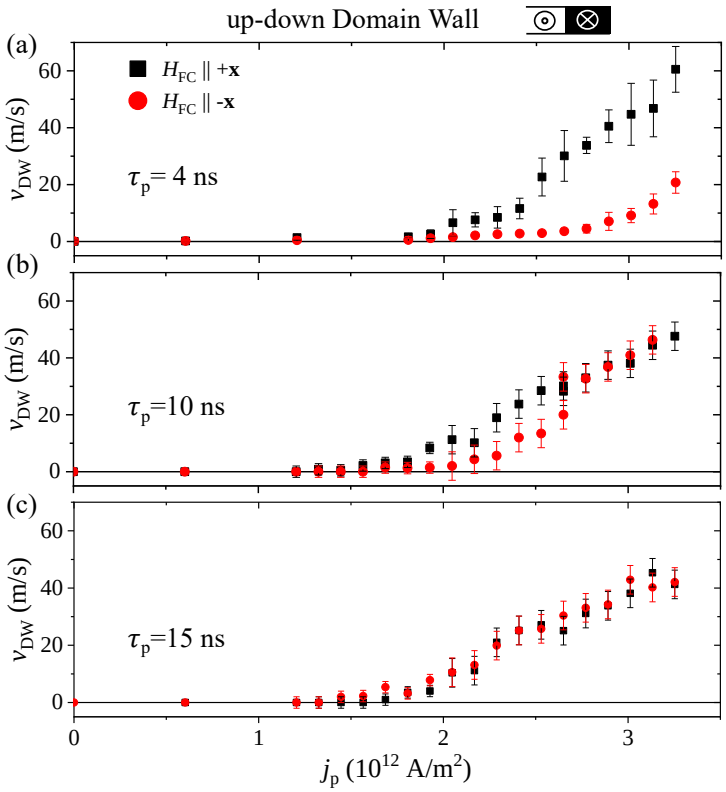

Figure 5.8: v_{DW} versus j_p for up-down DW after applying thirty pulses of length (a) $\tau_p = 4$ ns (b) 10 ns and (c) 15 ns with 10 Hz repetition rate in the absence of external field after field cooling with $H_{FC} \parallel \pm\mathbf{x}$. For each current density, v_{DW} is averaged over four pulse sequences; the error bars represent the standard deviation of each measurement.

T_N due to strain, which is in good agreement with $T_N \approx 320$ K obtained from the measurements reported in Fig. 5.6(c).

5.C Current-induced domain wall velocity for different pulse lengths

Figure 5.8 shows the DW velocity v_{DW} versus j_p for different pulse lengths (a) $\tau_p = 4$ ns, (b) $\tau_p = 10$ ns and (c) $\tau_p = 15$ ns. All the curves are characterized by a finite critical current for DW motion, a gradual increase of v_{DW} in the creep regime and a depinning threshold preceding the flow regime in which v_{DW} increases linearly with j_p, as discussed in Sect. 5.5.

We observe that the curves for $H_{\mathrm{FC}} \parallel \pm\mathbf{x}$ measured using the shorter pulses with $\tau_{\mathrm{p}} = 4$ ns are well separated due to the exchange bias favoring DW propagation along the field cooling direction (see Sect. 5.5). For $\tau_{\mathrm{p}} = 10$ ns, the curves superimpose at $j_{\mathrm{p}} > 2.5 \cdot 10^{12}$ A/m^2 and for $\tau_{\mathrm{p}} = 15$ ns the curves overlap in the entire range of current density. This behavior indicates that the device temperature remains below T_{N} at intermediate pulse lengths and current density, but exceeds T_{N} for longer pulse length and higher currents due to Joule heating.

Additionally, we observe that for $H_{\mathrm{FC}} \parallel +\mathbf{x}$ the depinning threshold, estimated as the current density above the creep regime where the curvature changes [109], decreases upon increasing τ_p, from $j_{\mathrm{d}}(\tau_{\mathrm{p}} = 4 \text{ ns}) \approx 2.2 \cdot 10^{12}$ A/m^2 to $j_{\mathrm{d}}(\tau_{\mathrm{p}} = 10 \text{ ns}) \approx 2 \cdot 10^{12}$ A/m^2 and $j_{\mathrm{d}}(\tau_{\mathrm{p}} = 15 \text{ ns}) \approx 1.8 \cdot 10^{12}$ A/m^2. This decrease is expected based on the higher temperature reached by the sample for longer pulses, which favors the thermally-activated depinning of DW.

6

A study of magnetic properties and domain wall dynamics in a ferrimagnetic Pt/CoGd/Cr trilayer system

In Chapter 4, we investigate the current-induced switching of antiferromagnets, and in Chapter 5, we study the control of magnetic domain wall motion in ferromagnets through exchange bias with an antiferromagnet. These studies provide valuable insights into the mechanisms governing these processes and their potential applications in next-generation spintronic devices. As we transition to the final chapter, our focus shifts to domain wall motion in ferrimagnets, a distinct class of magnetic materials with unique properties that offer substantial potential for the advancement of spintronics.

Ferrimagnets are characterized by antiferromagnetically coupled spin sublattices with unequal magnetic moments and gyromagnetic ratios [236]. This composition not only links ferrimagnets to the antiferromagnetic materials studied earlier but also results in distinctive magnetic ordering and compensation points, leading to behaviors that differentiate them from their antiferromagnetic counterparts. By exploring the dynamics of domain wall motion in ferrimagnets, we aim to expand our understanding of the broader family of magnetic materials and identify novel approaches to harnessing their properties for the development of more efficient and versatile spintronic devices.

Summary

Ferrimagnets are increasingly popular for spintronics due to their tunable magnetic properties and fast magnetization dynamics. Recent studies report ultrafast current-driven domain wall motion in heavy-metal/rare-earth-transition-metal bilayers such as Pt/CoGd, where the Pt layer provides spin current and the interfacial DMI favors chiral Néel-type domain walls in the CoGd layer. Here, we investigate the magnetic properties and domain wall dynamics in a Pt/CoGd/Cr trilayer with perpendicular

anisotropy, where the top Cr layer provides additional current-induced torque owing to the orbital current that is converted into a spin current in CoGd. To disentangle the effects of orbital current and spin current, we perform a systematic study on a series of samples with various CoGd compositions and different thicknesses of the Cr layer (1 nm and 8 nm). Our observations show that the current-induced domain wall mobility increases by more than 20% in 8 nm-thick Cr samples compared to 1 nm-thick Cr samples, indicating the presence of additional torques from the Cr top layer. The pinning barriers are dependent on the CoGd composition but independent of the Cr thickness. Additionally, we find that the maximum domain wall mobility occurs past the angular momentum compensation point due to large pinning barriers that dominate over intrinsic ferrimagnetic dynamics. This study opens new perspectives in achieving high current-induced domain wall velocity in ferrimagnets using light metals for high-speed spintronics devices.

This chapter is based on a manuscript in preparation and is therefore subject to change. The information presented here should be considered preliminary and not final. Dr. Min-Gu Kang fabricated the samples and performed the SQUID measurements. Dr. Min-Gu Kang and I performed the transport measurements. I conducted the DW motion measurements. Dr. Min-Gu Kang, Prof. Pietro Gambardella, and I interpreted the results.

6.1 Introduction

Rare-earth transition metal (RE-TM) ferrimagnets have gained significant attention in spintronics due to their unique tunable magnetic properties [237, 27]. The magnetic properties, such as saturation magnetization, magnetic anisotropy, and magnetization dynamics, can be modified by adjusting the atomic composition $RE_x - TM_{1-x}$ and temperature [238]. They possess smaller magnetic moments compared to ferromagnets, reducing overall stray fields in densely packed magnetic layouts. Overall, these materials enable more flexibility in experimental and practical applications [30, 26, 27].

One interesting phenomenon in RE-TM ferrimagnets is the behavior of domain walls (DW) under the influence of magnetic fields or electric currents. DWs exhibit a significant increase in velocity around the angular compensation point, which can be fine-tuned by adjusting the atomic composition or temperature [28, 30, 31].

The ability to control the DW velocity is crucial for the development of spintronics devices, including magnetic racetrack memory and logic gates [32, 33, 34, 35].

Both theoretical and experimental research have focused on understanding the current-induced motion of DWs under the influence of spin-transfer torque (STT) [239, 240, 241, 242] and spin-orbit torque (SOT) [243, 244, 245, 246, 247]. In the STT system, the charge current is spin-polarized within the ferrimagnet, which applies torque at the DW transition, triggering the motion. In the SOT system, an adjacent heavy metal (HM) is in direct contact with the ferrimagnet. The charge current in the HM layer becomes spin-polarized due to the interfacial Rashba-effect or spin-hall effect (SHE), inducing a damping-like spin-orbit torque (DL-SOT) on the internal DW magnetization $\mathbf{m}_{\mathrm{DW}}$, which triggers the DW motion.

Recently, experimental studies have shown that light metals can be the source of orbital current [248], which can then be converted into a spin current by a metal with spin-orbit coupling (SOC), significantly increasing the torque efficiency [249, 119, 118]. However, this orbital-spin conversion requires a conversion layer with SOC, and there have been few reports showing that the orbital-to-spin conversion can be done within magnetic materials with compounds having SOC [118, 119].

In this study, we investigate the spin-orbit torques and DW motion in heavy-metal/ ferrimagnet/ light-metal samples consisting of Pt/CoGd/Cr trilayers. Pt/CoGd is well known for its strong perpendicular anisotropy and current-induced DW dynamics [250, 28]. The bottom Pt layer serves as a source of SOT, owing to the spin Hall effect in Pt, and simultaneously generates a strong interfacial Dzyaloshinskii–Moriya interaction (DMI) that favors chiral Néel-type DW in the CoGd layers [250, 28]. On the other hand, Cr, a light metal, is known to generate strong orbital current and little spin current [117, 119, 251, 118]. The orbital current should be converted into spin current within the CoGd layer through the Gd atoms with strong spin-orbit coupling (SOC), eventually leading to a spin torque [119]. Due to the relatively long orbital diffusion length in Cr ($\lambda_{\mathrm{L}} \approx 20\,\mathrm{nm}$) [118], a significant effect of the orbital current is expected in relatively thick Cr layers. Therefore, the aim is to disentangle the effect of spin current from the Pt bottom layer and the effect of the orbital current from the Cr top layer by comparing Pt/CoGd/Cr(1 nm) and Pt/CoGd/Cr(8 nm) samples. Moreover, by varying the relative amount of Co and Gd in the ferrimagnet while keeping the Pt and Cr thickness constant, an increase in orbital to spin conversion is expected in Gd-rich samples compared to Co-rich samples, leading to stronger torques.

This chapter is organized as follows: Section 6.2 describes the sample fabrication and experiment setup. Section 6.3 presents the magnetic characterization of Pt/CoGd/Cr

samples and gives estimated values of the angular and magnetization compensation composition. In Section 6.4, we conduct measurements of current-driven DW motion as a function of Gd composition and Cr thickness and discuss the role of pinning and Joule heating on the DW mobility. Finally, we summarize our results in Sect. 6.5.

6.2 Methods

We study series of Pt(2)/[Co(0.8)/ Gd(t_{Gd})]$_{n=2}$/Cr (1,8) multilayers, with the numbers in parentheses indicating the thickness in nanometers. The samples are grown by magnetron sputtering on Si/SiO_2(200) substrates with Si_3N_4(8) bottom and top capping layers, as illustrated in Figure 6.1(a). The bottom and top Si_3N_4(8) layers reduce oxidation of Gd by the Si/SiO_2 substrate, or by environment respectively. To simplify the notation, we will refer to theses samples according to the thickness of the Cr top layer as Cr(1) and Cr(8) samples.

Before depositing samples, the Si/SiO_2 substrates were sonicated in the acetone bath for 60 min with sonication intensity of 50% in order to remove any contaminant on the surface of the substrate. Then, the substrates were sonicated in the isopropyl alcohol bath for 30 min again with sonication intensity of 50% in order to completely remove the residual acetone on the surface of Si/SiO_2, which may alter the subsequent thin film quality. After the sonication processes, the substrates were kept submerged in the ethanol bath. The Hall bar and racetrack structures were patterned using the photolithography techniques. The bare wafers were taken into a clean room facility where the thin film samples were spin coated with an AZ 1505 photoresist. After the spin coating process, the photomask with Hall bars and racetracks is loaded on the mask aligner with the thin film sample where the UV light is exposed. Following the UV light exposure, the thin film samples are developed using the AZ 400K 1:4 developer.

When the photolithography processes are finished, the samples were loaded in the load lock chamber of the magnetron sputtering system. All samples are deposited using DC (or RF) sputtering with an Ar pressure of (or 3.7 mTorr (10.2 mTorr). The base pressure is lower than $5 - 0 \times 10^{-5}$ mTorr. The depositions are performed at room-temperature. The two repetitions of [Co(0.8) / Gd(t_{Gd}]$_{n=2}$ increase the out-of-plane magnetic anisotropy. The thickness of Gd, t_{Gd}, varies from 0.5 nm to 1.4 nm in step of 0.1 nm, hence changing the volumetric ratio of RE-TM from 17.2% to 37% Gd composition, i.e. $Co_{82.7}Gd_{17.2}$ to $Co_{63}Gd_{37}$, with the total CoGd thickness

varying from 2.6 to 4.4 nm. Finally, the devices are developed using the lift-off process in the acetone bath.

The resistances of the 3 nm-thick Pt layer and $1,8$ nm-thick Cr layer are expected to be much smaller than the [Co/Gd] multilayers, hence most of the current flows through the Pt and Cr layers. This assumption is supported by the fact that the device resistances are almost constant over the whole range of Gd composition wherein the total Co/Gd thickness varies from 2.6 nm in Gd $17,2\%$ samples to 4.4 nm in Gd 37% samples. The two-probes measurement of the longitudinal resistance in $10-\mu$m-wide and $100-\mu$m-long racetracks are $1330 \pm 20\ \Omega$ in Cr(1) samples and $810 \pm 20\ \Omega$ in Cr(8) samples.

For the current-driven DW motion measurement, voltage pulses are injected in a racetrack using a sub-ns pulse generator. The impedance matching of the racetrack and pulse generator is achieved by connecting a $50\,\Omega$ resistor in parallel to the device, which reduces back reflection and shortens the pulse rise/fall time. We compute the average DW velocity along the racetrack v_{DW} as the total area spanned by the DW displacement divided by the racetrack width and pulse length.

A wide-field magneto-optical Kerr effect microscope (MOKE) in polar configuration is used to image the OOP magnetization component of the CoGd layers. The LED light source emits blue light with a wavelength of $\lambda = 451 \pm 24$ nm. At this wavelength, the Kerr signal of the Co sublattice dominates the one of the Gd sublattice [252]. Magnetic contrast is enhanced by taking differential MOKE images, obtained by subtracting from each image a reference image captured in a fully magnetized state.

6.3 Angular and magnetic compensation composition

First, we examine the ferrimagnetic properties of our samples by measuring the magnetic moments in Cr(1) and Cr(8) films using SQUID under an out-of-plane field $B_{\mathrm{x}} = 400$ mT as a function of temperature, as shown in Figure 6.1(b). These curves are typical of ferrimagnetic CoGd [236], in which the net moment is near zero close to the compensation temperature T_{M}. In Cr(1) and Cr(8), T_{M} is below room temperature in $\mathrm{Co}_{68.8}\mathrm{Gd}_{27.2}$ and close to room temperature in $\mathrm{Co}_{68.6}\mathrm{Gd}_{31.4}$. We observe that T_{M} in samples with $31.4\,\%$ Gd content is larger than the reported values in [236]. We also note that for a given Gd content, the compensation temperature is different in Cr(1) and Cr(8). These points are discussed below when analyzing the compensation composition in patterned devices.

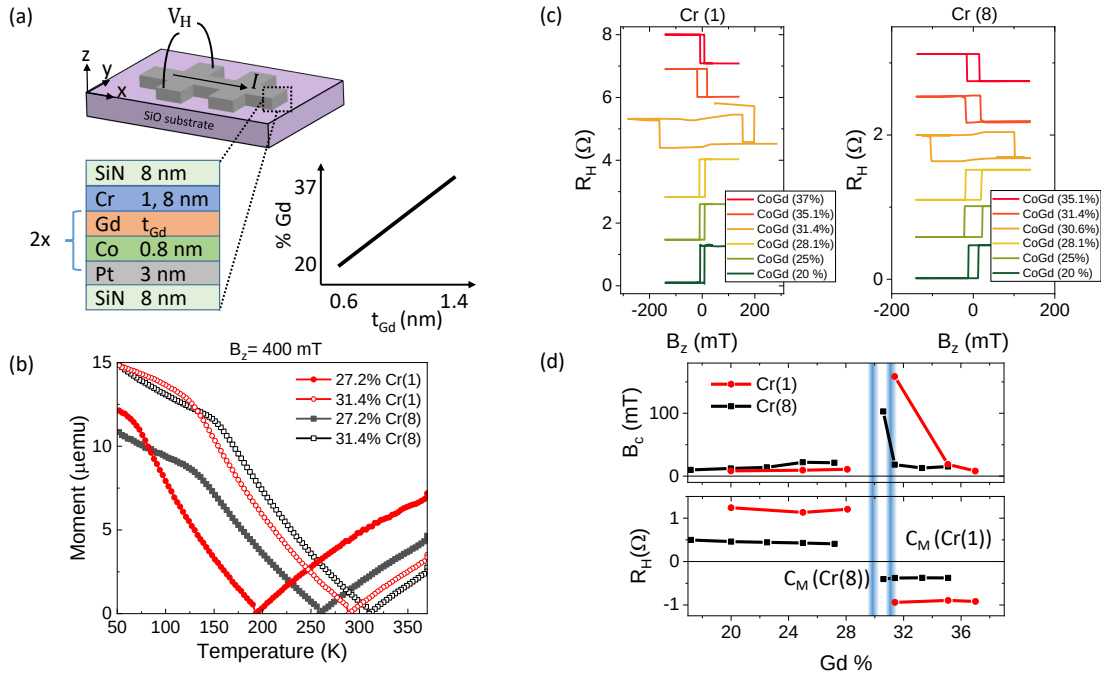

Figure 6.1: (a) Schematic of the device geometry and anomalous Hall resistance measurements. Cross section schematic of the sample with Gd composition plotted as a function of Gd thickness. (b) Magnetic moments measured by SQUID under $B_x = 400$ mT as a function of Gd content and temperature. (c) Hysteresis loops measured by R_H as a function of external field B_z in Cr(1) and Cr(8). The measurements are performed at room-temperature. (d) Coercive field B_c and AHE amplitude versus Gd composition. The divergence of the coercive field and inversion of the AHE sign indicate that magnetic compensation occurs at a composition c_M(Cr(1)) ≈ 31 % and c_M(Cr(8)) ≈ 30 % (blue vertical lines).

Next, we determine the magnetic compensation composition and coercive field B_c of the patterned devices by measuring the anomalous Hall resistance R_H while sweeping a magnetic field out-of-plane, as shown in Figure 6.1(a);(c). The samples display clear out-of-plane anisotropy, with R_H reaching saturation at high fields and nearly 100% remanence at zero field. The amplitude of R_H and the values of B_c are reported in Figure 6.1(d). In RE-TM ferrimagnetic alloys, R_H is mainly influenced by the TM sublattice. The positive (negative) sign of R_H indicates that the samples are Co-rich (Gd-rich) [253]. In Cr(1) and Cr(8) samples, R_H changes sign, and B_c reaches peak values in $Co_{68.6}Gd_{31.4}$ and $Co_{69.4}Gd_{30.6}$, respectively, indicating that the magnetic compensation composition at which $M_{Co} \approx M_{Gd}$ are approximately c_M(Cr(1)) $\approx 31\%$ and c_M(Cr(8)) $\approx 30\%$.

The magnetic compensation composition of Cr(1) and Cr(8) is higher than the reported value of $c_M \approx 25$ at room temperature for Pt(10)/CoGd(6) [253]. We attribute this to several factors. First, the presence of oxygen in the sputtering

chamber leads to the partial oxidation of Gd during sample growth, necessitating a higher Gd composition to achieve the magnetic compensation in the CoGd layers. Second, c_{M} in the Cr(1) samples is higher than in the Cr(8) samples, indicating that the effective Gd composition is lower in Cr(1) than in Cr(8). This difference suggests that Gd atoms may diffuse across the thin Cr(1) layer towards the SiN capping layer. GdN alloys can be energetically stable [254] and Gd has a tendency to migrate from the bulk towards the surface due to its surfactant effect [255]. As a results the Cr(1) layer may not be thick enough to act as an effective barrier against the diffusion of Gd atoms.

The total angular momentum of CoGd is the sum of the angular momentum of each sublattice, given by $A = M_{\mathrm{Co}}/\gamma_{\mathrm{Co}} - M_{\mathrm{Gd}}/\gamma_{\mathrm{Gd}}$, where M_{i} is the saturation magnetization and γ_{i} is the gyromagnetic ratio. The gyromagnetic ratio can be expressed as $\gamma_{\mathrm{i}} = \mu_0/\hbar g_i$, with g_i representing the g-factor [236]. Co and Gd possess similar g-factors ($g_{\mathrm{Co}} = 2.2$, $g_{\mathrm{Gd}} = 2$ [256]), and the angular compensation composition is close to c_{M}. In CoGd thin films, the empirical relationship c_{A} are $c_{\mathrm{M}} - 1.9\%$ has been established [28], yielding estimated values in our samples of $c_{\mathrm{A}}(\mathrm{Cr}(1)) \approx 29.1\%$ and $c_{\mathrm{A}}(\mathrm{Cr}(8)) \approx 28.1\%$.

6.4 Current-driven DW motion

In the following, we investigate the current-induced DW motion at room-temperature and under zero external field. Pt/CoGd is a well-studied system in which the Pt layer serves as a source of SOT due to the spin Hall effect, as illustrated in Figure 6.2(a). It also generates a strong interfacial Dzyaloshinskii-Moriya interaction (DMI), favoring chiral Néel-type DW in the CoGd layers [250, 28]. This system is similar to heavy-metal/ferromagnet bilayers and can also be described by the LLG equation, in which the dynamics of each sublattice can be combined into one effective spin system [257]. However, the effective gyromagnetic ratio γ_{eff} and effective damping parameter α_{eff} diverge at the angular compensation composition c_{A}. The direct consequence is that the DW motion becomes precession-free, maximizing the translational motion and thus the DW velocity [28, 250, 245]. This effect suppresses the saturation of the DW velocity due to the destabilization of DW chirality [47]. In the case of field-driven DW motion, this precession-free motion also maximizes the DW velocity and suppresses the Walker breakdown [29].

On the other hand, the Cr top layer is expected to generate both spin and orbital currents, as illustrated in Figure 6.2(a). The spin Hall conductivity $\boldsymbol{\sigma}_{\mathrm{S}}$ has an

opposite sign in Cr relative to Pt. Therefore, the spin current diffusing from the Cr should add up constructively to the torques generated by the Pt layer, but the spin Hall conductivity in Cr is much smaller than in Pt and thus can be neglected [118]. The orbital current generated in Cr is expected to apply torques by converting the orbital current to spin current through the Gd atoms. The strength of the torques depends on the intensity of orbital currents and the spin-orbit coupling of the ferrimagnetic CoGd layer. The orbital Hall conductivity of Cr has been reported to be larger than the spin Hall conductivity in Pt [118]. As a result, we expect a significant increase in the torques compared to Pt/CoGd due to the orbital current generated in Cr. Additionally, increasing the Gd content while keeping the Pt and Cr thickness constant is expected to increase the conversion of orbital to spin current, resulting in a continuous increase in the torques generated by the Cr layer. To the best of our knowledge, these effects have not been studied yet.

We note that the amount of generated torques by the Pt and Cr layers is proportional to the current density in each layer [26]. If the resistances of the Pt and Cr layers are considered to be independent of the CoGd layers [see in Sect.6.2], it is reasonable to assume that the applied voltage is proportional to the current density in each layer. This is because each layer in the Pt/CoGd/Cr conducts in parallel, and the applied voltage is proportional to the current density. Thus, we obtain $V_{\mathrm{p}} = R\, I_{\mathrm{p}} = \frac{\rho^l\, L}{w\, t^l}\, I_{\mathrm{p}} = \rho^l\, L\, j^l_{\mathrm{p}} \propto \rho^l\, j^l_{\mathrm{p}}$, where ρ^l represents the resistivity of Pt, CoGd, or Cr layers, L is the device length, and w and t^l are the width and thickness of the layers, respectively. Therefore, we compare the DW velocity as a function of the applied voltage for different Gd compositions.

We measure current-induced DW motion along $100-\mu$m-long and $10-\mu$m wide racetracks, as shown in Figure 6.2(a). In Figure 6.2(b), Kerr images of the DW displacement after applying a series of voltage pulses are displayed. To position the DW in the racetrack, a combination of in-plane and out-of-plane external fields was used before pulsing the current. Afterwards, the electromagnets were demagnetized before applying the pulses to reduce the spurious effects on the DW dynamics due to their remanent stray fields. The rough contour of the domains is due to pinning along the edges of the racetrack and inhomogeneities in the samples. The v_{DW} curves as a function of the voltage amplitude in Cr(1) and Cr(8) are shown in Figure 6.2(c) and (d), respectively. All the curves exhibit a finite critical current for DW motion, a gradual increase in v_{DW} corresponding to the creep regime (from 10 V to 30 V), and a curvature change representing the depinning regime (from 30 V to 55 V). The curves resemble the current-driven DW motion in Pt/CoGd alloys [250, 28, 258] and Pt/CoTb alloys [259]. The maximum velocity is around 330 m/s, which is of the same order as velocities in Ref. [250, 258] under zero external field. Velocities were

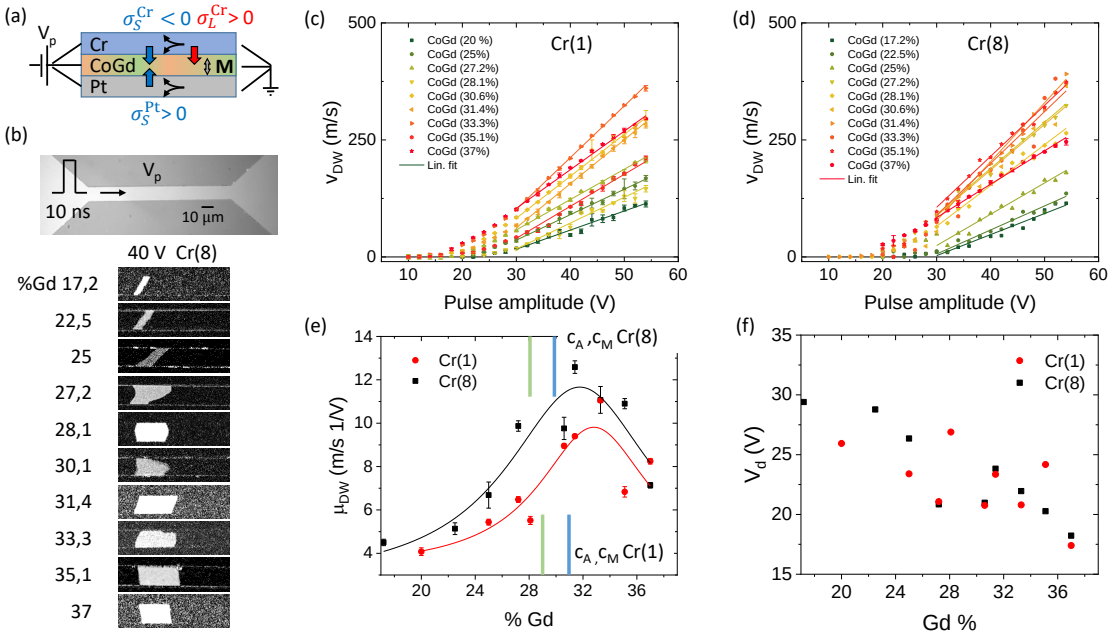

Figure 6.2: (a) Schematic of the spin and orbital current induced by an electric field in the Pt and Cr layers, generating torques on the CoGd magnetization. The arrows indicate the direction of the induced spin current (S, blue arrow) and orbital current (L, red arrows), taking into account the sign of the spin and orbital Hall conductivities $\boldsymbol{\sigma}_{\mathrm{S,L}}$. The strength of the torques depends on the intensity of the spin and orbital currents and the spin-orbit coupling of the ferrimagnetic CoGd layer. (b) Optical image of the racetrack for the domain wall motion measurements. Below are the Kerr microscopy images showing the domain wall motion in Cr(8) induced by 10 pulses of length 10 ns with amplitude $V_{\mathrm{p}} = 40\,\mathrm{V}$ with $10\,\mathrm{Hz}$ repetition rate. The measurements are performed at room-temperature. (c),(d) v_{DW} versus pulse amplitude V_{p} in Cr(1) and Cr(8). For each pulse amplitude, v_{DW} is averaged over three pulse sequences (30 pulses). (e) DW mobility μ_{DW} and (f) depinning voltage V_{d} versus Gd composition calculated from the linear fits in (c) and (d).

larger in Ref. [28], but an in-plane field along the current direction, $B_{\mathrm{x}} = 120\,\mathrm{mT}$, significantly increased the velocity.

Even though the DW achieves velocities greater than $200,\mathrm{m/s}$ at high voltage, we observe that there is no linear flow regime that can be fitted with $v_{\mathrm{DW}} \propto j_{\mathrm{p}} \propto V_{\mathrm{p}}$. Instead, the depinning regime appears to expand over a large voltage range, which may be due to the presence of stronger pinning in $[\mathrm{Co/Gd}]_{\mathrm{n=2}}$ multilayers compared to CoGd alloys. This behavior is similar to that of DW in Pt/[Co/Tb] multilayers [183]. In fact, the curves that we obtain are reminiscent of the low-temperature regime observed in Pt/CoGd alloys [250], where pinning is more significant than at high temperatures. We will discuss the impact of the depinning regime expanding over a large voltage range in more detail below, while comparing the maximum velocity as a function of the Gd composition.

We compute and report the DW mobility $\mu_{\mathrm{DW}} = v_{\mathrm{DW}}/V_{\mathrm{p}}$ and the depinning voltage V_{d} using linear fits in the depinning regime. The results, which are summarized in Figure 6.2(e) and (f), show that the Gd composition has a significant impact on both the DW velocity and depinning. We used a Lorentzian function as a visual guide to the data. Starting from the Co-rich region, μ_{DW} increases with Gd composition and reaches its maximum at around 31% in Cr(1) samples and 30% in Cr(8) samples. The maximum value of μ_{DW} in Cr(8) is 20% larger than in Cr(1), which suggests the presence of additional torques from the Cr top layer. This increase in mobility cannot be directly attributed to additional Joule heating from a thick Cr layer compared to thin Cr layer reducing the pinning energy barrier, since the depinning voltage V_{d} is comparable in both Cr(1) and Cr(8) samples, as shown in Figure 6.2(f). Further measurements on samples with increased Cr thickness must be performed to establish the contribution of the orbital toque.

Unexpectedly, in both Cr(1) and Cr(8) samples, the peak value of mobility occurs past the effective c_{M} rather than close to c_{A}. This differs from previous studies in heavy-metal/ferrimagnet systems [259, 31, 28, 250, 245]. Below, we discuss two possible reasons for this discrepancy: Joule heating and the special DW dynamic in the depinning regime.

Influence of Joule heating

Temperature plays a critical role in the study of current-driven DW in ferrimagnets because the angular compensation composition c_{A} shifts to higher Gd content with increasing temperature. This effect was measured in [236], where $c_{\mathrm{A}}(T - T_{\mathrm{RT}}) = c_{\mathrm{A}}(T_{\mathrm{RT}}) + [1\%/50\,\mathrm{K}]\,(T - T_{\mathrm{RT}})$ where T_{RT} is room-temperature as shown schematically in Figure 6.3(a). Therefore, Joule heating generated during the pulse can shift the maximum mobility from c_{A} towards a higher Gd content, modifying the shape of the DW mobility as a function of current, which is no longer monotonic [246, 28].

For example, consider a device with a specific Gd content where the angular compensation temperature is equal to room temperature ($T_{\mathrm{A}} = T_{\mathrm{RT}}$). In this case, the device will exhibit saturation of μ_{DW} at high current because Joule heating will increase the device temperature above room temperature, resulting in a non-zero total angular moment that eventually reduces μ_{DW}. On the other hand, a device with a larger Gd content, where T_{A} is higher than room temperature ($T_{\mathrm{A}} > T_{\mathrm{RT}}$), will display maximum mobility at high currents when Joule heating raises the device temperature to reach T_{A}. This effect was proposed in [28] to explain the shift of

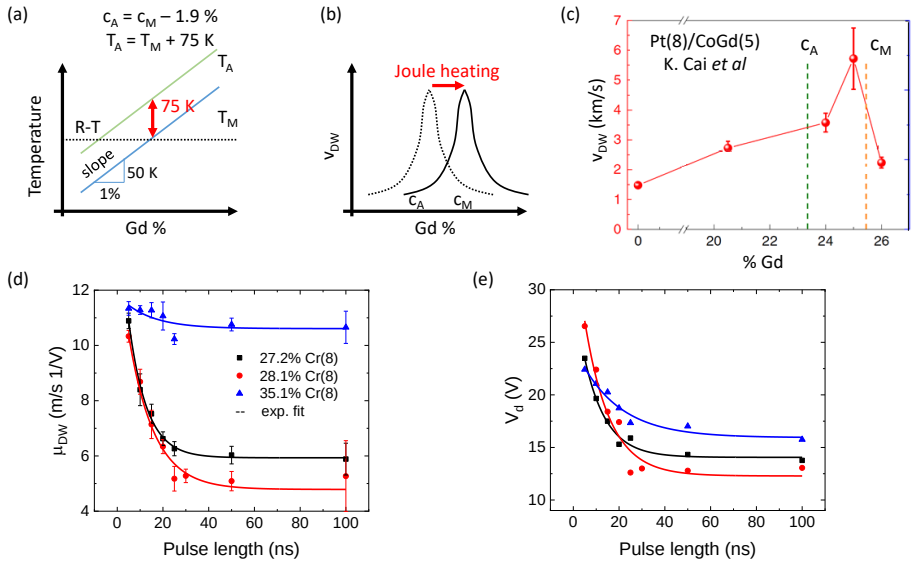

Figure 6.3: (a) Schematic of the angular compensation temperature T_A and magnetization compensation temperature T_M as a function of Gd content, based on [236, 28]. (b) v_{DW} versus Gd composition. The peak value of v_{DW} can shift from c_A towards c_M if Joule heating increases the device temperature by tens of degrees. (c) This effect was observed in Ref. [28] wherein the peak value of v_{DW} occurs around c_M measured at room-temperature due to Joule heating. (d) μ_{DW} and (e) V_d versus pulse length in Cr(8) samples. The pulse parameters are the same as in Figure 6.2. The Co-rich devices, 27.2 % and 28.1 %, do not show an increase of μ_{DW} for increasing pulse length. Therefore the peak values of μ_{DW} past c_M observed in Figure 6.2(e) is not due to Joule heating.

the maximum velocity around c_M instead of c_A measured at room temperature, as shown in Figure 6.3(b).

To investigate whether Joule heating is responsible for the peak value of μ_{DW} past the room temperature of c_A and c_M shown in Figure 6.2(d), we conducted additional experiments to measure μ_{DW} and V_d as a function of pulse length in both Co-rich and Gd-rich samples. If Joule heating is the cause, we would expect to see an increase in the DW velocity with an increase in pulse length in Co-rich samples, and a constant decrease in Gd-rich samples.

However, the results shown in Figure 6.3(d,e) reveal that longer pulses reduce both μ_{DW} and the depinning threshold. While the decrease of tte depinning threshold can be attributed larger thermal activation reducing the pinning barrier, the monotonic decrease of μ_{DW} in both Co-rich and Gd-rich samples as the pulse length increases indicate that the shift of μ_{DW} past c_M is not due to Joule heating. The reason behind that reducing in μ_{DW} is not well understood yet. For instance, similar behavior was observed in Pt(5)/GdFeCo(20) [31], where longer pulses decreased the DW velocity

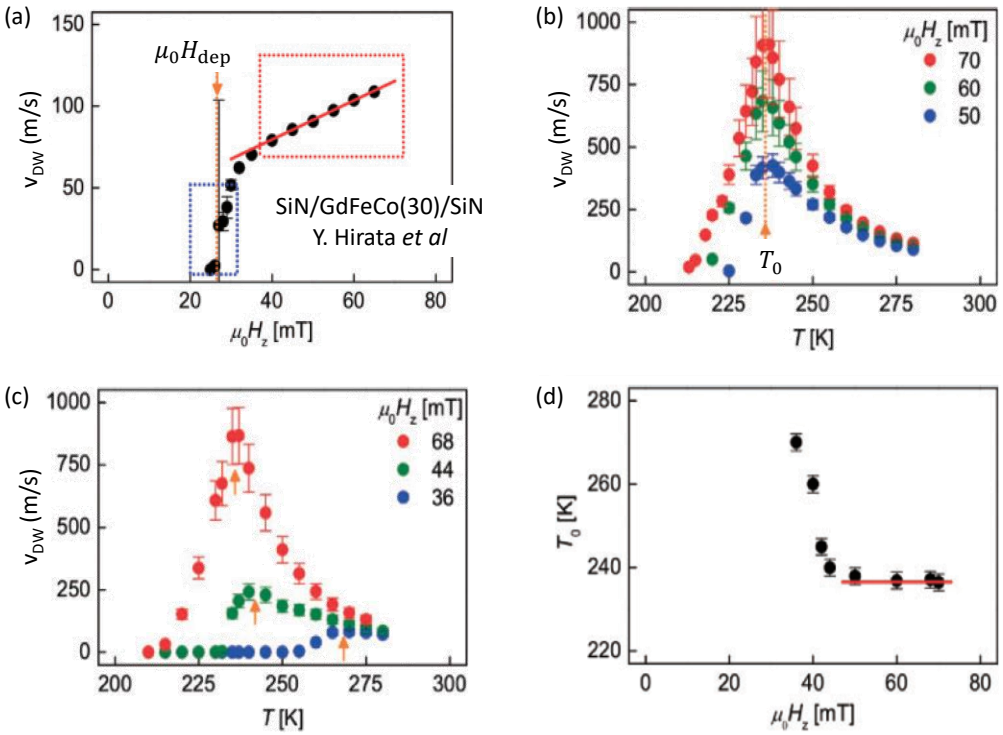

Figure 6.4: Field driven domain wall velocity SiN/$Gd_{23.5}Fe_{66.9}$ $Co_{9.6}$(100 nm)/SiN with perpendicular anisotropy taken from [260]. (a) v_{DW} as a function of $\mu_0 H_z$ at T = 280 K. The blue and red boxes represent the depinning and flow regimes, respectively. The red line represents the best linear fit. The orange arrow indicates the depinning field $\mu_0 H_{dep}$. (b) v_{DW} as a function of T for $\mu_0 H_z$ = 50, 60, and 70 mT in the linear flow regime, and (c) for T for = 36, 44, and 68 mT in the depinning regime. The temperature at which the velocity is maximal is indicated by T_0. (d) T_0 as a function of $\mu_0 H_z$. The maximum velocity is constantly around T_A in the flow regime but diverge in the depinning regime.

by more than 50%. The effect in that case was attributed to a temperature gradient between the center of the racetrack (hot) and the edges (cold) that rounded the DW shape and reduced the DW velocity. However, in our samples, the DW shape is deformed due to pinning [see in Figure 6.2(b)], which randomizes the DW tilt across the racetrack width and prevents the observation of the rounding of the DW shape.

DW mobility in the depinning regime

Pinning is another important parameter to take into account when studying the DW mobility as a function of composition. The LLG equation predicts that the DW maximum velocity is around c_A, but this only applies to a pinning-free system where the DW moves steadily with a constant tilt angle along the racetrack. This refers to

the linear flow regime, where the DW velocity is directly proportional to the applied current density [109]. However, in practice, pinning affects the DW shape and causes deformations, resulting in a continuously changing relative angle between the spin-polarized current and the DW magnetization decreasing the DW velocity.

In our experiment, the linear flow regime is most probably never reached. The presence of pinning is evident in the Kerr images [see in Figure 6.2(b)] where the DW shape is sometimes distorted. Furthermore, the data of the DW velocity versus pulse amplitude cannot be fitted with a linear fit without an offset, indicating that a linear flow regime is never achieved. We believe that the maximum DW mobility does not occurs around c_{A} because pinning hinders the intrinsic DW dynamics in the depinning regime.

To support our claims, we compare our findings with a study that examined field-driven DW motion in SiN/GdFeCo/SiN. In Ref.[260], the authors measured the temperature at which the DW velocity was maximal, which is typically attributed to the angular compensation temperature T_{A}. As shown in Figure 6.4, they found that in the flow regime, the DW velocity exhibits a peak at T_{A}, whereas in the depinning regime, the temperature corresponding to the peak DW velocity increass monotonically as the driving field $\mu_0 H_{\mathrm{z}}$ decreases, making it impossible to determine T_{A}. It is therefore likely that our current-driven DW measurements show maximum mobility around c_{M} instead of c_{A} because we never reached the linear flow regime.

Depinning threshold and Gd composition

One could argue that pinning is a stochastic process that eventually averages out and simply decreases the current-induced DW velocity independently of the composition of the ferrimagnets. Therefore, one should still observe a consistent maximum velocity around c_{A}, and maybe a shift towards c_{M} due to Joule heating. However, in Figure 6.2(f), we observe that the depinning threshold depends on the CoGd composition, with a decrease in V_d as the Gd content increases. A similar behavior was observed in current-driven DW motion in Pt/CoTb alloys, where the depinning current density gradually decreased with increasing Tb content [259], but no specific physical meaning was provided.

Another study that used field-driven DW motion in SiN/GdFeCo/SiN reported a correlation between the composition and the depinning field [260]. It was found that the depinning field $\mu_0 H_{\mathrm{dep}}$ is intrinsically related to temperature, not because of thermal activation, but because $\mu_0 H_{\mathrm{dep}}$ is related to the effective magnetic anisotropy $\mu_0 H_{\mathrm{K}}$ and magnetization M_{S} via $\mu_0 H_{\mathrm{dep}} \propto \sqrt{\mu_0 H_{\mathrm{K}}/M_{\mathrm{S}}}$, and both H_{K} and M_{S}

depend on temperature. Since there is interdependence between temperature and composition in ferrimagnets, i.e., changing the temperature is equivalent to changing the composition within a reasonable range, we argue that the threshold V_{p} depends on the Gd composition because of the ratio $H_{\mathrm{K}}/M_{\mathrm{S}}$ varies. To check this we will need to conduct additional SQUID measurements to measure H_{K} in Cr(1) and Cr(8).

Overall, the dominance of pinning over intrinsic DW dynamics, combined with the fact that the pinning barrier depends on the sample and composition, provides a plausible explanation for why the maximum values of μ_{DW} are not found around c_{A} in Figure 6.2(e).

6.5 Conclusions

In conclusion, we presente a comparative analysis of magnetic properties using SQUID and transport measurements, as well as current-induced DW motion in Pt/CoGd/Cr samples. We investigate the influence of Gd composition and Cr thickness on current-induced DW motion. The measured DW velocities are in the range of several hundred meters per second, which is comparable to previous values found in Pt/CoGd [250] under zero external field. The DW mobility is larger in Cr(8) compared to Cr(1), suggesting the presence of additional orbital torques from the Cr top layer. Unexpectedly, we observe that the maximum DW mobility shifts from c_{A} towards c_{M} in Cr(1) and Cr(8). We rule out Joule heating as the primary reason for this shift, because of the monotic decrease of the DW mobility when increasing the pulse length in both Co-rich and Gd-rich samples. We then attribute the maximum mobility close to c_{M} to the presence of pinning that dominates over the intrinsic DW magnetization dynamics of a ferrimagnet, in agreement with a previous report on field-driven DW motion [260].

Our study emphasizes the importance of considering Gd composition and Cr layers in the design of spintronic devices based on Pt/CoGd/Cr thin films. Further research is needed to fully understand the underlying mechanisms of the torques generated by the Cr layer and their impact on DW dynamics. We discuss in Chapter 7 the outlook of this research.

7 Conclusions and outlook

In this thesis, we presented a series of studies of the effects of an electric current on magnetic systems incorporating antiferromagnetic interactions. These include collinear antiferromagnets as in NiO/Pt bilayers, exchange bias in Cr_2O_3/Co/Pt trilayers, and ferrimagnetic Pt/CoGd/Cr trilayers. Our results clarify the origin of current-induced resistance effects in NiO/Pt, which we attribute to structural modification of the Pt layer rather than magnetic switching of NiO. Further, we studied field- and current-induced domain wall motion in ferromagnetic layers coupled to an antiferromagnet. Finally, we investigated current-induced domain wall motion in a ferrimagnetic layer with varying composition of the antiferromagnetically-coupled sublattices. Overall, our findings provide a systematic overview of various aspects of spintronics and pave the way for future research and development of spintronic devices including antiferromagnetically-coupled materials. In the following, we summarize the main findings and give an outlook on future studies.

In Chapter 4, we

- compared current-induced resistance variations in Pt and NiO/Pt samples.
- systematically studied the pulse amplitude and pulse length dependence of the transverse resistance on epitaxial and non-epitaxial films.
- found that changes in Pt resistivity at the corners of the Hall crosses due to current crowding effect were responsible for the resistance changes.
- observed that the signal shape cannot be used to unambiguously identify magnetic switching.
- identified competing effects responsible for the resistance changes: decrease of local resistivity due to thermal annealing of the Pt layer and increase of resistivity due to electromigration preceding device breakdown.
- showed that the substrate plays an essential role in dissipating heat away from the Pt line during pulsing.

In Chapter 5, we

- investigated the effect of exchange bias on the field- and current-driven DW motion of an AFM/FM/HM trilayer.
- found that the exchange bias field in Cr_2O_3/Co/Pt can be set either OOP or IP depending on the field cooling direction, while the Co magnetization remains OOP.
- discovered that an IP exchange bias field significantly offsets the depinning threshold of the DW, leading to a manifold increase/decrease of the DW velocity when the exchange bias field is set along/antiparallel to the DW magnetization.
- found that the IP exchange bias field adds to the effective DMI field and external IP field to determine the DW motion driven by an OOP field or spin-orbit torques.
- showed that exchange bias can be used to replace an external field to set a preferential direction of field-driven and current-driven DW motion in perpendicular AFM/FM/HM systems.

In Chapter 6, we

- conducted a comparative analysis of magnetic properties using SQUID and transport measurements, as well as current-induced DW motion in Pt/CoGd/Cr samples.
- observed that the actual Gd content in the CoGd layer tends to be lower than the nominal deposition rate.
- found that Cr(8) exhibits larger mobility than Cr(1), suggesting the presence of additional orbital torques from the Cr top layer.
- evidenced that the maximum DW mobility shifts from c_A towards c_M in Cr(1) and Cr(8), and attributed this to the presence of pinning that dominates over the intrinsic DW magnetization dynamics effect.
- called for further transport measurements to quantify the effective torques acting on the CoGd layer to confirm whether Cr(8) indeed has larger torques than Cr(1) in relation to DW mobility.

Based on Chapter 6, various intriguing behaviors emerged. In the following, we propose several projects to expand this work:

Nitrification of Gd. Our initial results indicate the presence of interdiffusion of Gd across a 1 nm-thick Cr layer, alloying with the SiN capping layer. As a first step, I

propose to remove the top SiN layer to assess if it actually reduces oxidation from the environment and is beneficial in maintaining the effective Gd composition close the nominal deposited Gd composition.

As a second project, I propose modifying the sample structure by inserting a Pt interlayer between the CoGd and Cr layers to form Pt/CoGd/Pt/Cr. In addition to reducing interdiffusion of Gd across the thin Cr layer, the Pt interlayer can serve several purposes. Firstly, the spin current of the top layer will subtract from the Pt bottom layer, eventually canceling out if the Pt layers have similar thicknesses [103]. By optimizing the Pt thickness to achieve both strong perpendicular anisotropy and cancellation of spin currents, we can amplify the effect of the orbital current from the Cr layer. However, the Pt/CoGd/Pt system favors the presence of Bloch-type domain walls [103], which require an in-plane external magnetic field along the current direction to transform the domain walls into a Néel-type, enabling current-induced domain wall motion.

Secondly, Pt has a large spin-orbit coupling and can convert the orbital current from Cr into a spin current into CoGd [118]. By changing the Gd content while keeping the Pt thicknesses constant, one can differentiate whether the orbital current is converted by the Gd in the CoGd layer or by the Pt interlayer.

Influence of pinning. We observed that the [Co/Gd] multilayer possesses substantial pinning, which hinders the extraction of intrinsic DW dynamics. Therefore, I propose to replace the [Co/Gd] multilayers with a CoGd alloy using co-sputtering of Co and Gd. The co-sputtered CoGd layers might have less pinning due to better homogeneity.

In addition, we observed pinning at the edges of the devices. I propose to investigate whether patterning the devices using reactive ion etching, instead of lift-off techniques, reduces pinning at the edges. However, etching Cr layers is typically inefficient and requires high etching power, which may not be feasible. Furthermore, the Gd composition can be altered due to temperature changes during etching, so the etching power should be minimized.

By changing the [Co/Gd] multilayers to co-sputtered CoGd alloy and adapting the device fabrication process, one could reduce pinning and approach the linear flow regime, taking advantage of the fast DW dynamics at the compensation composition.

Separation of the orbital torque. We have observed a more than 20% increase in current-induced domain wall mobility in 8 nm-thick Cr samples compared to 1 nm-thick Cr samples, indicating the presence of additional orbital torques from

the Cr top layer. To distinguish between the generation of orbital torque and spin torque, I propose to investigate the current-induced torque generation using other light metals with large orbital Hall conductivity, such as Al [261, 262] and oxidized Cu [249]. By comparing the effective domain wall mobility with the values of the orbital Hall conductivity of the light metal, one can infer the role of orbital torque. Furthermore, the sign of the orbital Hall conductivity in Al is opposite to that of Cr and oxidized Cu. In the hypothetical case of large orbital torques dominating over the spin torque from the bottom Pt layer, the direction of the domain wall motion with respect to the electric current direction would therefore be opposite in Al samples compared to Cr and CuO samples.

8 Appendix

8.1 Matlab code for the computation of the domain wall velocity

```
% It is a Matlab file to measure the magnetic domain wall velocity. After
% indicating the folder and filename, the users will be ask to manually
% selected the left and right side of the domain wall displacement. xDWmax
% correspond to the interval length, and xDWmean is computed as the
% sum of the pixel inside the interval (defined by the user) devided by the
% racetrack width. Then, the distance in pixels is converted into meters by
% multiplying by the scale.

% Below we give a first example.
clear all

% to import the MOKE images
% here is an example
folderName = uigetdir;
if folderName == 0
    disp('No folder selected, please try again.')
else
    disp(['Selected folder: ', folderName])
end
prefix = 'l11'
%% Load the files
S = dir(folderName);
S = S(~[S.isdir]);            % remove if not a file
[~,idx] = sort([S.datenum]); % sort by modified data, oldest to the newest
Ssort = S(idx); %
% remove the non corresponding the hear
fileNameAll = struct;
fileNameSelect = struct;
```

```
% filters the fileName keep only the files with the corresponding prefix
% and remove files and matrices that don't contain any measurements

% what the filename must contain. For instance, posEBx, posHx16000e, etc
txt1 = 'subtracted';
txt2 = '-';
txt3 = '-';
% txt1 = '.';txt2 = '.';txt3 = '.';
for n = 1 : numel(Ssort)
    if strncmp(Ssort(n).name, prefix, length(prefix))
        fileNameAll(end+1).name = Ssort(n).name;
        if strfind( fileNameAll(end).name, txt1)
            if strfind( fileNameAll(end).name, txt2)
                if strfind( fileNameAll(end).name, txt3)
                    fileNameSelect(end+1).name = Ssort(n).name;
                end
            end
        end
    end
end
fileNameAll = fileNameAll(2:end); fileNameSelect = fileNameSelect(2:end);

if size(fileNameSelect, 2) == 0
    disp('There is no such file in this folder');
end
results    = zeros(1,12);

ContrThr   = 0.1;         % below/above the contrast level is black/white
RacetrackHeigth    = 38;  % in pixels
scaleImage = 260e-6/2048; % scale of the image
xDWmean = 1; xDWmax  = 1; dY = 1;
%% indicate the center of the racetrack
% it will crop the raw image according the coordinate below
% zoomIn     = [880, 1180, 1180, 1250];
zoomIn  = f_checkcentering( folderName, fileNameSelect(1).name, ContrThr)
%zoomIn     = [880, 1180, 1180, 1250];
for n =  20 :25%numel(fileNameSelect)
    pause(0.2);
    % open and ask to click on the left and right side of the DW expansion
%     [xDWmean, xDWmax]  = f_DW_Width_Manual( folderName, ...
%                                             fileNameSelect(n).name,...
```

```
70  %                                                   ContrThr,...
71  %                                                   RacetrackHeigth,...
72  %                                                   zoomIn);
73      [xDWmean, xDWmax]     = f_DW_Width_Auto( folderName, ...
74                                                fileNameSelect(n).name
                                                      ,...
75                                                ContrThr,...
76                                                RacetrackHeigth,...
77                                                zoomIn);
78      % read the experimental parameters
79      % Get pulse amplitude
80      PAmp = char(extractBefore(fileNameSelect(n).name, 'V-'));
81      if isempty(PAmp)
82          PAmp = char(extractBefore(fileNameSelect(n).name, 'V-10Hz')
                );
83      end
84      if strcmp( PAmp(end-4:end-2), 'pos')
85          PAmp = str2double(PAmp(end-1:end));
86      elseif strcmp( PAmp(end-4:end-2), 'neg')
87          PAmp = -str2double(PAmp(end-1:end));
88          xDWmean    = -xDWmean; xDWmax    = -xDWmax;
89      end
90      % Get the parameters from the filename
91      % Get pulse length
92      try
93          PulseLeng = char(extractBefore(fileNameSelect(n).name, 'ns'
                ));
94          lastdot_pos = find( PulseLeng == '-', 1, 'last');
95          PulseLeng = str2double(PulseLeng( lastdot_pos+1:end))*1e-9;
96      catch
97          disp('problem reading pulse length');
98      end
99      if isempty(PulseLeng)
100         PulseLeng = char(extractBefore(fileNameSelect(n).name, 'ps'
                ));
101         lastdot_pos = find( PulseLeng == '-', 1, 'last');
102         PulseLeng = str2double(PulseLeng( lastdot_pos+1:end))*1e
                -12;
103     end
104     % Get the field value
105     HIP = char(extractBefore(fileNameSelect(n).name, 'A-'));
106     if isempty(HIP)
107         HIP = char(extractBefore(fileNameSelect(n).name, '0e-'));
108     else
109         HIP = 'posHx00';
110     end
111     if strfind( HIP, 'posHx')
112         HIP =  str2double(extractAfter(HIP, '-posHx'));
```

```
113     elseif strfind( HIP, 'negHx')
114         HIP = -str2double(extractAfter(HIP, '-negHx'));
115     end
116     % Get number of pulse
117     PulseNb = char(extractBefore(fileNameSelect(n).name, 'pls'));
118     PulseNb = str2double(extractAfter( PulseNb, 'A-'));
119     if isnan(PulseNb)
120         PulseNb = char(extractBefore(fileNameSelect(n).name, 'pls')
            );
121         PulseNb = str2double(extractAfter( PulseNb, '0e-'));
122     end
123
124     % Compute velocity dx/(Number * dt) [pixel/s]
125     DWvelMean = xDWmean/(PulseNb*PulseLeng)*scaleImage;
126     DWvelMax  = xDWmax /(PulseNb*PulseLeng)*scaleImage;
127
128     % Store the results
129     SaveVec = [ n, PulseLeng, PAmp, NaN, HIP, PulseNb, xDWmean,
            xDWmean*scaleImage, DWvelMean, xDWmax, xDWmax*scaleImage,
            DWvelMax, atand(-xDWmean/dY)];
130     results( n, :) =  SaveVec( 2:end);
131 end
132 %% average the datas with same parameter
133 col = 2; % Pulse amplitude
134 [i,idx]= sort( results( :, col),'ascend');
135 resultsReorder = results( idx, :);
136 resultsMeanPulse = f_avgVelocity( resultsReorder, col);
137
138 col = 4; % IP field
139 [i,idx]= sort( results( :, col),'ascend');
140 resultsReorder = results( idx, :);
141 resultsMeanField = f_avgVelocity( resultsReorder, col);
142 %% Functions
143 function [xDWmean, xDWmax] = f_DW_Width_Manual( folderName, prefix,
        ContrThr, RacetrackHeigth, zoomIn)
144     % read the image
145     I = imread( [ folderName, '/', prefix]);
146     Iresize = I;
147
148     % convert RGB to Gray
149     if ndims( Iresize) == 3
150         Iresize= rgb2gray( Iresize);
151     end
152     % convert [ 0, 256] scale to [ 0, 1] scale
153     Iresize= im2double( Iresize);
154
155     % resize/crop the image, [x1, x2, y1, y2] crop box that need to
            be keepts
```

```
156     if sum(zoomIn) > 0
157         Iresize = Iresize( zoomIn(2):zoomIn(4),zoomIn(1):zoomIn(3))
                ;
158     end
159
160     % Adapt contrast
161     Iresize = Iresize >= ContrThr;
162     imshow(Iresize);
163
164     title(prefix);
165     % to read contiously the mouse position
166     %     set (gcf, 'WindowButtonMotionFcn', @mouseMove);
167
168     % use mouse button do define one edge of the DW
169     M1 = ginput(1);
170     % draw lines to show where the point was selectd
171     xline( M1(1), 'Color', 'b', 'LineStyle','--', 'Linewidth', 2);
172     yline( M1(2), 'Color', 'b', 'LineStyle','--', 'Linewidth', 2);
173
174     % use mouse button do define the other edge of the DW
175     M2 = ginput(1);
176     if M2(1) > size(Iresize, 2)
177         M2(1) = size(Iresize, 2);
178     end
179     if M2(1) < 1
180         M2(1) = 1;
181     end
182
183     xline( M2(1), 'Color', 'b', 'LineStyle','--', 'Linewidth', 2);
184
185     %Total length between the two point in pixels
186     xDWmax = (M2(1)-M1(1)); % 1D Vector
187     %dY = -(M2(2)-M1(2)); % 2D Vector
188     %dL = norm(M2-M1); % 2D Vector
189
190     %%%%%%%%  method B %%%%%%%%
191     % It gives the averrage DW travelling distance.
192     % sum up all the pixel where there is contrast inside the
            interval
193     % defined by the user and devide by the width of the bar.
194     DWarea    = sum( sum( Iresize ( :, min( M1(1), M2(1)) : max( M1
            (1), M2(1)))));
195     % Hallbar width = 74 - 38 pixels = 36 pixels
196     xDWmean = DWarea/RacetrackHeigth;
197
198     xline( min( M1(1), M2(1)), 'Color', 'b', 'LineStyle','--', '
            Linewidth', 2);
```

```
199     xline( min( M1(1), M2(1)) + abs(xDWmean), 'Color', 'b', '
            LineStyle','--', 'Linewidth', 2);
200 end
201 function [ xDWmean, xDWmax] = f_DW_Width_Auto( folderName, prefix,
        ContrThr, RacetrackHeigth, zoomIn)
202     % ContThr is the contrast threshold
203     % RacetrackHeigth is the height of the bar in pixel
204     % ZoomIn is the number of the pixel that is cropped away from
            the
205     % center of the image
206
207     % read the image
208     I = imread( [ folderName, '/', prefix]);
209     % make a copy
210     Iprocessed = I;
211     % convert RGB to Gray
212     if ndims( Iprocessed) == 3
213         Iprocessed = rgb2gray( Iprocessed);
214     end
215
216     % convert [ 0, 256] scale to [ 0, 1] scale
217     Iprocessed = im2double( Iprocessed);
218
219     % Sometimes there is a white border around the image. To do so
            we
220     % remove all the lines and columns of the images that contains
            only
221     % ones
222     % check vertical lines
223     col=find(sum(Iprocessed)<size(Iprocessed,1));
224     Iprocessed = Iprocessed(:, col);
225     row=find(sum(Iprocessed')<size(Iprocessed,2));
226     Iprocessed = Iprocessed(row, :);
227
228     % to rotate by 90 degrees anticlockwise
229     % rot90(A,k) rotates array A counterclockwise by k*90 degrees
230     if size( Iprocessed,1) > size( Iprocessed,2)
231         Iprocessed  = rot90( Iprocessed , 1);
232     end
233
234     % resize/crop the image, [x1, x2, y1, y2] crop box that need to
            be keepts
235     if sum(zoomIn) > 0
236         Iprocessed  = Iprocessed ( zoomIn(2):zoomIn(4),zoomIn(1):
                zoomIn(3));
237         Xcent = round(abs(zoomIn(2)-zoomIn(4))/2);
238     end
239
```

```
240     % create a logical matrix
241     Ilogic = Iprocessed >= ContrThr;
242 %     spy(Ilogic);
243     % show the image
244     imshow( Ilogic); title(prefix);
245     % compute DW length with 2 methodes
246
247     %%%%%%%%  method A %%%%%%%
248     % find the longest travel distance by looking at the
249     %  horizontal histogram of the image and getting the longest
            line of
250     %  contrast
251     % first sum pixels in each row,
252     Isum = sum(Ilogic');
253     % then find the k largest elements
254     [ val, loc ] = maxk( Isum, 3);
255     % average DW length
256     xDWmax = round(mean(val));
257     % average location;
258     DWloc = round(mean( loc));
259     % draw the line where there is the wall. compute the moving
            mean to
260     % find the plateau at which there is the wall.
261     xStartMax = find ( movmean(Ilogic( DWloc, :),3) == 1 ,1, 'first
            ');
262     if isempty(xStartMax)
263         xStartMax = 1;
264     end
265     % but sometimes, there is noise and a fake xDWmax and xStart is
            found
266     % to change that, we compute the ratio of the white/black pixel
            along
267     % that line. if it is too big, we look of a new maximum... not
268     % implemented yet
269
270     xline( xStartMax, 'Color', 'r', 'LineStyle','--', 'Linewidth',
            2);
271     xline( xStartMax + xDWmax, 'Color', 'r', 'LineStyle','--', '
            Linewidth', 2);
272     yline( DWloc, 'Color', 'r', 'LineStyle','--', 'Linewidth', 2);
273
274     %%%%%%%%  method B %%%%%%%%
275     % sum up all the pixel where there is contrast and devide
276     % by the width of the bar. It gives the averrage DW travelling
            distance
277     % from Methode A, we know does the DW starts and it avg length,
            which
```

```
278     % over evaluate the total displacement. Hence. we can simply
            sum the
279     % pixel in the box define by these two values.
280     if xStartMax + xDWmax > length( Ilogic)
281         xDWmax = length( Ilogic) - xStartMax;
282     end
283     DWarea    = sum( sum( Ilogic ( :, xStartMax : xStartMax + xDWmax
            )));
284     % Hallbar width = 74 - 38 pixels = 36 pixels
285     xDWmean = DWarea/RacetrackHeigth;
286
287     % draw the line where there is the wall. compute the moving
            mean to
288     % find the plateau at which there is the wall.
289     xStartMax = find ( movmean(Ilogic( DWloc, :),3) == 1 ,1, 'first
            ');
290     if isempty(xStartMax)
291         xStartMax = 1;
292     end
293     xline( xStartMax, 'Color', 'b', 'LineStyle','--', 'Linewidth',
            2);
294     xline( xStartMax + xDWmean, 'Color', 'b', 'LineStyle','--', '
            Linewidth', 2);
295
296
297 end
298 function [CropParam] = f_checkcentering( folderName, prefix,
        ContrThr)
299        % read the image
300     I = imread( [ folderName, '/', prefix]);
301     Iresize = I;
302
303     % convert RGB to Gray
304     if ndims( Iresize) == 3
305         Iresize= rgb2gray( Iresize);
306     end
307     % convert [ 0, 256] scale to [ 0, 1] scale
308     Iresize= im2double( Iresize);
309
310     % Sometimes there is a white border around the image. To do so
            we
311     % remove all the lines and columns of the images that contains
            only
312     % ones
313     % check vertical lines
314     col=find(sum(Iresize)<size(Iresize,1));
315     Iresize = Iresize(:, col);
316     row=find(sum(Iresize')<size(Iresize,2));
```

```
317     Iresize = Iresize(row, :);
318     % to rotate by 90? anticlockwise
319     % rot90(A,k) rotates array A counterclockwise by k*90 degrees
320     if size( Iresize,1) > size( Iresize,2)
321         Iresize  = rot90( Iresize, 1);
322     end
323     % Adapt contrast
324     Iresize = Iresize >= ContrThr;
325     % resize/crop the image
326 %     Iresize = I( size( I, 1)/2-zoomIn : size( I, 1)/2+zoomIn,
    size( I, 1)/2-zoomIn : size( I, 1)/2+zoomIn);
327     imshow(Iresize);
328
329     title(prefix);
330     % to read contiously the mouse position
331     %     set (gcf, 'WindowButtonMotionFcn', @mouseMove);
332
333     % use mouse button do define one edge of the DW
334
335     M1 = ginput(1);
336     CropParam( 1:2 ) = round(M1);
337     % draw lines to show where the point was selectd
338     xline( M1(1), 'Color', 'b', 'LineStyle','--', 'Linewidth', 2);
339     yline( M1(2), 'Color', 'b', 'LineStyle','--', 'Linewidth', 2);
340
341     % use mouse button do define the other edge of the DW
342     M2 = ginput(1);
343     CropParam( 3:4 ) = round(M2);
344     xline( M2(1), 'Color', 'b', 'LineStyle','--', 'Linewidth', 2);
345
346 end
347 function results = f_avgVelocity( x, colmean)
348
349     % average the value with common parameter
350     % colmean = 2 is the pulse amplitude
351     % colmean = 4 is the external field
352
353     if nargin == 1
354         col = 4;
355     else
356         col = colmean;
357     end
358
359     [UniVal] = unique(x( :, col));
360
361     results = zeros( length(UniVal), 5);
362     for n = 1 : length( UniVal)
363         % avg the row with indentical parameter
```

```
364         meanVal = mean( x( x( :, col) == UniVal(n), :), 1);
365         error   = std(  x( x( :, col) == UniVal(n), :), 1);
366         if isnan(error)
367             error = 0.5*ones(size(meanVal));
368         end
369         results( n, :) = [meanVal(col), meanVal(8), error(8),
                meanVal(11), error(11)];
370     end
371 end
372 % to read continously the mouse position when manually selecting
        the DW
373 % position.
374 function mouseMove(object, eventdata)
375     C = get (gca, 'CurrentPoint');
376     title(gca, ['(X,Y) = (', num2str(C(1,1)), ', ',num2str(C(1,2)),
            ')']);
377 end
```

Bibliography

[1] D. Sander, S. O. Valenzuela, D. Makarov, et al. “The 2017 Magnetism Roadmap”. In: *Journal of Physics D: Applied Physics* 50.36 (Sept. 2017), p. 363001. DOI: 10.1088/1361-6463/aa81a1 (cit. on p. 1).

[2] E. Y. Vedmedenko, R. K. Kawakami, D. D. Sheka, et al. “The 2020 magnetism roadmap”. In: *Journal of Physics D: Applied Physics* 53.45 (Nov. 2020), p. 453001. DOI: 10.1088/1361-6463/ab9d98 (cit. on p. 1).

[3] Louis Néel. “Théorie du paramagnétisme constant. Application au manganèse.” In: *Comptes Rendus Hebdomadaires Des Seances De L Academie Des Sciences* 203 (1936), pp. 304–306 (cit. on p. 1).

[4] Louis Néel. “Influence des fluctuations du champ moléculaire sur les propriétés magnétiques des corps”. In: *Annales de Physique* 10.18 (Apr. 1932), pp. 5–105. DOI: 10.1051/anphys/193210180005 (cit. on p. 1).

[5] Louis Néel. “Propriétés magnétiques de l’état métallique et énergie d’interaction entre atomes magnétiques”. In: *Annales de physique* 11.5 (Apr. 1936), pp. 232–279. DOI: 10.1051/anphys/193611050232 (cit. on p. 1).

[6] V. Baltz, A. Manchon, M. Tsoi, et al. “Antiferromagnetic spintronics”. In: *Reviews of Modern Physics* 90.1 (Feb. 2018), p. 015005. DOI: 10.1103/RevModPhys.90.015005 (cit. on pp. 1, 2, 7, 18, 40).

[7] K. Olejník, V. Schuler, X. Marti, et al. “Antiferromagnetic CuMnAs multi-level memory cell with microelectronic compatibility”. In: *Nature Communications* 8.1 (Aug. 2017), p. 15434. DOI: 10.1038/ncomms15434 (cit. on pp. 1, 2, 40).

[8] Kamil Olejník, Tom Seifert, Zdeněk Kašpar, et al. “Terahertz electrical writing speed in an antiferromagnetic memory”. In: *Science Advances* 4.3 (Mar. 2018), eaar3566. DOI: 10.1126/sciadv.aar3566 (cit. on pp. 1, 2, 40, 42).

[9] F. Keffer and C. Kittel. “Theory of Antiferromagnetic Resonance”. In: *Physical Review* 85.2 (Jan. 1952), pp. 329–337. DOI: 10.1103/PhysRev.85.329 (cit. on pp. 2, 40).

[10] C. G. Shull, W. A. Strauser, and E. O. Wollan. “Neutron diffraction by paramagnetic and antiferromagnetic substances”. In: *Physical Review* 83.2 (1951), pp. 333–345. DOI: 10.1103/PhysRev.83.333 (cit. on p. 2).

[11] J. Stöhr, A. Scholl, T. J. Regan, et al. “Images of the Antiferromagnetic Structure of a NiO(100) Surface by Means of X-Ray Magnetic Linear Dichroism Spectromicroscopy”. In: *Physical Review Letters* 83.9 (Aug. 1999), pp. 1862–1865. DOI: 10.1103/PhysRevLett.83.1862 (cit. on p. 2).

[12] Takahiro Moriyama, Kent Oda, Takuo Ohkochi, Motoi Kimata, and Teruo Ono. “Spin torque control of antiferromagnetic moments in NiO”. In: *Scientific Reports* 8.1 (Dec. 2018), p. 14167. DOI: 10.1038/s41598-018-32508-w (cit. on pp. 2, 22, 40–42, 47, 58).

[13] L. Baldrati, O. Gomonay, A. Ross, et al. “Mechanism of Néel Order Switching in Antiferromagnetic Thin Films Revealed by Magnetotransport and Direct Imaging”. In: *Physical Review Letters* 123.17 (Oct. 2019), p. 177201. DOI: 10.1103/PhysRevLett.123.177201 (cit. on pp. 2, 22, 40–42, 47, 58).

[14] Manfred Fiebig, D. Fröhlich, Th Lottermoser, et al. “Second Harmonic Generation in the Centrosymmetric Antiferromagnet NiO”. In: *Physical Review Letters* 87.13 (Sept. 2001), p. 137202. DOI: 10.1103/PhysRevLett.87.137202 (cit. on p. 2).

[15] Isaiah Gray, Takahiro Moriyama, Nikhil Sivadas, et al. “Spin Seebeck Imaging of Spin-Torque Switching in Antiferromagnetic Pt/NiO Heterostructures”. In: *Physical Review X* 9.4 (Oct. 2019), p. 041016. DOI: 10.1103/PhysRevX.9.041016 (cit. on pp. 2, 40–42).

[16] Patrick Appel, Brendan J. Shields, Tobias Kosub, et al. “Nanomagnetism of Magnetoelectric Granular Thin-Film Antiferromagnets”. In: *Nano Letters* 19.3 (Mar. 2019), pp. 1682–1687. DOI: 10.1021/acs.nanolett.8b04681 (cit. on p. 2).

[17] Martin S. Wörnle, M. S. Woernle, P. Welter, et al. “Current-induced fragmentation of antiferromagnetic domains”. In: *arXiv* (Dec. 2019), pp. 1–21 (cit. on pp. 2, 40).

[18] Martin S. Wörnle, P. Welter, M. Giraldo, et al. “Coexistence of Bloch and Néel walls in a collinear antiferromagnet”. In: *Physical Review B* 103.9 (Mar. 2021), p. 094426. DOI: 10.1103/PhysRevB.103.094426 (cit. on pp. 2, 12).

[19] Johanna Fischer, Olena Gomonay, Richard Schlitz, et al. “Spin Hall magnetoresistance in antiferromagnet/heavy-metal heterostructures”. In: *Physical Review B* 97.1 (Jan. 2018), p. 014417. DOI: 10.1103/PhysRevB.97.014417 (cit. on pp. 2, 7, 8, 43).

[20] Richard Schlitz, Tobias Kosub, Andy Thomas, et al. “Evolution of the spin hall magnetoresistance in Cr2O3 /Pt bilayers close to the Néel temperature”. In: *Applied Physics Letters* 112.13 (Mar. 2018), p. 132401. DOI: 10.1063/1.5019934 (cit. on pp. 2, 7).

[21] T. Jungwirth, X. Marti, P. Wadley, and J. Wunderlich. “Antiferromagnetic spintronics”. In: *Nature Nanotechnology* 11.3 (Mar. 2016), pp. 231–241. DOI: 10.1038/nnano.2016.18 (cit. on pp. 2, 40).

[22] Stuart S. P. Parkin, Masamitsu Hayashi, and Luc Thomas. “Magnetic Domain-Wall Racetrack Memory”. In: *Science* 320.5873 (Apr. 2008), pp. 190–194. DOI: 10.1126/science.1145799 (cit. on pp. 3, 62).

[23] C. Battarel, R. Morille, and J. Nori. “Flat domain propagation mechanism in a simplified shift register structure with magnetostrictive read out”. In: *IEEE Transactions on Magnetics* 13.5 (Sept. 1977), pp. 1302–1304. DOI: 10.1109/TMAG.1977.1059534 (cit. on pp. 3, 62).

[24] J. H. Franken, H. J.M. Swagten, and B. Koopmans. “Shift registers based on magnetic domain wall ratchets with perpendicular anisotropy”. In: *Nature Nanotechnology* 7.8 (2012), pp. 499–503. DOI: 10.1038/nnano.2012.111 (cit. on pp. 3, 62).

[25] Mathias Kläui, C. A.F. Vaz, J. A.C. Bland, et al. “Controlled and reproducible domain wall displacement by current pulses injected into ferromagnetic ring structures”. In: *Physical Review Letters* 94.10 (2005), pp. 1–4. DOI: 10.1103/PhysRevLett.94.106601 (cit. on pp. 3, 62).

[26] Giacomo Sala and Pietro Gambardella. “Ferrimagnetic Dynamics Induced by Spin-Orbit Torques”. In: *Advanced Materials Interfaces* 2201622.1 (2022). DOI: 10.1002/admi.202201622 (cit. on pp. 3, 82, 88).

[27] Joseph Finley and Luqiao Liu. “Spintronics with compensated ferrimagnets”. In: *Applied Physics Letters* 116.11 (Mar. 2020), p. 110501. DOI: 10.1063/1.5144076 (cit. on pp. 3, 82).

[28] Kaiming Cai, Zhifeng Zhu, Jong Min Lee, et al. “Ultrafast and energy-efficient spin–orbit torque switching in compensated ferrimagnets”. In: *Nature Electronics* 3.1 (2020), pp. 37–42. DOI: 10.1038/s41928-019-0345-8 (cit. on pp. 3, 18, 82, 83, 87–91).

[29] Kab Jin Kim, Se Kwon Kim, Yuushou Hirata, et al. “Fast domain wall motion in the vicinity of the angular momentum compensation temperature of ferrimagnets”. In: *Nature Materials* 16.12 (2017), pp. 1187–1192. DOI: 10.1038/nmat4990 (cit. on pp. 3, 87).

[30] Se Kwon Kim, Geoffrey S. D. Beach, Kyung-Jin Lee, et al. “Ferrimagnetic spintronics”. In: *Nature Materials* 21.1 (Jan. 2022), pp. 24–34. DOI: 10.1038/s41563-021-01139-4 (cit. on pp. 3, 18, 82).

[31] S. Ranjbar, S. Kambe, S. Sumi, et al. “Elucidation of the mechanism for maintaining ultrafast domain wall mobility over a wide temperature range”. In: *Materials Advances* 3.18 (2022), pp. 7028–7036. DOI: 10.1039/d2ma00273f (cit. on pp. 3, 82, 90, 91).

[32] Se Kwon Kim, Kyung-Jin Lee, and Yaroslav Tserkovnyak. “Self-focusing skyrmion racetracks in ferrimagnets”. In: *Physical Review B* 95.14 (Apr. 2017), p. 140404. DOI: 10.1103/PhysRevB.95.140404 (cit. on pp. 3, 83).

[33] Yuushou Hirata, Duck Ho Kim, Se Kwon Kim, et al. “Vanishing skyrmion Hall effect at the angular momentum compensation temperature of a ferrimagnet”. In: *Nature Nanotechnology* 14.3 (Mar. 2019), pp. 232–236. DOI: 10.1038/s41565-018-0345-2 (cit. on pp. 3, 83).

[34] Saül Vélez, Sandra Ruiz-Gómez, Jakob Schaab, et al. “Current-driven dynamics and ratchet effect of skyrmion bubbles in a ferrimagnetic insulator”. In: *Nature Nanotechnology* 17.8 (Aug. 2022), pp. 834–841. DOI: 10.1038/s41565-022-01144-x (cit. on pp. 3, 34, 83, 131).

[35] Pingzhi Li, Thomas J. Kools, Bert Koopmans, and Reinoud Lavrijsen. “Ultrafast Racetrack Based on Compensated Co/Gd-Based Synthetic Ferrimagnet with All-Optical Switching”. In: *Advanced Electronic Materials* 9.1 (Jan. 2023), p. 2200613. DOI: 10.1002/aelm.202200613 (cit. on pp. 3, 83).

[36] J.M.D. Coey, V. Skumryev, and K. Gallagher. “Is gadolinium really ferromagnetic?” In: *Nature* 401.6748 (Sept. 1999), pp. 35–36. DOI: 10.1038/43363 (cit. on p. 5).

[37] J. M.D. Coey. *Magnetism and magnetic materials*. Vol. 9780521816. 2009 (cit. on pp. 5, 6, 11, 15, 18).

[38] W. Heisenberg. “Mehrkorperproblem und Resonanz in der Quantenmechanik”. In: *Zeitschrift fr Physik* 38.6-7 (June 1926), pp. 411–426. DOI: 10.1007/BF01397160 (cit. on p. 5).

[39] Paul Dirac. “On the theory of quantum mechanics”. In: *Proceedings of the Royal Society of London. Series A, Containing Papers of a Mathematical and Physical Character* 112.762 (Oct. 1926), pp. 661–677. DOI: 10.1098/rspa.1926.0133 (cit. on p. 5).

[40] Frances Hellman, Axel Hoffmann, Yaroslav Tserkovnyak, et al. “Interface-induced phenomena in magnetism”. In: *Reviews of Modern Physics* 89.2 (June 2017). DOI: 10.1103/RevModPhys.89.025006 (cit. on p. 6).

[41] Tôru Moriya. “Anisotropic Superexchange Interaction and Weak Ferromagnetism”. In: *Physical Review* 120.1 (Oct. 1960), pp. 91–98. DOI: 10.1103/PhysRev.120.91 (cit. on p. 7).

[42] I. Dzyaloshinsky. “A thermodynamic theory of “weak” ferromagnetism of antiferromagnetics”. In: *Journal of Physics and Chemistry of Solids* 4.4 (Jan. 1958), pp. 241–255. DOI: 10.1016/0022-3697(58)90076-3 (cit. on p. 7).

[43] Satoru Emori, Uwe Bauer, Sung-Min Ahn, Eduardo Martinez, and Geoffrey S. D. Beach. “Current-driven dynamics of chiral ferromagnetic domain walls”. In: *Nature Materials* 12.7 (July 2013), pp. 611–616. DOI: 10.1038/nmat3675 (cit. on pp. 7, 62, 63, 70–72).

[44] Kwang-Su Ryu, Luc Thomas, See-Hun Yang, and Stuart Parkin. “Chiral spin torque at magnetic domain walls”. In: *Nature Nanotechnology* 8.7 (July 2013), pp. 527–533. DOI: 10.1038/nnano.2013.102 (cit. on pp. 7, 62, 63, 70–73).

[45] Vikas Kashid, Timo Schena, Bernd Zimmermann, et al. “Dzyaloshinskii-Moriya interaction and chiral magnetism in 3d-5d zigzag chains: Tight-binding model and ab initio calculations”. In: *Physical Review B* 90.5 (Aug. 2014), p. 054412. DOI: 10.1103/PhysRevB.90.054412 (cit. on p. 7).

[46] Hongxin Yang, André Thiaville, Stanislas Rohart, Albert Fert, and Mairbek Chshiev. “Anatomy of Dzyaloshinskii-Moriya Interaction at Co/Pt Interfaces”. In: *Physical Review Letters* 115.26 (Dec. 2015), p. 267210. DOI: 10.1103/PhysRevLett.115.267210 (cit. on pp. 7, 69).

[47] André Thiaville, Stanislas Rohart, Emilie Jué, Vincent Cros, and Albert Fert. “Dynamics of Dzyaloshinskii domain walls in ultrathin magnetic films”. In: *EPL (Europhysics Letters)* 100.5 (Dec. 2012), p. 57002. DOI: 10.1209/0295-5075/100/57002 (cit. on pp. 7, 20, 21, 62, 68–70, 72, 87).

[48] P. P. J. Haazen, E. Murè, J. H. Franken, et al. “Domain wall depinning governed by the spin Hall effect”. In: *Nature Materials* 12.4 (Apr. 2013), pp. 299–303. DOI: 10.1038/nmat3553 (cit. on pp. 7, 62, 63, 70).

[49] Eduardo Martinez, Satoru Emori, Noel Perez, Luis Torres, and Geoffrey S. D. Beach. "Current-driven dynamics of Dzyaloshinskii domain walls in the presence of in-plane fields: Full micromagnetic and one-dimensional analysis". In: *Journal of Applied Physics* 115.21 (June 2014), p. 213909. DOI: 10.1063/1.4881778 (cit. on pp. 7, 20, 62, 70, 71, 73).

[50] Jia Xu, Chao Zhou, Mengwen Jia, et al. "Imaging antiferromagnetic domains in nickel oxide thin films by optical birefringence effect". In: *Physical Review B* 100.13 (Oct. 2019), p. 134413. DOI: 10.1103/PhysRevB.100.134413 (cit. on pp. 8, 13).

[51] Pengxiang Zhang, Joseph Finley, Taqiyyah Safi, and Luqiao Liu. "Quantitative Study on Current-Induced Effect in an Antiferromagnet Insulator/Pt Bilayer Film". In: *Physical Review Letters* 123.24 (2019), p. 247206. DOI: 10.1103/PhysRevLett.123.247206 (cit. on p. 8).

[52] Helen Gomonay and Vadim M. Loktev. "Magnetostriction and magnetoelastic domains in antiferromagnets". In: *Journal of Physics: Condensed Matter* 14.15 (Apr. 2002), pp. 3959–3971. DOI: 10.1088/0953-8984/14/15/310 (cit. on p. 8).

[53] J. Gelard, A.R. Fert, P. Meriel, and Y. Allain. "Magnetic structure of FeI2 by neutron diffraction experiments". In: *Solid State Communications* 14.2 (Jan. 1974), pp. 187–189. DOI: 10.1016/0038-1098(74)90213-0 (cit. on p. 8).

[54] Natalia Rinaldi-Montes, Pedro Gorria, David Martínez-Blanco, et al. "Size effects on the Néel temperature of antiferromagnetic NiO nanoparticles". In: *AIP Advances* 6.5 (May 2016), p. 056104. DOI: 10.1063/1.4943062 (cit. on p. 8).

[55] V.M.T.S. Barthem, C.V. Colin, H. Mayaffre, M.-H. Julien, and D. Givord. "Revealing the properties of Mn2Au for antiferromagnetic spintronics". In: *Nature Communications* 4.1 (Dec. 2013), p. 2892. DOI: 10.1038/ncomms3892 (cit. on p. 8).

[56] A. Manchon, J. Železný, I. M. Miron, et al. "Current-induced spin-orbit torques in ferromagnetic and antiferromagnetic systems". In: *Reviews of Modern Physics* 91.3 (Sept. 2019), p. 035004. DOI: 10.1103/RevModPhys.91.035004 (cit. on pp. 8, 17, 18, 40, 42, 62, 70).

[57] O. Gomonay, T. Jungwirth, and J. Sinova. "High Antiferromagnetic Domain Wall Velocity Induced by Néel Spin-Orbit Torques". In: *Physical Review Letters* 117.1 (June 2016), p. 017202. DOI: 10.1103/PhysRevLett.117.017202 (cit. on p. 8).

[58] Richard P. Michel, Alison Chaiken, Young K. Kim, and Lantz E. Johnson. "NiO Exchange Bias Layers Grown by Direct Ion Beam Sputtering of a Nickel Oxide Target". In: *IEEE Transactions on Magnetics* 32.5 PART 2 (1996), pp. 4651–4653. DOI: 10.1109/20.539107 (cit. on p. 9).

[59] J Nogués and Ivan K Schuller. "Exchange bias". In: *Journal of Magnetism and Magnetic Materials* 192.2 (Feb. 1999), pp. 203–232. DOI: 10.1016/S0304-8853(98)00266-2 (cit. on pp. 9, 63).

[60] J. Nogués, D. Lederman, T. J. Moran, and Ivan K. Schuller. “Positive Exchange Bias in Fe <math display="inline"> <mrow> <msub> <mrow> <mi mathvariant="normal">F</mi> </mrow> <mrow> <mn>2</mn> </mrow> </msub> </mrow> </math> -Fe Bilayers”. In: *Physical Review Letters* 76.24 (June 1996), pp. 4624–4627. DOI: 10.1103/PhysRevLett.76.4624 (cit. on p. 9).

[61] G. Vallejo-Fernandez, L. E. Fernandez-Outon, and K. O’Grady. “Antiferromagnetic grain volume effects in metallic polycrystalline exchange bias systems”. In: *Journal of Physics D: Applied Physics* 41.11 (June 2008). DOI: 10.1088/0022-3727/41/11/112001 (cit. on pp. 9, 10).

[62] Yu Shiratsuchi, Hayato Noutomi, Hiroto Oikawa, et al. “Detection and In Situ Switching of Unreversed Interfacial Antiferromagnetic Spins in a Perpendicular-Exchange-Biased System”. In: *Physical Review Letters* 109.7 (Aug. 2012), p. 077202. DOI: 10.1103/PhysRevLett.109.077202 (cit. on pp. 9, 63, 64, 66, 67, 77).

[63] Haiwen Xi, Robert M. White, Zheng Gao, and Sining Mao. “Antiferromagnetic thickness dependence of blocking temperature in exchange coupled polycrystalline ferromagnet/antiferromagnet bilayers”. In: *Journal of Applied Physics* 92.8 (Oct. 2002), pp. 4828–4830. DOI: 10.1063/1.1503159 (cit. on p. 10).

[64] X. Martí, B. G. Park, J. Wunderlich, et al. “Electrical Measurement of Antiferromagnetic Moments in Exchange-Coupled IrMn/NiFe Stacks”. In: *Physical Review Letters* 108.1 (Jan. 2012), p. 017201. DOI: 10.1103/PhysRevLett.108.017201 (cit. on p. 10).

[65] J. Nogués, J. Sort, V. Langlais, et al. “Exchange bias in nanostructures”. In: *Physics Reports* 422.3 (Dec. 2005), pp. 65–117. DOI: 10.1016/j.physrep.2005.08.004 (cit. on p. 10).

[66] Andrew D. Kent and Daniel C. Worledge. “A new spin on magnetic memories”. In: *Nature Nanotechnology* 10.3 (Mar. 2015), pp. 187–191. DOI: 10.1038/nnano.2015.24 (cit. on p. 10).

[67] Jiajun Guo, Xiaonan Zhao, Zhijian Lu, et al. “High exchange-bias blocking temperature in an ultrathin amorphous antiferromagnet system”. In: *Physical Review B* 104.10 (Sept. 2021), p. L100401. DOI: 10.1103/PhysRevB.104.L100401 (cit. on p. 10).

[68] K. O’Grady, L. E. Fernandez-Outon, and G. Vallejo-Fernandez. *A new paradigm for exchange bias in polycrystalline thin films*. Apr. 2010. DOI: 10.1016/j.jmmm.2009.12.011 (cit. on p. 10).

[69] G. Krishnaswamy, A. Kurenkov, Giacomo Sala, et al. “Multidomain Memristive Switching of Pt38Mn62/[Co/Pt] multilayers”. In: *Physical Review Applied* 14.4 (Oct. 2020), p. 044036. DOI: 10.1103/PhysRevApplied.14.044036 (cit. on pp. 10, 63, 68).

[70] Shunsuke Fukami, Chaoliang Zhang, Samik DuttaGupta, Aleksandr Kurenkov, and Hideo Ohno. “Magnetization switching by spin–orbit torque in an antiferromagnet–ferromagnet bilayer system”. In: *Nature Materials* 15.5 (May 2016), pp. 535–541. DOI: 10.1038/nmat4566 (cit. on pp. 10, 63, 68).

[71] Young-Wan Oh, Seung-heon Chris Baek, Y. M. Kim, et al. “Field-free switching of perpendicular magnetization through spin–orbit torque in antiferromagnet/ferromagnet/oxide structures”. In: *Nature Nanotechnology* 11.10 (Oct. 2016), pp. 878–884. DOI: 10.1038/nnano.2016.109 (cit. on pp. 10, 63, 68).

[72] A. van den Brink, G. Vermijs, A. Solignac, et al. “Field-free magnetization reversal by spin-Hall effect and exchange bias”. In: *Nature Communications* 7.1 (Apr. 2016), p. 10854. DOI: 10.1038/ncomms10854 (cit. on pp. 10, 63, 68).

[73] R C O’handley. *Magnetic Materials*. 2001 (cit. on p. 11).

[74] Yunlong Geng. “Microstructure and Magnetic Behavior Studies of Processing-controlled and Composition-modified Fe-Ni and Mn-Al Alloys”. PhD thesis. University of Nebraska, 2014 (cit. on p. 11).

[75] Charles Kittel. “Theory of the Structure of Ferromagnetic Domains in Films and Small Particles”. In: *Physical Review* 70.11-12 (Dec. 1946), pp. 965–971. DOI: 10.1103/PhysRev.70.965 (cit. on p. 11).

[76] Wolfgang Kuch, Rudolf Schäfer, Peter Fischer, and Franz Ulrich Hillebrecht. “Magnetic Microscopy of Layered Structures”. In: *Magneto Microscopy of layered structures*. Springer US, 2015, pp. 19–95. DOI: 10.1007/978-3-662-44532-7{_}2 (cit. on pp. 11, 12, 14, 34).

[77] Saül Vélez, Jakob Schaab, Martin S. Wörnle, et al. “High-speed domain wall racetracks in a magnetic insulator”. In: *Nature Communications* 10.1 (Dec. 2019), p. 4750. DOI: 10.1038/s41467-019-12676-7 (cit. on p. 11).

[78] Sang-Wook Cheong, Manfred Fiebig, Weida Wu, Laurent Chapon, and Valery Kiryukhin. “Seeing is believing: visualization of antiferromagnetic domains”. In: *npj Quantum Materials* 5.1 (Jan. 2020), p. 3. DOI: 10.1038/s41535-019-0204-x (cit. on p. 12).

[79] Kuniaki Arai, Taichi Okuda, Arata Tanaka, et al. “Three-dimensional spin orientation in antiferromagnetic domain walls of NiO studied by x-ray magnetic linear dichroism photoemission electron microscopy”. In: *Physical Review B* 85.10 (Mar. 2012), p. 104418. DOI: 10.1103/PhysRevB.85.104418 (cit. on p. 12).

[80] I. Sanger, V. V. Pavlov, M. Bayer, and Manfred Fiebig. “Distribution of antiferromagnetic spin and twin domains in NiO”. In: *Physical Review B* 74.14 (Oct. 2006), p. 144401. DOI: 10.1103/PhysRevB.74.144401 (cit. on p. 12).

[81] Hendrik Meer, Felix Schreiber, Christin Schmitt, et al. “Direct Imaging of Current-Induced Antiferromagnetic Switching Revealing a Pure Thermomagnetoelastic Switching Mechanism in NiO”. In: *Nano Letters* 21.1 (Jan. 2021), pp. 114–119. DOI: 10.1021/acs.nanolett.0c03367 (cit. on pp. 12, 22, 23, 42).

[82] H. C. B. Zhao, H. Xia, S. Hu, et al. “Large ultrafast-modulated Voigt effect in noncollinear antiferromagnet Mn3Sn”. In: *Nature Communications* 12.1 (Dec. 2021), p. 5266. DOI: 10.1038/s41467-021-25654-9 (cit. on p. 12).

[83] Shinji Miwa, Satoshi Iihama, Takuya Nomoto, et al. “Giant Effective Damping of Octupole Oscillation in an Antiferromagnetic Weyl Semimetal”. In: *Small Science* 1.5 (May 2021), p. 2000062. DOI: 10.1002/smsc.202000062 (cit. on p. 12).

[84] Herbert Hopster and Hans Peter Oepen. *Magnetic microscopy of nanostructures*. Ed. by Springer Science & Business Media. 2005 (cit. on p. 12).

[85] Andy F. Zhou, J. Kevin Erwin, Charles F. Brucker, and M. Mansuripur. "Dielectric tensor characterization for magneto-optical recording media". In: *Applied Optics* 31.29 (Oct. 1992), p. 6280. DOI: 10.1364/AO.31.006280 (cit. on p. 13).

[86] Felix Schreiber, Lorenzo Baldrati, Christin Schmitt, et al. "Concurrent magneto-optical imaging and magneto-transport readout of electrical switching of insulating antiferromagnetic thin films". In: *arXiv* 117.8 (Apr. 2020), pp. 1–14. DOI: 10.1063/5.0011852 (cit. on pp. 13, 41, 47, 58).

[87] C Tannous and J Gieraltowski. "The Stoner–Wohlfarth model of ferromagnetism". In: *European Journal of Physics* 29.3 (May 2008), pp. 475–487. DOI: 10.1088/0143-0807/29/3/008 (cit. on p. 15).

[88] N. L. Schryer and L. R. Walker. "The motion of 180° domain walls in uniform dc magnetic fields". In: *Journal of Applied Physics* 45.12 (Dec. 1974), pp. 5406–5421. DOI: 10.1063/1.1663252 (cit. on p. 16).

[89] Vincent Jeudy, R. Díaz Pardo, W. Savero Torres, S. Bustingorry, and A. B. Kolton. "Pinning of domain walls in thin ferromagnetic films". In: *Physical Review B* 98.5 (Aug. 2018), p. 054406. DOI: 10.1103/PhysRevB.98.054406 (cit. on pp. 16, 22, 69, 70).

[90] Vincent Jeudy, A. Mougin, S. Bustingorry, et al. "Universal Pinning Energy Barrier for Driven Domain Walls in Thin Ferromagnetic Films". In: *Physical Review Letters* 117.5 (July 2016), p. 057201. DOI: 10.1103/PhysRevLett.117.057201 (cit. on p. 17).

[91] R. Diaz Pardo, W. Savero Torres, A. B. Kolton, S. Bustingorry, and Vincent Jeudy. "Universal depinning transition of domain walls in ultrathin ferromagnets". In: *Physical Review B* 95.18 (May 2017), p. 184434. DOI: 10.1103/PhysRevB.95.184434 (cit. on pp. 17, 22, 62).

[92] Pascal Chauve, Thierry Giamarchi, and Pierre Le Doussal. "Creep and depinning in disordered media". In: *Physical Review B* 62.10 (Sept. 2000), pp. 6241–6267. DOI: 10.1103/PhysRevB.62.6241 (cit. on p. 17).

[93] S Lemerle, J Ferré, C Chappert, et al. "Domain Wall Creep in an Ising Ultrathin Magnetic Film". In: *Physical review letters* 80.4 (Jan. 1998) (cit. on p. 17).

[94] F. Cayssol, D. Ravelosona, C. Chappert, J. Ferré, and J. P. Jamet. "Domain Wall Creep in Magnetic Wires". In: *Physical Review Letters* 92.10 (Mar. 2004), p. 107202 (cit. on pp. 17, 62, 68, 69).

[95] D. C. Ralph and M. D. Stiles. "Spin transfer torques". In: *Journal of Magnetism and Magnetic Materials* 320.7 (2008), pp. 1190–1216. DOI: 10.1016/j.jmmm.2007.12.019 (cit. on p. 17).

[96] Kevin Garello, Can Onur Avci, Ioan Mihai Miron, et al. "Ultrafast magnetization switching by spin-orbit torques". In: *Applied Physics Letters* 105.21 (2014). DOI: 10.1063/1.4902443 (cit. on p. 18).

[97] K. V. Shanavas, Z. S. Popović, and S. Satpathy. "Theoretical model for Rashba spin-orbit interaction in d electrons". In: *Physical Review B* 90.16 (Oct. 2014), p. 165108. DOI: 10.1103/PhysRevB.90.165108 (cit. on p. 18).

[98] G Bihlmayer, O Rader, and R Winkler. "Focus on the Rashba effect". In: *New Journal of Physics* 17.5 (May 2015), p. 050202. DOI: 10.1088/1367-2630/17/5/050202 (cit. on p. 18).

[99] J. E. Hirsch. "Spin Hall Effect". In: *Physical Review Letters* 83.9 (Aug. 1999), pp. 1834–1837. DOI: 10.1103/PhysRevLett.83.1834 (cit. on p. 19).

[100] Jairo Sinova, Sergio O. Valenzuela, J. Wunderlich, C. H. Back, and T. Jungwirth. "Spin Hall effects". In: *Reviews of Modern Physics* 87.4 (2015), pp. 1213–1260. DOI: 10.1103/RevModPhys.87.1213 (cit. on p. 19).

[101] Axel Hoffmann. "Spin hall effects in metals". In: *IEEE Transactions on Magnetics* 49.10 (2013), pp. 5172–5193. DOI: 10.1109/TMAG.2013.2262947 (cit. on p. 19).

[102] Pietro Gambardella and Ioan Mihai Miron. "Current-induced spin–orbit torques". In: *Philosophical Transactions of the Royal Society A: Mathematical, Physical and Engineering Sciences* 369.1948 (Aug. 2011), pp. 3175–3197. DOI: 10.1098/rsta.2010.0336 (cit. on p. 19).

[103] P. P. J. Haazen, E. Murè, J. H. Franken, et al. "Domain wall depinning governed by the spin Hall effect". In: *Nature Materials* 12.4 (Apr. 2013), pp. 299–303. DOI: 10.1038/nmat3553 (cit. on pp. 19, 97).

[104] Olivier Boulle, S. Rohart, L. D. Buda-Prejbeanu, et al. "Domain Wall Tilting in the Presence of the Dzyaloshinskii-Moriya Interaction in Out-of-Plane Magnetized Magnetic Nanotracks". In: *Physical Review Letters* 111.21 (Nov. 2013), p. 217203. DOI: 10.1103/PhysRevLett.111.217203 (cit. on pp. 20, 62, 68, 70).

[105] Manuel Baumgartner and Pietro Gambardella. "Asymmetric velocity and tilt angle of domain walls induced by spin-orbit torques". In: *Applied Physics Letters* 113.24 (Dec. 2018), p. 242402. DOI: 10.1063/1.5063456 (cit. on pp. 20, 62, 70).

[106] Pietro Diona, Luca Gnoli, and Fabrizio Riente. "Simulation and Modeling of Racetrack Memories With VCMA Synchronization". In: *IEEE Transactions on Electron Devices* 69.7 (July 2022), pp. 3675–3680. DOI: 10.1109/TED.2022.3173920 (cit. on p. 20).

[107] L. Herrera Diez, Vincent Jeudy, G. Durin, et al. "Wire edge dependent magnetic domain wall creep". In: *Physical Review B* 98.5 (Aug. 2018), p. 054417. DOI: 10.1103/PhysRevB.98.054417 (cit. on p. 22).

[108] Kowsar Shahbazi, Joo-Von Kim, Hans T. Nembach, et al. "Domain-wall motion and interfacial Dzyaloshinskii-Moriya interactions in Pt/Co/Ir/Ta multilayers". In: *Physical Review B* 99.9 (Mar. 2019), p. 094409. DOI: 10.1103/PhysRevB.99.094409 (cit. on pp. 22, 69).

[109] R. Díaz Pardo, N. Moisan, L. J. Albornoz, et al. "Common universal behavior of magnetic domain walls driven by spin-polarized electrical current and magnetic field". In: *Physical Review B* 100.18 (Nov. 2019), p. 184420. DOI: 10.1103/PhysRevB.100.184420 (cit. on pp. 22, 79, 93).

[110] Egecan Cogulu, Nahuel N. Statuto, Yang Cheng, et al. “Direct imaging of electrical switching of antiferromagnetic Néel order in a-Fe2O3 epitaxial films”. In: *Physical Review B* 103.10 (Mar. 2021), p. L100405. DOI: 10.1103/PhysRevB.103.L100405 (cit. on p. 23).

[111] Dongwook Go and Hyun-Woo Lee. “Orbital torque: Torque generation by orbital current injection”. In: *Physical Review Research* 2.1 (Feb. 2020), p. 013177. DOI: 10.1103/PhysRevResearch.2.013177 (cit. on pp. 24, 25).

[112] Dongwook Go, Frank Freimuth, Jan-Philipp Hanke, et al. “Theory of current-induced angular momentum transfer dynamics in spin-orbit coupled systems”. In: *Physical Review Research* 2.3 (Sept. 2020), p. 033401. DOI: 10.1103/PhysRevResearch.2.033401 (cit. on p. 24).

[113] Dongwook Go, Daegeun Jo, Hyun-Woo Lee, Mathias Kläui, and Yuriy Mokrousov. “Orbitronics: Orbital currents in solids”. In: *EPL (Europhysics Letters)* 135.3 (Aug. 2021), p. 37001. DOI: 10.1209/0295-5075/ac2653 (cit. on p. 24).

[114] T. Tanaka, H. Kontani, M. Naito, et al. “Intrinsic spin Hall effect and orbital Hall effect in 4d, 5d transition metals”. In: *Physical Review B* 77.16 (Apr. 2008), p. 165117. DOI: 10.1103/PhysRevB.77.165117 (cit. on p. 24).

[115] H. Kontani, T. Tanaka, D. S. Hirashima, K. Yamada, and J. Inoue. “Giant Orbital Hall Effect in Transition Metals: Origin of Large Spin and Anomalous Hall Effects”. In: *Physical Review Letters* 102.1 (Jan. 2009), p. 016601. DOI: 10.1103/PhysRevLett.102.016601 (cit. on p. 24).

[116] Dongwook Go, Daegeun Jo, Changyoung Kim, and Hyun-Woo Lee. “Intrinsic Spin and Orbital Hall Effects from Orbital Texture”. In: *Physical Review Letters* 121.8 (Aug. 2018), p. 086602. DOI: 10.1103/PhysRevLett.121.086602 (cit. on p. 24).

[117] Daegeun Jo, Dongwook Go, and Hyun-Woo Lee. “Gigantic intrinsic orbital Hall effects in weakly spin-orbit coupled metals”. In: *Physical Review B* 98.21 (Dec. 2018), p. 214405. DOI: 10.1103/PhysRevB.98.214405 (cit. on pp. 24, 83).

[118] Giacomo Sala and Pietro Gambardella. “Giant orbital Hall effect and orbital-to-spin conversion in 3d, 5d and 4f metallic heterostructures”. In: *Physical Review Research* 4.3 (July 2022), p. 033037. DOI: 10.1103/PhysRevResearch.4.033037 (cit. on pp. 24, 83, 88, 97).

[119] Soogil Lee, Min-Gu Kang, Dongwook Go, et al. “Efficient conversion of orbital Hall current to spin current for spin-orbit torque switching”. In: *Communications Physics* 4.1 (Nov. 2021), p. 234. DOI: 10.1038/s42005-021-00737-7 (cit. on pp. 24, 83).

[120] Chun-Yeol You, In Mo Sung, and Byung-Kyu Joe. “Analytic expression for the temperature of the current-heated nanowire for the current-induced domain wall motion”. In: *Applied Physics Letters* 89.22 (Nov. 2006), p. 222513. DOI: 10.1063/1.2399441 (cit. on pp. 32, 33, 48, 53).

[121] A. Yamaguchi, S. Nasu, H. Tanigawa, et al. “Effect of Joule heating in current-driven domain wall motion”. In: *Applied Physics Letters* 86.1 (Jan. 2005), p. 012511. DOI: 10.1063/1.1847714 (cit. on pp. 32, 48).

[122] Benjamin Julien Jacot, G. Krishnaswamy, Giacomo Sala, et al. “Systematic study of nonmagnetic resistance changes due to electrical pulsing in single metal layers and metal/antiferromagnet bilayers”. In: *Journal of Applied Physics* 128.17 (Nov. 2020), p. 173902. DOI: 10.1063/5.0026147 (cit. on pp. 40, 131).

[123] Manfred Fiebig, Nguyen Phuc Duong, Takuya Satoh, et al. “Ultrafast magnetization dynamics of antiferromagnetic compounds”. In: *Journal of Physics D: Applied Physics* 41.16 (Aug. 2008), p. 164005. DOI: 10.1088/0022-3727/41/16/164005 (cit. on p. 40).

[124] Peter Wadley, B. Howells, J. Elezny, et al. “Electrical switching of an antiferromagnet”. In: *Science* 351.6273 (Feb. 2016), pp. 587–590. DOI: 10.1126/science.aab1031 (cit. on pp. 40, 42, 43).

[125] Peter Wadley, Sonka Reimers, Michal J. Grzybowski, et al. “Current polarity-dependent manipulation of antiferromagnetic domains”. In: *Nature Nanotechnology* 13.5 (May 2018), pp. 362–365. DOI: 10.1038/s41565-018-0079-1 (cit. on pp. 40, 42).

[126] X. F. Zhou, J. Zhang, F. Li, et al. “Strong Orientation-Dependent Spin-Orbit Torque in Thin Films of the Antiferromagnet Mn2Au”. In: *Physical Review Applied* 9.5 (May 2018), p. 054028. DOI: 10.1103/PhysRevApplied.9.054028 (cit. on pp. 40, 42).

[127] Markus Meinert, Dominik Graulich, and Tristan Matalla-Wagner. “Electrical Switching of Antiferromagnetic Mn2Au and the Role of Thermal Activation”. In: *Physical Review Applied* 9.6 (June 2018), p. 064040. DOI: 10.1103/PhysRevApplied.9.064040 (cit. on pp. 40, 42).

[128] S. Yu Bodnar, L. Šmejkal, I. Turek, et al. “Writing and reading antiferromagnetic Mn2Au by Néel spin-orbit torques and large anisotropic magnetoresistance”. In: *Nature Communications* 9.1 (Dec. 2018), p. 348. DOI: 10.1038/s41467-017-02780-x (cit. on pp. 40, 42).

[129] Xianzhe Chen, Xiaofeng Zhou, Ran Cheng, et al. “Electric field control of Néel spin–orbit torque in an antiferromagnet”. In: *Nature Materials* 18.9 (Sept. 2019), pp. 931–935. DOI: 10.1038/s41563-019-0424-2 (cit. on pp. 40, 42).

[130] Nityan L. Nair, Eran Maniv, Caolan John, et al. “Electrical switching in a magnetically intercalated transition metal dichalcogenide”. In: *Nature Materials* 19.2 (Feb. 2020), pp. 153–157. DOI: 10.1038/s41563-019-0518-x (cit. on pp. 40, 42, 58).

[131] M. Dunz, T. Matalla-Wagner, and M. Meinert. “Spin-orbit torque induced electrical switching of antiferromagnetic MnN”. In: *Physical Review Research* 2.1 (Mar. 2020), p. 013347. DOI: 10.1103/PhysRevResearch.2.013347 (cit. on pp. 40, 41).

[132] K. A. Omari, L. X. Barton, O. Amin, et al. “Low-energy switching of antiferromagnetic CuMnAs/GaP using sub-10 nanosecond current pulses”. In: *Journal of Applied Physics* 127.19 (May 2020), p. 193906. DOI: 10.1063/5.0006183 (cit. on pp. 40, 42).

[133] Hanshen Tsai, Tomoya Higo, Kouta Kondou, et al. “Electrical manipulation of a topological antiferromagnetic state”. In: *Nature* 580.7805 (2020), pp. 608–613. DOI: 10.1038/s41586-020-2211-2 (cit. on pp. 40, 41).

[134] X. Z. Chen, R. Zarzuela, J. Zhang, et al. “Antidamping-Torque-Induced Switching in Biaxial Antiferromagnetic Insulators”. In: *Physical Review Letters* 120.20 (May 2018), p. 207204. DOI: 10.1103/PhysRevLett.120.207204 (cit. on pp. 40, 42, 47, 58).

[135] Pengxiang Zhang, Joseph Finley, Taqiyyah Safi, and Luqiao Liu. “Quantitative Study on Current-Induced Effect in an Antiferromagnet Insulator/Pt Bilayer Film”. In: *Physical Review Letters* 123.24 (Dec. 2019), p. 247206. DOI: 10.1103/PhysRevLett.123.247206 (cit. on pp. 40–42).

[136] Yang Cheng, Sisheng Yu, Menglin Zhu, Jinwoo Hwang, and Fengyuan Yang. “Electrical Switching of Tristate Antiferromagnetic Néel Order in alpha-Fe2O3 epitaxial films”. In: *Physical Review Letters* 124.2 (Jan. 2020), p. 027202. DOI: 10.1103/PhysRevLett.124.027202 (cit. on pp. 40, 41).

[137] U. Schmid and H. Seidel. “Effect of high temperature annealing on the electrical performance of titanium/platinum thin films”. In: *Thin Solid Films* 516.6 (Jan. 2008), pp. 898–906. DOI: 10.1016/j.tsf.2007.04.128 (cit. on p. 40).

[138] Paul S. Ho and Thomas Kwok. “Electromigration in metals”. In: *Reports on Progress in Physics* 52.3 (Mar. 1989), pp. 301–348. DOI: 10.1088/0034-4885/52/3/002 (cit. on p. 40).

[139] C. C. Chiang, S. Y. Huang, D. Qu, P. H. Wu, and C. L. Chien. “Absence of Evidence of Electrical Switching of the Antiferromagnetic Néel Vector”. In: *Physical Review Letters* 123.22 (Nov. 2019), p. 227203. DOI: 10.1103/PhysRevLett.123.227203 (cit. on pp. 41, 47–49, 58).

[140] Tristan Matalla-Wagner, Jan-Michael Schmalhorst, Günter Reiss, Nobumichi Tamura, and Markus Meinert. “Resistive contribution in electrical-switching experiments with antiferromagnets”. In: *Physical Review Research* 2.3 (July 2020), p. 033077. DOI: 10.1103/PhysRevResearch.2.033077 (cit. on pp. 41, 47, 48, 58).

[141] A. Churikova, D. Bono, B. Neltner, et al. “Non-magnetic origin of spin Hall magnetoresistance-like signals in Pt films and epitaxial NiO/Pt bilayers”. In: *Applied Physics Letters* 116.2 (Jan. 2020), p. 022410. DOI: 10.1063/1.5134814 (cit. on pp. 41, 47, 48, 50, 58).

[142] X.F. F. Zhou, X.Z. Z. Chen, J. Zhang, et al. “From Fieldlike Torque to Antidamping Torque in Antiferromagnetic Mn2Au”. In: *Physical Review Applied* 11.5 (May 2019), p. 054030. DOI: 10.1103/PhysRevApplied.11.054030 (cit. on p. 41).

[143] Jiacheng Shi, Victor Lopez-Dominguez, Francesca Garesci, et al. “Electrical manipulation of the magnetic order in antiferromagnetic PtMn pillars”. In: *Nature Electronics* 3.2 (Feb. 2020), pp. 92–98. DOI: 10.1038/s41928-020-0367-2 (cit. on p. 41).

[144] Takahiro Moriyama, Weinan Zhou, Takeshi Seki, Koki Takanashi, and Teruo Ono. “Spin-Orbit-Torque Memory Operation of Synthetic Antiferromagnets”. In: *Physical Review Letters* 121.16 (2018), p. 167202. DOI: 10.1103/PhysRevLett.121.167202 (cit. on p. 41).

[145] J. Zelezny, H. Gao, K. Vyborny, et al. “Relativistic Neel-order fields induced by electrical current in antiferromagnets”. In: *Physical Review Letters* 113.15 (Oct. 2014), p. 157201. DOI: 10.1103/PhysRevLett.113.157201 (cit. on p. 42).

[146] Ioan Mihai Miron, Kevin Garello, Gilles Gaudin, et al. “Perpendicular switching of a single ferromagnetic layer induced by in-plane current injection”. In: *Nature* 476.7359 (Aug. 2011), pp. 189–193. DOI: 10.1038/nature10309 (cit. on p. 42).

[147] Can Onur Avci, Andy Quindeau, Chi-Feng Pai, et al. “Current-induced switching in a magnetic insulator”. In: *Nature Materials* 16.3 (Mar. 2017), pp. 309–314. DOI: 10.1038/nmat4812 (cit. on p. 42).

[148] Erlend G. Tveten, Alireza Qaiumzadeh, and Arne Brataas. “Antiferromagnetic Domain Wall Motion Induced by Spin Waves”. In: *Physical Review Letters* 112.14 (Apr. 2014), p. 147204. DOI: 10.1103/PhysRevLett.112.147204 (cit. on p. 42).

[149] Takayuki Shiino, Se-Hyeok Oh, Paul M. Haney, et al. “Antiferromagnetic Domain Wall Motion Driven by Spin-Orbit Torques”. In: *Physical Review Letters* 117.8 (Aug. 2016), p. 087203. DOI: 10.1103/PhysRevLett.117.087203 (cit. on p. 42).

[150] A. S. Núñez, Rembert A. Duine, Paul Haney, and A. H. MacDonald. “Theory of spin torques and giant magnetoresistance in antiferromagnetic metals”. In: *Physical Review B* 73.21 (June 2006), p. 214426. DOI: 10.1103/PhysRevB.73.214426 (cit. on p. 43).

[151] Yan-Ting Chen, Saburo Takahashi, Hiroyasu Nakayama, et al. “Theory of spin Hall magnetoresistance”. In: *Physical Review B* 87.14 (Apr. 2013), p. 144411. DOI: 10.1103/PhysRevB.87.144411 (cit. on p. 43).

[152] Dazhi Hou, Zhiyong Qiu, Joseph Barker, et al. “Tunable Sign Change of Spin Hall Magnetoresistance in Pt/NiO/YIG Structures”. In: *Physical Review Letters* 118.14 (Apr. 2017), p. 147202. DOI: 10.1103/PhysRevLett.118.147202 (cit. on p. 43).

[153] L. Baldrati, A. Ross, T. Niizeki, et al. “Full angular dependence of the spin Hall and ordinary magnetoresistance in epitaxial antiferromagnetic NiO(001)/Pt thin films”. In: *Physical Review B* 98.2 (July 2018), p. 024422. DOI: 10.1103/PhysRevB.98.024422 (cit. on p. 43).

[154] F. B. Hagedorn and P. M. Hall. “Right-Angle Bends in Thin Strip Conductors”. In: *Journal of Applied Physics* 34.1 (Jan. 1963), pp. 128–133. DOI: 10.1063/1.1729052 (cit. on p. 44).

[155] Christian Stamm, Christoph Murer, Marco Berritta, et al. “Magneto-Optical Detection of the Spin Hall Effect in Pt and W Thin Films”. In: *Physical Review Letters* 119.8 (Aug. 2017), p. 087203. DOI: 10.1103/PhysRevLett.119.087203 (cit. on p. 45).

[156] J.S. Agustsson, U.B. Arnalds, A.S. Ingason, et al. “Growth, coalescence, and electrical resistivity of thin Pt films grown by dc magnetron sputtering on SiO2”. In: *Applied Surface Science* 254.22 (Sept. 2008), pp. 7356–7360. DOI: 10.1016/j.apsusc.2008.05.335 (cit. on p. 45).

[157] Ulrich Schmid. “The impact of thermal annealing and adhesion film thickness on the resistivity and the agglomeration behavior of titanium/platinum thin films”. In: *Journal of Applied Physics* 103.5 (Mar. 2008), p. 054902. DOI: 10.1063/1.2838229 (cit. on pp. 45, 47).

[158] Li Xiao, Zhan Zhao, Lidong Du, Shaohua Wu, and Qimin Liu. “Annealing effect on the stability of platinum thin films covered by SiO2 or SiNx layer”. In: *IEEE Intl. Conf. on Nano/Micro Engineered and Molecular Systems*. Vol. 1. IEEE, Apr. 2013, pp. 352–355. DOI: 10.1109/NEMS.2013.6559749 (cit. on p. 47).

[159] P. Luo, Z. Lu, Z. G. Zhu, et al. “Prominent β -relaxations in yttrium based metallic glasses”. In: *Applied Physics Letters* 106.3 (Jan. 2015), p. 031907. DOI: 10.1063/1.4906452 (cit. on p. 49).

[160] P. Luo, P. Wen, H. Y. Bai, B. Ruta, and W. H. Wang. “Relaxation Decoupling in Metallic Glasses at Low Temperatures”. In: *Physical Review Letters* 118.22 (May 2017), p. 225901. DOI: 10.1103/PhysRevLett.118.225901 (cit. on p. 49).

[161] S.-M. Lee and David G. Cahill. “Heat transport in thin dielectric films”. In: *Journal of Applied Physics* 81.6 (Mar. 1997), pp. 2590–2595. DOI: 10.1063/1.363923 (cit. on pp. 53, 54).

[162] substrate provided by MTI-Corporation. *Al2O3 Single Crystal Sapphire boule and polished wafer*. 2019. DOI: http://www.mtixtl.com/xtlflyers/Al2O3.pdf (cit. on pp. 53, 54).

[163] Nenad Stojanovic, Jongsin Yun, Jordan M. Berg, Mark Holtz, and Henryk Temkin. “Model-based data analysis for thin-film thermal conductivity measurement using microelectrothermal test structures”. In: *ASME International Mechanical Engineering Congress and Exposition, Proceedings (IMECE)* 11.5 (2007), pp. 639–645. DOI: 10.1115/IMECE2007-42750 (cit. on p. 53).

[164] A. J. Griffin, F. R. Brotzen, and P. J. Loos. “The effective transverse thermal conductivity of amorphous Si 3 N 4 thin films”. In: *Journal of Applied Physics* 76.7 (Oct. 1994), pp. 4007–4011. DOI: 10.1063/1.357347 (cit. on p. 54).

[165] Benjamin Julien Jacot, S Vélez, P Noël, et al. “Control of field- and current-driven magnetic domain wall motion by exchange bias in Cr2O3/Co/Pt trilayers”. In: *Physical Review B* 106.13 (Oct. 2022), p. 134411. DOI: 10.1103/PhysRevB.106.134411 (cit. on pp. 61, 131).

[166] A.P. Malozemoff and J.C. Slonczewski. *Magnetic Domain Walls in Bubble Materials*. Elsevier, 1979. DOI: 10.1016/C2013-0-06998-8 (cit. on p. 62).

[167] André Thiaville and Yoshinobu Nakatani. “Domain-wall dynamics in nanowires and nanostrips”. In: *Topics in Applied Physics* 101 (Oct. 2006), pp. 161–205. DOI: 10.1007/10938171{_}5 (cit. on p. 62).

[168] P. J. Metaxas, J. P. Jamet, A. Mougin, et al. “Creep and Flow Regimes of Magnetic Domain-Wall Motion in Ultrathin Pt/Co/Pt Films with Perpendicular Anisotropy”. In: *Physical Review Letters* 99.21 (Nov. 2007), p. 217208. DOI: 10.1103/PhysRevLett.99.217208 (cit. on pp. 62, 63, 68).

[169] O. Boulle, G. Malinowski, and Mathias Kläui. “Current-induced domain wall motion in nanoscale ferromagnetic elements”. In: *Materials Science and Engineering R: Reports* 72.9 (2011), pp. 159–187. DOI: 10.1016/j.mser.2011.04.001 (cit. on p. 62).

[170] R. Spain and M. Marino. “Magnetic film domain-wall motion devices”. In: *IEEE Transactions on Magnetics* 6.3 (Sept. 1970), pp. 451–463. DOI: 10.1109/TMAG.1970.1066853 (cit. on p. 62).

[171] Stuart Parkin and See-Hun Yang. “Memory on the racetrack”. In: *Nature Nanotechnology* 10.3 (Mar. 2015), pp. 195–198. DOI: 10.1038/nnano.2015.41 (cit. on p. 62).

[172] D. A. Allwood, G. Xiong, C. C. Faulkner, et al. “Magnetic domain-wall logic”. In: *Science* 309.5741 (Sept. 2005), pp. 1688–1692. DOI: 10.1126/science.1108813 (cit. on p. 62).

[173] Zhaochu Luo, Aleš Hrabec, Trong Phuong Dao, et al. “Current-driven magnetic domain-wall logic”. In: *Nature* 579.7798 (Mar. 2020), pp. 214–218. DOI: 10.1038/s41586-020-2061-y (cit. on pp. 62, 71).

[174] Soong-Geun Je, Duck-Ho Kim, Sang Cheol Yoo, et al. “Asymmetric magnetic domain-wall motion by the Dzyaloshinskii-Moriya interaction”. In: *Physical Review B - Condensed Matter and Materials Physics* 88.21 (2013), pp. 1–5. DOI: 10.1103/PhysRevB.88.214401 (cit. on pp. 62, 63, 68, 69, 72).

[175] Aleš Hrabec, N. A. Porter, A. Wells, et al. “Measuring and tailoring the Dzyaloshinskii-Moriya interaction in perpendicularly magnetized thin films”. In: *Physical Review B* 90.2 (July 2014), p. 020402. DOI: 10.1103/PhysRevB.90.020402 (cit. on pp. 62, 63, 68, 69, 72).

[176] Ioan Mihai Miron, Thomas Moore, Helga Szambolics, et al. “Fast current-induced domain-wall motion controlled by the Rashba effect”. In: *Nature Materials* 10.6 (June 2011), pp. 419–423. DOI: 10.1038/nmat3020 (cit. on pp. 62, 63, 71).

[177] Manuel Baumgartner, Kevin Garello, Johannes Mendil, et al. “Spatially and time-resolved magnetization dynamics driven by spin–orbit torques”. In: *Nature Nanotechnology* 12.10 (Oct. 2017), pp. 980–986. DOI: 10.1038/nnano.2017.151 (cit. on pp. 62, 63, 70).

[178] M. Heide, G. Bihlmayer, and S. Blügel. “Dzyaloshinskii-Moriya interaction accounting for the orientation of magnetic domains in ultrathin films: Fe/W(110)”. In: *Physical Review B* 78.14 (Oct. 2008), p. 140403. DOI: 10.1103/PhysRevB.78.140403 (cit. on pp. 62, 69).

[179] Jacob Torrejon, Junyeon Kim, Jaivardhan Sinha, et al. “Interface control of the magnetic chirality in CoFeB/MgO heterostructures with heavy-metal underlayers”. In: *Nature Communications* 5.1 (Dec. 2014), p. 4655. DOI: 10.1038/ncomms5655 (cit. on p. 62).

[180] Gong Chen, Tianping Ma, Alpha T. N’Diaye, et al. “Tailoring the chirality of magnetic domain walls by interface engineering”. In: *Nature Communications* 4.1 (Dec. 2013), p. 2671. DOI: 10.1038/ncomms3671 (cit. on p. 62).

[181] R. Lavrijsen, D. M. F. Hartmann, A. van den Brink, et al. “Asymmetric magnetic bubble expansion under in-plane field in Pt/Co/Pt: Effect of interface engineering”. In: *Physical Review B* 91.10 (Mar. 2015), p. 104414. DOI: 10.1103/PhysRevB.91.104414 (cit. on p. 62).

[182] Kwang-Su Ryu, See-Hun Yang, Luc Thomas, and Stuart S. P. Parkin. “Chiral spin torque arising from proximity-induced magnetization”. In: *Nature Communications* 5.1 (Sept. 2014), p. 3910. DOI: 10.1038/ncomms4910 (cit. on pp. 62, 73).

[183] Mickey Martini, Can Onur Avci, Silvia Tacchi, Charles-Henri Lambert, and Pietro Gambardella. “Engineering the Spin-Orbit-Torque Efficiency and Magnetic Properties of Tb/Co Ferrimagnetic Multilayers by Stacking Order”. In: *Physical Review Applied* 17.4 (Apr. 2022), p. 044056. DOI: 10.1103/PhysRevApplied.17.044056 (cit. on pp. 62, 89).

[184] See-Hun Yang, Kwang-Su Ryu, and Stuart Parkin. “Domain-wall velocities of up to 750 m s-1 driven by exchange-coupling torque in synthetic antiferromagnets”. In: *Nature Nanotechnology* 10.3 (Mar. 2015), pp. 221–226. DOI: 10.1038/nnano.2014.324 (cit. on p. 62).

[185] Mark C. H. de Jong, Can Onur Avci, Aleš Hrabec, and Pietro Gambardella. “Asymmetric depinning of chiral domain walls in ferromagnetic trilayers”. In: *Physical Review B* 102.17 (Nov. 2020), p. 174433. DOI: 10.1103/PhysRevB.102.174433 (cit. on p. 62).

[186] D. Chiba, M. Kawaguchi, S. Fukami, et al. “Electric-field control of magnetic domain-wall velocity in ultrathin cobalt with perpendicular magnetization”. In: *Nature Communications* 3.1 (Jan. 2012), p. 888. DOI: 10.1038/ncomms1888 (cit. on p. 62).

[187] Marine Schott, Laurent Ranno, Hélène Béa, et al. “Electric field control of interfacial Dzyaloshinskii-Moriya interaction in Pt/Co/AlOx thin films”. In: *Journal of Magnetism and Magnetic Materials* 520.January 2020 (Feb. 2021), p. 167122. DOI: 10.1016/j.jmmm.2020.167122 (cit. on p. 62).

[188] M. Vaňatka, J-C Rojas-Sánchez, J. Vogel, et al. “Velocity asymmetry of Dzyaloshinskii domain walls in the creep and flow regimes”. In: *Journal of Physics: Condensed Matter* 27.32 (Aug. 2015), p. 326002. DOI: 10.1088/0953-8984/27/32/326002 (cit. on pp. 63, 68, 69).

[189] M. R. Fitzsimmons, P. Yashar, C. Leighton, et al. “Asymmetric Magnetization Reversal in Exchange-Biased Hysteresis Loops”. In: *Physical Review Letters* 84.17 (Apr. 2000), pp. 3986–3989. DOI: 10.1103/PhysRevLett.84.3986 (cit. on p. 63).

[190] A. Kirilyuk, Th Rasing, H. Jaffres, D. Lacour, and F. Nguyen Van Dau. “Domain strucutres during magnetization reversal in exchange biased layers”. In: *Journal of Applied Physics* 91.10 (2002), p. 7745. DOI: 10.1063/1.1454978 (cit. on p. 63).

[191] J. McCord, Rudolf Schäfer, R. Mattheis, and K.-U. Barholz. “Kerr observations of asymmetric magnetization reversal processes in CoFe/IrMn bilayer systems”. In: *Journal of Applied Physics* 93.9 (May 2003), pp. 5491–5497. DOI: 10.1063/1.1562732 (cit. on p. 63).

[192] Jeffrey McCord and Rudolf Schäfer. “Domain wall asymmetries in Ni 81 Fe 19 /NiO: proof of variable anisotropies in exchange bias systems”. In: *New Journal of Physics* 11.8 (Aug. 2009), p. 083016. DOI: 10.1088/1367-2630/11/8/083016 (cit. on p. 63).

[193] Hun-Sung Lee, Kwang-Su Ryu, Chun-Yeol You, et al. “Asymmetric stochasticity of magnetization reversal dynamics in exchange-biased IrMn/CoFe Film”. In: *Journal of Applied Physics* 111.7 (Apr. 2012), p. 07D731. DOI: 10.1063/1.3694022 (cit. on p. 63).

[194] S. M. Wu, Shane A. Cybart, D. Yi, et al. “Full Electric Control of Exchange Bias”. In: *Physical Review Letters* 110.6 (Feb. 2013), p. 067202. DOI: 10.1103/PhysRevLett.110.067202 (cit. on p. 63).

[195] Risalat A. Khan, Hans T. Nembach, Mannan Ali, et al. “Magnetic domain texture and the Dzyaloshinskii-Moriya interaction in Pt/Co/IrMn and Pt/Co/FeMn thin films with perpendicular exchange bias”. In: *Physical Review B* 98.6 (Aug. 2018), p. 064413. DOI: 10.1103/PhysRevB.98.064413 (cit. on p. 63).

[196] P. Kuświk, M. Matczak, M. Kowacz, et al. “Asymmetric domain wall propagation caused by interfacial Dzyaloshinskii-Moriya interaction in exchange biased Au/-Co/NiO layered system”. In: *Physical Review B* 97.2 (Jan. 2018), p. 024404. DOI: 10.1103/PhysRevB.97.024404 (cit. on p. 63).

[197] Z. Shi, H. Zhong, W.J. Fan, S.M. Zhou, and J. Yuan. “Nanoscale probing of asymmetric magnetization reversal in perpendicularly exchange biased Pt/Co/Pt/IrMn multilayers”. In: *Journal of Magnetism and Magnetic Materials* 474.October 2018 (Mar. 2019), pp. 127–131. DOI: 10.1016/j.jmmm.2018.10.128 (cit. on p. 63).

[198] E. Albisetti and D. Petti. “Domain wall engineering through exchange bias”. In: *Journal of Magnetism and Magnetic Materials* 400 (Feb. 2016), pp. 230–235. DOI: 10.1016/j.jmmm.2015.07.009 (cit. on p. 63).

[199] Yee-Mou Kao, Lance Horng, and Chi-Ho Cheng. “Analytical studies of the magnetic domain wall structure in the presence of non-uniform exchange bias”. In: *AIP Advances* 11.6 (June 2021), p. 065308. DOI: 10.1063/5.0046803 (cit. on p. 63).

[200] I. Polenciuc, A. J. Vick, D. A. Allwood, et al. “Domain wall pinning for racetrack memory using exchange bias”. In: *Applied Physics Letters* 105.16 (Oct. 2014), p. 162406. DOI: 10.1063/1.4899134 (cit. on p. 63).

[201] Hyun-Joong Kim, Soong-Geun Je, Kyoung-Woong Moon, et al. “Programmable Dynamics of Exchange-Biased Domain Wall via Spin-Current-Induced Antiferromagnet Switching”. In: *Advanced Science* 8.17 (Sept. 2021), p. 2100908. DOI: 10.1002/advs.202100908 (cit. on p. 63).

[202] Pavel Borisov, Andreas Hochstrat, Xi Chen, Wolfgang Kleemann, and Christian Binek. “Magnetoelectric Switching of Exchange Bias”. In: *Physical Review Letters* 94.11 (Mar. 2005), p. 117203. DOI: 10.1103/PhysRevLett.94.117203 (cit. on p. 63).

[203] Xi He, Yi Wang, Ning Wu, et al. “Robust isothermal electric control of exchange bias at room temperature”. In: *Nature Materials* 9.7 (July 2010), pp. 579–585. DOI: 10.1038/nmat2785 (cit. on p. 63).

[204] T. Ashida, M. Oida, N. Shimomura, et al. “Observation of magnetoelectric effect in Cr2O3/Pt/Co thin film system”. In: *Applied Physics Letters* 104.15 (Apr. 2014), p. 152409. DOI: 10.1063/1.4871515 (cit. on p. 63).

[205] T. Nozaki, N. Shimomura, T. Ashida, Y. Sato, and M. Sahashi. “Grain Growth Effect of Cr2O3 ilm Layer on Exchange Coupling of Cr2O3/Co Interface”. In: *IEEE Transactions on Magnetics* 48.11 (Nov. 2012), pp. 4359–4362. DOI: 10.1109/TMAG.2012.2195718 (cit. on pp. 63, 64, 66).

[206] Joonghoe Dho, M. G. Blamire, and E. O. Chi. “Correlation of the exchange interaction in Ni81Fe19Cr2O3 bilayers with the antiferromagnetic spin configuration”. In: *Physical Review B - Condensed Matter and Materials Physics* 72.22 (2005), pp. 1–8. DOI: 10.1103/PhysRevB.72.224421 (cit. on pp. 63, 64, 67, 68).

[207] K.-W. Lin and J.-Y. Guo. “Tuning in-plane and out-of-plane exchange biases in Ni80Fe20/Cr-oxide bilayers”. In: *Journal of Applied Physics* 104.12 (Dec. 2008), p. 123913. DOI: 10.1063/1.3054170 (cit. on pp. 63, 68).

[208] Tomohiro Nozaki, Yuji Sato, Takuya Ashida, Naoki Shimomura, and Masashi Sahashi. “In-plane angular-dependent exchange bias and blocking temperature of a Cr2O3 film system prepared by post annealing”. In: *Applied Physics Express* 7.9 (Sept. 2014), p. 093006. DOI: 10.7567/APEX.7.093006 (cit. on p. 63).

[209] Ch Binek, P. Borisov, Xi Chen, et al. “Perpendicular exchange bias and its control by magnetic, stress and electric fields”. In: *The European Physical Journal B* 45.2 (May 2005), pp. 197–201. DOI: 10.1140/epjb/e2005-00054-2 (cit. on p. 63).

[210] Tobias Kosub, Martin Kopte, Ruben Hühne, et al. “Purely antiferromagnetic magnetoelectric random access memory.” In: *Nature communications* 8.1 (Apr. 2017), p. 13985. DOI: 10.1038/ncomms13985 (cit. on p. 63).

[211] Natascha Hedrich, Kai Wagner, Oleksandr V. Pylypovskyi, et al. “Nanoscale mechanics of antiferromagnetic domain walls”. In: *Nature Physics* 17.5 (May 2021), pp. 574–577. DOI: 10.1038/s41567-020-01157-0 (cit. on p. 63).

[212] S.-H. Lim, M. Murakami, S.E. Lofland, et al. “Exchange bias in thin-film (Co/Pt)3/Cr2O3 multilayers”. In: *Journal of Magnetism and Magnetic Materials* 321.13 (July 2009), pp. 1955–1958. DOI: 10.1016/j.jmmm.2008.12.022 (cit. on p. 64).

[213] Igor Veremchuk, Maciej Oskar Liedke, Pavlo Makushko, et al. “Defect Nanostructure and its Impact on Magnetism of α -Cr 2 O 3 Thin Films”. In: *Small* 18.17 (Apr. 2022), p. 2201228. DOI: 10.1002/smll.202201228 (cit. on pp. 64, 75, 77).

[214] Po-Hung Lin, Bo-Yuan Yang, Ming-Han Tsai, et al. “Manipulating exchange bias by spin–orbit torque”. In: *Nature Materials* 18.4 (Apr. 2019), pp. 335–341. DOI: 10.1038/s41563-019-0289-4 (cit. on p. 65).

[215] Hyun-Joong Kim, Soong-Geun Je, Dae-Han Jung, Ki-Suk Lee, and Jung-Il Hong. “Field-free control of exchange bias by spin Hall currents”. In: *Applied Physics Letters* 115.2 (July 2019), p. 022401. DOI: 10.1063/1.5109967 (cit. on p. 65).

[216] Shouzhong Peng, Daoqian Zhu, Weixiang Li, et al. “Exchange bias switching in an antiferromagnet/ferromagnet bilayer driven by spin–orbit torque”. In: *Nature Electronics* 3.12 (Dec. 2020), pp. 757–764. DOI: 10.1038/s41928-020-00504-6 (cit. on p. 65).

[217] Jaimin Kang, Jeongchun Ryu, Jong-Guk Choi, et al. “Current-induced manipulation of exchange bias in IrMn/NiFe bilayer structures”. In: *Nature Communications* 12.1 (Dec. 2021), p. 6420. DOI: 10.1038/s41467-021-26678-x (cit. on p. 65).

[218] E. Z. Zhang, Y. C. Deng, X. H. Liu, et al. “Manipulating antiferromagnetic interfacial states by spin-orbit torques”. In: *Physical Review B* 104.13 (Oct. 2021), p. 134408. DOI: 10.1103/PhysRevB.104.134408 (cit. on p. 65).

[219] R. Lavrijsen, P. P. J. Haazen, E. Murè, et al. “Asymmetric Pt/Co/Pt-stack induced sign-control of current-induced magnetic domain-wall creep”. In: *Applied Physics Letters* 100.26 (June 2012), p. 262408. DOI: 10.1063/1.4732083 (cit. on p. 68).

[220] L. Herrera Diez, F. Ummelen, Vincent Jeudy, et al. “Magnetic domain wall curvature induced by wire edge pinning”. In: *Applied Physics Letters* 117.6 (Aug. 2020), p. 062406. DOI: 10.1063/5.0010798 (cit. on p. 69).

[221] P. Géhanne, S. Rohart, André Thiaville, and Vincent Jeudy. “Strength and length scale of the interaction between domain walls and pinning disorder in thin ferromagnetic films”. In: *Physical Review Research* 2.4 (Oct. 2020), p. 043134. DOI: 10.1103/PhysRevResearch.2.043134 (cit. on p. 69).

[222] Emilie Jué, André Thiaville, S. Pizzini, et al. “Domain wall dynamics in ultrathin Pt/Co/AlOx microstrips under large combined magnetic fields”. In: *Physical Review B* 93.1 (Jan. 2016), p. 014403. DOI: 10.1103/PhysRevB.93.014403 (cit. on p. 69).

[223] Emilie Jué, C. K. Safeer, Marc Drouard, et al. “Chiral damping of magnetic domain walls”. In: *Nature Materials* 15.3 (2016), pp. 272–277. DOI: 10.1038/nmat4518 (cit. on p. 69).

[224] Zhaochu Luo, Stefan Schären, Aleš Hrabec, et al. “Field- A nd Current-Driven Magnetic Domain-Wall Inverter and Diode”. In: *Physical Review Applied* 15.3 (2021), p. 1. DOI: 10.1103/PhysRevApplied.15.034077 (cit. on p. 71).

[225] D. A. Allwood, Gang Xiong, and R. P. Cowburn. “Domain wall diodes in ferromagnetic planar nanowires”. In: *Applied Physics Letters* 85.14 (Oct. 2004), pp. 2848–2850. DOI: 10.1063/1.1802388 (cit. on p. 71).

[226] M. T. Bryan, T. Schrefl, and D. A. Allwood. “Symmetric and asymmetric domain wall diodes in magnetic nanowires”. In: *Applied Physics Letters* 91.14 (Oct. 2007), p. 142502. DOI: 10.1063/1.2794030 (cit. on p. 71).

[227] Satoru Emori, Eduardo Martinez, Kyung-Jin Lee, et al. “Spin Hall torque magnetometry of Dzyaloshinskii domain walls”. In: *Physical Review B* 90.18 (Nov. 2014), p. 184427. DOI: 10.1103/PhysRevB.90.184427 (cit. on pp. 72, 73).

[228] J. H. Franken, M. Herps, H. J. M. Swagten, and B. Koopmans. “Tunable chiral spin texture in magnetic domain-walls”. In: *Scientific Reports* 4.1 (May 2015), p. 5248. DOI: 10.1038/srep05248 (cit. on p. 72).

[229] Sai Mu and K. D. Belashchenko. “Influence of strain and chemical substitution on the magnetic anisotropy of antiferromagnetic Cr2O3, an ab-initio study”. In: *Physical Review Materials* 3.3 (Mar. 2019), p. 034405. DOI: 10.1103/PhysRevMaterials.3.034405 (cit. on p. 73).

[230] Jacob Torrejon, Victor Raposo, Eduardo Martinez, Rafael P. del Real, and Masamitsu Hayashi. “Current-induced dynamics of chiral domain walls in magnetic heterostructures”. In: *Magnetic Nano- and Microwires*. 2nd ed. Dm. Elsevier, 2020, pp. 297–324. DOI: 10.1016/B978-0-08-102832-2.00010-4 (cit. on p. 73).

[231] Erol Girt, W. Huttema, O. N. Mryasov, et al. “A method for measuring exchange stiffness in ferromagnetic films”. In: *Journal of Applied Physics* 109.7 (Apr. 2011), 07B765. DOI: 10.1063/1.3565203 (cit. on p. 73).

[232] Tsung-Han Yang, S. Mal, C. Jin, R. J. Narayan, and J. Narayan. “Epitaxial VO2/Cr2O3/sapphire heterostructure for multifunctional applications”. In: *Applied Physics Letters* 98.2 (Jan. 2011), p. 022105. DOI: 10.1063/1.3541649 (cit. on pp. 75, 76).

[233] Howard F. McMurdie, Marlene C. Morris, Eloise H. Evans, et al. “Standard X-Ray Diffraction Powder Patterns from the JCPDS Research Associateship”. In: *Powder Diffraction* 1.2 (June 1986), pp. 64–77. DOI: 10.1017/S0885715600011593 (cit. on p. 75).

[234] N. M. Vu, X. Luo, S. Novakov, et al. “Bulk-like dielectric and magnetic properties of sub 100 nm thick single crystal Cr2O3 films on an epitaxial oxide electrode”. In: *Scientific Reports* 10.1 (Dec. 2020), p. 14721. DOI: 10.1038/s41598-020-71619-1 (cit. on p. 76).

[235] Yohei Kota, Hiroshi Imamura, and Munetaka Sasaki. “Strain-Induced Néel Temperature Enhancement in Corundum-Type Cr 2 O 3 and Fe 2 O 3”. In: *Applied Physics Express* 6.11 (Nov. 2013), p. 113007. DOI: 10.7567/APEX.6.113007 (cit. on p. 77).

[236] M. Binder, A. Weber, O. Mosendz, et al. “Magnetization dynamics of the ferrimagnet CoGd near the compensation of magnetization and angular momentum”. In: *Physical Review B* 74.13 (Oct. 2006), p. 134404. DOI: 10.1103/PhysRevB.74.134404 (cit. on pp. 81, 85, 87, 90, 91).

[237] Yue Zhang, Xueqiang Feng, Zhenyi Zheng, et al. “Ferrimagnets for spintronic devices: From materials to applications”. In: *Applied Physics Reviews* 10.1 (Mar. 2023), p. 011301. DOI: 10.1063/5.0104618 (cit. on p. 82).

[238] Joseph Barker and Unai Atxitia. “A Review of Modelling in Ferrimagnetic Spintronics”. In: *Journal of the Physical Society of Japan* 90.8 (Aug. 2021), p. 081001. DOI: 10.7566/JPSJ.90.081001 (cit. on p. 82).

[239] Takaya Okuno, Duck-Ho Kim, Se-Hyeok Oh, et al. “Spin-transfer torques for domain wall motion in antiferromagnetically coupled ferrimagnets”. In: *Nature Electronics* 2.9 (Sept. 2019), pp. 389–393. DOI: 10.1038/s41928-019-0303-5 (cit. on p. 83).

[240] Takaya Okuno. “Spin-Transfer Torques for Domain Wall Motion in Antiferromagnetically-Coupled Ferrimagnets”. In: *Springer, Singapor*. 2020, pp. 25–48. DOI: 10.1007/978-981-15-9176-1{_}2 (cit. on p. 83).

[241] Dong-Hyun Kim, Duck-Ho Kim, Kab-Jin Kim, et al. “The dynamics of a domain wall in ferrimagnets driven by spin-transfer torque”. In: *Journal of Magnetism and Magnetic Materials* 514.June (Nov. 2020), p. 167237. DOI: 10.1016/j.jmmm.2020.167237 (cit. on p. 83).

[242] Do Bang, Pham Van Thach, and Hiroyuki Awano. “Current-induced domain wall motion in antiferromagnetically coupled structures: Fundamentals and applications”. In: *Journal of Science: Advanced Materials and Devices* 3.4 (Dec. 2018), pp. 389–398. DOI: 10.1016/j.jsamd.2018.09.003 (cit. on p. 83).

[243] Do Bang and Hiroyuki Awano. “Current-Induced Domain Wall Motion in Perpendicular Magnetized Tb–Fe–Co Wire with Different Interface Structures”. In: *Applied Physics Express* 5.12 (Nov. 2012), p. 125201. DOI: 10.1143/APEX.5.125201 (cit. on p. 83).

[244] V. V. Yurlov, K. A. Zvezdin, P. N. Skirdkov, and A. K. Zvezdin. “Domain wall dynamics of ferrimagnets influenced by spin current near the angular momentum compensation temperature”. In: *Physical Review B* 103.13 (Apr. 2021), p. 134442. DOI: 10.1103/PhysRevB.103.134442 (cit. on p. 83).

[245] E. Haltz, J. Sampaio, S. Krishnia, et al. “Measurement of the tilt of a moving domain wall shows precession-free dynamics in compensated ferrimagnets”. In: *Scientific Reports* 10.1 (Dec. 2020). DOI: 10.1038/s41598-020-73049-5 (cit. on pp. 83, 87, 90).

[246] Haltz Eloi. “Domain Wall Dynamics driven by spin-current in Ferrimagnetic alloys ELOI HALTZ Composition du Jury”. PhD thesis. Université Paris-Saclay, 2019 (cit. on pp. 83, 90).

[247] Yuqing Zhou, Teng Xu, Xue Liang, et al. “A comparative study of the domain wall motion in ferrimagnets (Fe,Co) 1 x (Gd,Tb) x”. In: *Nanoscale* 14.37 (2022), pp. 13526–13531. DOI: 10.1039/D2NR02594A (cit. on p. 83).

[248] Young-gwan Choi, Daegeun Jo, Kyung-hun Ko, et al. “Observation of the orbital Hall effect in a light metal Ti”. In: *arXiv:2109.14847v1* (Sept. 2021), pp. 1–17 (cit. on p. 83).

[249] Shilei Ding, Andrew Ross, Dongwook Go, et al. “Harnessing Orbital-to-Spin Conversion of Interfacial Orbital Currents for Efficient Spin-Orbit Torques”. In: *Physical Review Letters* 125.17 (Oct. 2020), p. 177201. DOI: 10.1103/PhysRevLett.125.177201 (cit. on pp. 83, 98).

[250] Lucas Caretta, Maxwell Mann, Felix Büttner, et al. “Fast current-driven domain walls and small skyrmions in a compensated ferrimagnet”. In: *Nature Nanotechnology* 13.12 (Dec. 2018), pp. 1154–1160. DOI: 10.1038/s41565-018-0255-3 (cit. on pp. 83, 87–90, 94).

[251] Chen-Yu Hu, Yu-Fang Chiu, Chia-Chin Tsai, et al. “Toward 100% Spin–Orbit Torque Efficiency with High Spin–Orbital Hall Conductivity Pt–Cr Alloys”. In: *ACS Applied Electronic Materials* 4.3 (Mar. 2022), pp. 1099–1108. DOI: 10.1021/acsaelm.1c01233 (cit. on p. 83).

[252] Shigeo Honda and Masatoshi Yoshiyama. “Magneto-Optical Kerr Rotation and Sublattice Magnetic Moments in RE-Co Sputtered Films”. In: *Japanese Journal of Applied Physics* 27.9R (Sept. 1988), p. 1687. DOI: 10.1143/JJAP.27.1687 (cit. on p. 85).

[253] Rahul Mishra, Jiawei Yu, Xuepeng Qiu, et al. “Anomalous Current-Induced Spin Torques in Ferrimagnets near Compensation”. In: *Physical Review Letters* 118.16 (2017), pp. 1–6. DOI: 10.1103/PhysRevLett.118.167201 (cit. on p. 86).

[254] Duck Ho Kim, Mitsutaka Haruta, Hye Won Ko, et al. “Bulk Dzyaloshinskii–Moriya interaction in amorphous ferrimagnetic alloys”. In: *Nature Materials* 18.7 (July 2019), pp. 685–690. DOI: 10.1038/s41563-019-0380-x (cit. on p. 87).

[255] N. Bergeard, A. Mougin, M. Izquierdo, E. Fonda, and F. Sirotti. “Correlation between structure, electronic properties, and magnetism in Co x Gd 1-x thin amorphous films”. In: *Physical Review B* 96.6 (Aug. 2017), p. 064418. DOI: 10.1103/PhysRevB.96.064418 (cit. on p. 87).

[256] P. Hansen, C. Clausen, G. Much, M. Rosenkranz, and K. Witter. “Magnetic and magneto-optical properties of rare-earth transition-metal alloys containing Gd, Tb, Fe, Co”. In: *Journal of Applied Physics* 66.2 (July 1989), pp. 756–767. DOI: 10.1063/1.343551 (cit. on p. 87).

[257] Eloi Haltz, Sachin Krishnia, Léo Berges, Alexandra Mougin, and João Sampaio. “Domain wall dynamics in antiferromagnetically coupled double-lattice systems”. In: *Physical Review B* 103.1 (Jan. 2021), p. 014444. DOI: 10.1103/PhysRevB.103.014444 (cit. on p. 87).

[258] Léo Berges, Eloi Haltz, Sujit Panigrahy, et al. “Size-dependent mobility of skyrmions beyond pinning in ferrimagnetic GdCo thin films”. In: *Physical Review B* 106.14 (Oct. 2022), p. 144408. DOI: 10.1103/PhysRevB.106.144408 (cit. on p. 88).

[259] Saima A. Siddiqui, Jiahao Han, Joseph T. Finley, Caroline A. Ross, and Luqiao Liu. “Current-Induced Domain Wall Motion in a Compensated Ferrimagnet”. In: *Physical Review Letters* 121.5 (July 2018), p. 057701. DOI: 10.1103/PhysRevLett.121.057701 (cit. on pp. 88, 90, 93).

[260] Yuushou Hirata, Duck Ho Kim, Takaya Okuno, et al. “Effect of depinning field on determination of angular-momentum-compensation temperature of ferrimagnets”. In: *Applied Physics Express* 11.6 (June 2018). DOI: 10.7567/APEX.11.063001 (cit. on pp. 92–94).

[261] Z. C. Zheng, Q. X. Guo, D. Jo, et al. “Magnetization switching driven by current-induced torque from weakly spin-orbit coupled Zr”. In: *Physical Review Research* 2.1 (Feb. 2020), p. 013127. DOI: 10.1103/PhysRevResearch.2.013127 (cit. on p. 98).

[262] Amit Rothschild, Nadav Am-Shalom, Nirel Bernstein, et al. “Generation of spin currents by the orbital Hall effect in Cu and Al and their measurement by a Ferris-wheel ferromagnetic resonance technique at the wafer level”. In: *Physical Review B* 106.14 (Oct. 2022), p. 144415. DOI: 10.1103/PhysRevB.106.144415 (cit. on p. 98).

[263] Gunasheel Kauwtilyaa Krishnaswamy, Giacomo Sala, Benjamin Julien Jacot, et al. “Time-Dependent Multistate Switching of Topological Antiferromagnetic Order in Mn3Sn”. In: *Physical Review Applied* 18.2 (Aug. 2022), p. 024064. DOI: 10.1103/PhysRevApplied.18.024064 (cit. on p. 131).

Journal articles

1. **Jacot, B. J.**, Vèlez, S., Noël, P., Helbingk, P., Lambert, C.-H., Gambardella, P. (2022). Control of field- and current-driven magnetic domain wall motion by exchange bias in Cr_2O_3/Co/Pt trilayers. Physical Review B, 106(13), 134411. [165]

2. Vélez, S., Ruiz-Gómez, S., Schaab, J., Gradauskaite, E., Wörnle, M. S., Welter, P., **Jacot, B. J.**, Degen, C. L., Trassin, M., Fiebig, M., Gambardella, P. (2022). Current-driven dynamics and ratchet effect of skyrmion bubbles in a ferrimagnetic insulator. Nature Nanotechnology, 17(8), 834–841. [34]

3. Krishnaswamy, G. K., Sala, G., **Jacot, B. J.**, Lambert, C.-H., Schlitz, R., Rossell, M. D., Noël, P., Gambardella, P. (2022). Time-Dependent Multistate Switching of Topological Antiferromagnetic Order in Mn_3Sn. Physical Review Applied, 18(2), 024064. [263]

4. **Jacot, B. J.**, Krishnaswamy, G., Sala, G., Avci, C. O., Vélez, S., Gambardella, P., Lambert, C.-H. (2020). Systematic study of nonmagnetic resistance changes due to electrical pulsing in single metal layers and metal/antiferromagnet bilayers. Journal of Applied Physics, 128(17), 173902. [122]

Manuscript in preparation

1. **Jacot, B. J.**, Kang M., Gambardella, P. “Increase of current-induced magnetic domain wall velocity by orbital Hall effect in Pt/CoGd/Cr trilayers”.

Conferences

1. Contributed talk: "Control of domain wall motion with exchange bias", Néel Colloquium 2022, Award of the best poster presentation.

BENJAMIN JULIEN JACOT

CONTACT

Address:
Rue de la Poste 14
2024 St-Aubin, Neuchâtel

Phone:
+41 (0)79 617 42 57

Email:
benjaminjacot@hotmail.com

LinkedIn:
linkedin.com/benjaminjacot

LANGUAGES

French

English

German

SKILL HIGHLIGHTS

- Physical modelling
- Experimental physics
- Team work
- Academic writing
- Teaching

EDUCATION

Master's degree in Physics | ETH Zurich
2018 | Zürich, Switzerland

- Master Thesis: Computational Physics at University of Cambridge (UK). Grade: 5.5/6
- Semester work: THz spectroscopy at ETHZ
- Specialization: quantum computing and quantum optics

Bachelor's degres in Physics | EFP Lausanne
2016 | Lausanne, Switzerland

- Specialization: computational physics, biophysics and plasma physics

WORK EXPERIENCE

PhD Researcher | ETH Zurich
02/2019 – 04/2023 | Zürich, Switzerland

- Experimental research on the electrical manipulation of magnetic materials for logic and memory devices.
- Device fabrication and characterization
    - Sputtering, photolithography, clean room
    - Magnetotransport measurements
    - Microscopy of magnetic domain wall motion
- Instrumentation
    - Development of Graphic User Interface (GUI) with Matlab for automatized measurement processes
    - RF electronics for fast electrical switching
- Micromagnetic simulation
- Publication in scientific peer-reviewed journals

Teaching Assistant | ETH Zurich
09/2019 – 2022 | Zurich, Switzerland

- Teaching physics for Material scientists at D-MATL

SOFTWARES

- Matlab for Physical Modelling, GUI
- Python for Machine Learning
- C++ for Object Orientated Programing
- Origin Pro for data visualization

HOBBIES

- Outdoor sports: cycling and ski touring
- Sailing racing on Neuchâtel's lake
- Gardening of old-fashioned veggies

REFERENCES

Dr. Paul Noël
Post-doc | ETH Zurich
E-Mail:
paul.noel@mat.ethz.ch

Prof. Pietro Gambardella
Professor | ETH Zurich
E-Mail:
pietro.gambardella@mat.ethz.ch /
Tel: +41 (0) 44 633 07 56

Internship I Swiss Center of Electronics and Microtechnologies CSEM

05/2018 – 11/2018 I Neuchatel, Switzerland

- Implementation of world 1st active atomic clockwork laser wits saturable vapor cell absorber, supervised by Dr. Dmitri Boiko and Dr. Steve Lecomte

Sabbatical leave – 11/2018 – 02/2019

- Trip with campervan in Australia, hiking in New Zealand and train travel in Japan.
- Budget management of limited monetary resources, my student savings :-)

Part-time job I Fraises et Outils Sélection SA
2009 – 2017 I Bevaix, Switzerland

- Manufacture of high precision tools for key machine cutters
- Packaging and shipment of products

PUBLICATIONS

Google Scholar profile

Jacot, B. J., Kang M., Gambardella, P. "Increase of current-induced magnetic domain wall velocity by orbital hall effect in Pt/CoGd/Cr trilayers". In preparation

Jacot, B. J., Vélez, S., Noël, P., Helbingk, P., Lambert, C.-H., Gambardella, P. (2022). "Control of field- and current-driven magnetic domain wall motion by exchange bias in Cr_2O_3/Co/Pt trilayers". Physical Review B **106**, 134411

Vélez, S., Ruiz-Gómez, S., Schaab, J., Gradauskaite, E., Wörnle, M. S., Welter, P., **Jacot, B. J.**, Degen, C. L., Trassin, M., Fiebig, M., Gambardella, P. (2022). "Current-driven dynamics and ratchet effect of skyrmion bubbles in a ferrimagnetic insulator". Nature Nanotechnology, 17(8), 834–841.

Krishnaswamy, G. K., Sala, G., **Jacot, B. J.**, Lambert, C.-H., Schlitz, R., Rossell, M. D., Noël, P., Gambardella, P. (2022). Time-Dependent Multistate Switching of Topological Antiferromagnetic Order in Mn3Sn. Physical Review Applied, 18(2), 024064.

Jacot, B. J., Krishnaswamy, G., Sala, G., Avci, C. O., Vélez, S., Gambardella, P., Lambert, C.-H. (2020). "Systematic study of nonmagnetic resistance changes due to electrical pulsing in single metal layers and metal/antiferromagnet bilayers". Journal of Applied Physics, 128(17), 173902.

Awards

Award best poster presentation, Néel Colloquium 2022